MODELING THE INTERFACE BETWEEN BIOLOGICAL AND SYNTHETIC COMPONENTS IN HYBRID NANOSYSTEMS

BY

ROGAN C. CARR

DISSERTATION

Submitted in partial fulfillment of the requirements
for the degree of Doctor of Philosophy in Physics
in the Graduate College of the
University of Illinois at Urbana-Champaign, 2011

Urbana, Illinois

Doctoral Committee:

Professor Robert M. Clegg, Chair
Assistant Professor Aleksei Aksimentiev, Director of Research
Professor John D. Stack
Assistant Professor Luke Olson

Abstract

The fusion of biology and nanotechnology holds amazing promise for revolutionizing medicine and personal technology. In order to take advantage of the great feats of engineering coming out of these fields, there needs to be theories and computational tools capable of describing the interface between the pristine and ordered world of precision electronics and the hot, wet, and stochastic world of biology. The success of these technologies will depend on our abilities to design and optimize interactions of biomolecules and solid-state materials down to the atomic scale. In my research at the University of Illinois, I have used molecular dynamics (MD) as a tool to describe the atomic-scale interactions driving the function of biomolecules and their interface with solid-state devices, and I have sought to use it as a starting point to create new methods for modeling, designing, and optimizing these interactions. In my dissertation, I show the methodologies that I use in my work and the range of possibilities that they present for researchers in the field, and I present my research on the modeling of the interface between biological and synthetic materials in (1) immunosurfaces used for detection of live bacteria; (2) protein transport through a nanochannel; (3) deriving the Langmuir constant for adsorption for small, organic molecules on synthetic surfaces; (4) creating a multiscale model for transport in micro- and nanofluidic devices; (5) synthetic analogs of biological ion channels. It is my hope that the research that I have performed in my doctoral studies here at the University of Illinois at Urbana-Champaign will be a template for future research and interdisciplinary science. The work I have done here has shown the possibilities of the MD method for studying the physical interface of biological and synthetic components, and I have developed new techniques that can be used by researchers in field to further the science and engineering of bionanotechnology and nanobiotechnology.

Where are we going, Walt Whitman? The doors close in an hour. Which way does your beard point tonight?

— *Allen Ginsberg,* A Supermarket in California

Acknowledgments

I would like to thank the members of my committee, past and present: Professors Robert M. Clegg, Aleksei Aksimentiev, John D. Stack, Luke Olson, Greg Timp, and Karin Dahmen. I am especially grateful to my advisor, Aleksei Aksimentiev. I have learned a lot under his tutelage, not the least of which are how to perform scientific research and set long-term goals for a lab, and he has overseen my development as a physicist is these past four and a half years that I have worked for him. I would like to acknowledge all of his help here at the University of Illinois, and I believe that my success as a scientist is due in large part to the knowledge and abilities I have gained under his tutelage.

I would like to thank all the members of the Aksimentiev group: Jeff Comer, Chris Maffeo, David Wells, Swati Bhattacharya, Max Belkin, Binquan Luan and Jejoong Yoo. They have been a great resource, not only for science, but friendship and support. I think that our camaraderie and combined knowledge, personalities, senses of humor, and just general state of awesomness made us the best research group in the department. I am going to have fond memories our time together in Loomis for the rest of my life, including our development of the highly parallel cluster of maple trees.

I am indebted to all the individuals who have helped me out along the way: All my collaborators, those members of the physics department who took me under their wing, and the scientists outside of the university who have given me great advice and sent me in interesting directions. The department of physics at the University of Illinois at Urbana-Champaign has been a wonderful place to pursue a Ph.D. The impressive collection of minds, the great introductory classes and being surrounded by a great class of graduate students have made my time here special. The setting in Urbana, of course, is also ideal, with its great people, shops, green tree-lined streets, and farmer's market.

Finally, I would like to thank my family and my friends for all their support. My parents, Edward and Elizabeth, have always supported me and pushed me to be my best. My brother, Aengus, who has always been there for me. My wife, Christy, who has been with me day in and day out through this process and always inspires me to be my best. And a thanks to all my friends in Champaign-Urbana, especially to Brandon, Kevin and Garrett Bowersox-Johnson, who invited me into their family all those years ago.

This work was supported by grants from the National Institutes of Health (R01-HG003713 and PHS 5 P41-RR05969), National Science Foundation (PHY-0822613 and DMR-0955959), the Petroleum Research Fund (48352-G6) and through a cooperative research agreement with the U.S. Army Engineer Research and Development Center - Construction Engineering Research Laboratory (ERDC-CERL). The author gladly acknowledge supercomputer time provided by the TeraGrid through grant MCA05S028 and through the Department of Defense High Performance Computing Modernization Program at the ERDC Supercomputing Resource Center, Vicksburg, Mississippi.

Table of Contents

List of Abbreviations . . . . . **viii**

Chapter 1 Introduction **1**

Chapter 2 Immunosurfaces for Bacterial Detection **9**

Chapter 3 Modeling Protein Transport through Nanochannels **16**

Chapter 4 Microscopic perspective on the adsorption isotherm of a heterogeneous surface **28**

Chapter 5 Atoms-to-microns model for small solutes transport through sticky nanochannels **35**

Chapter 6 Synthetic ion channels embedded in biological membranes **48**

Appendix A Immunosurfaces for Bacterial Detection **56**
A.1 Molecular dynamics methods 56
A.2 Details of the atomic-scale model 57
A.3 Modeling the degradation of functionalized silica 58
A.4 Potential of mean force calculations 58

Appendix B Modeling Protein Transport through Nanochannels **60**
B.1 All-atom molecular dynamics 60

Appendix C Microscopic perspective on the adsorption isotherm of a heterogeneous surface **61**
C.1 Molecular dynamics simulations. 61
C.2 All-atom model for dimethyl methylphosphonate (DMMP). 61
C.3 All-atom model for synthetic surfaces. 64
C.4 Solute adsorption simulations and analysis. 65
C.5 Calculations of the maximum adsorption density. 67
C.6 Umbrella sampling simulations. 68
C.7 Potential of mean force calculation. 69
C.8 Surface Characterization. 70

Appendix D Atoms-to-microns model for small solutes transport through sticky nanochannels **73**
D.1 All-atom model for synthetic surfaces. 73
D.2 MD simulation setup 75
D.3 Analysis of the BD and MD simulations 76
D.4 Umbrella sampling simulations. 76
D.5 Potential of mean force calculation. 77
D.6 Implicit Solvent MD Simulations 78
D.7 Smoluchowski model 79

Appendix E Synthetic ion channels embedded in biological membranes 81
E.1 Coarse-grained molecular dynamics 81
E.2 Modeling the system with a coarse grain 81
E.3 Validation of the coarse-grain model 82

Appendix F Publications 84

References 85

List of Abbreviations

BD	Brownian Dynamics
CG	Coarse Grain
CGMD	Coarse Grain Molecular Dynamics
DMMP	Dimethyl Methylphosphonate
DODA	Dimethyldioctadecylammonium
GAPSG	Corning GAPS II amine-terminated Glass
MD	Molecular Dynamics
NAMD	Nanoscale Molecular Dynamics
PMF	Potential of Mean Force
POM	Polyoxometalate or specifically Polyoxomolybdate
POPC	Palmitoyloleoylphosphatidylcholine
SMD	Steered Molecular Dynamics
UNCD	Ultra Nanocrystalline Diamond
WHAM	Weighted Histogram Analysis Method

Chapter 1

Introduction

Hybrid structures that combine biological and inorganic materials are ubiquitous in the biosphere, from the carbonated hydroxyapatite that makes up the inorganic structure of bones, to the calcium carbonate created by coral polyps and coralline algae that forms the structure of coral reefs. The ability to design materials that are biocompatible, or able to be incorporated into organisms without provoking an immune response, has significant applications in medicine and therapeutics, for example in designing prosthetics and implanted medical devices like pacemakers. However, designing synthetic materials to interact favorably with biological components is made difficult by the fact that many biological processes, including immune response, are dictated by interactions between biomolecules and their environment on the nanometer scale. Therefore, our ability to fabricate materials with nanometer precision will determine our ability to create devices that can interface with the biological world.

The technology driving the miniaturization of materials manufacturing has advanced to the point where it is now possible to manufacture synthetic device structures on the nanometer scale. Researchers can create surfaces patterned with 25 nm diamond grains [1, 2], nanopores smaller than the width of duplex DNA [3], macroscopic-length channels with cross-sections smaller than ten nanometers [4], and hollow metal-oxide macromolecular spheres measuring 4 nm across [5]. Although manufacturing structures with feature sizes of several nanometers is now possible, how these structures will interact with biomolecules is difficult to predict. The warm and wet environments necessary for biology and the function of biomolecules are incompatible with the imaging methods usually applied to the nanoscale, such as electron microscopy. Computational models provide a way to visualize and quantify the nanoscale details of interaction between biomolecules and synthetic materials. With accurate computational models, it will be possible to optimize next-generation devices that incorporate biological and synthetic nanostructured components and manufacture them on a commercial scale.

With the goal of interfacing biology and technology in mind, a whole new genre of science has emerged. One section of this hybrid science, a blend of physics, chemistry, biology, materials science and engineering, seeks to take advantage of the nanoscale revolution by building new sensing tools to learn more about

biology [6, 7, 8] — the field of nanobiotechnology — creating new devices ranging from synthetic surfaces patterned with biomolecules, to nanopores in semiconductor material capable of detecting single molecules, to whole biochemistry wet labs shrunk down to fit on a single chip. Another side seeks to take advantage of biology's atomic-scale precision tools and make new devices by incorporating biomolecules into synthetic devices [9] — the field of bionanotechnology. Whatever you call these fields, they promise to provide us with new, exciting technologies by elucidating and developing control over the nanoscale world. In order to take advantage of the great feats of engineering coming out of these fields, there needs to be theories and computational tools capable of describing the interface between the pristine and ordered world of precision electronics and the hot, wet, and stochastic world of biology. The success of these technologies will depend on our abilities to design and optimize interactions of biomolecules and solid-state materials down to the atomic scale.

One of the strengths of electronics manufacturing is the great control engineers have over surface patternization. Creating patterned surfaces is a standard process in the electronics industry, where commercial methods for lithography used in microchip fabrication have been extended down to 22 nm [10]. While that scale is too large to create regular single-molecule-sized device features, the bio-nano world has been pushing the limits with hybrid technologies. In a method known as DNA origami, double-stranded DNA can be folded into 3D structures and layered on surfaces to create 6-nm resolution patterned surfaces with a chosen DNA sequence [11]. These "nanobreadboards" [11] can provide accurate templates for defining regular small distances between binding sites for small molecules to make precise measurements [12]. Solid surfaces like glass or polymer can be pattered with single-stranded DNA open to solution allowing complementary DNA to hybridize to create a device known as a DNA microarray [13, 14]. These structures are the basis of many high-throughput biological assays such as ChIP-on-chip [15], which combines DNA microarrays ("chips") with chromatin immunoprecipitation (ChIP) to investigate protein–DNA interactions. With biological and solid-state methods combined, it is likely we will see the ability to pattern surfaces on the single-nanometer level soon, opening up the development of a whole new set of technologies.

In a move analogous to the reduction in size of the fundamental components of electronics, researchers are pushing to shrink the components of wet labs down to the micro- and nanoscale, so that a laboratory for producing chemical or biological products, filtering solutions, or performing measurements with high sensitivity could fit on a microchip. This would not only save lab space and money spent on chemical reagents, but it would also allow for parallel, high-throughput assays and the ability to perform new types of detection not possible on the macro scale. The advance of micro- and nanofluidic technologies has already enabled the creation of new devices for applications like high throughput biological assays [6, 7, 8],

protein crystallography [16] and the direct, quantitative study of interfacial phenomena like adsorption [17]. However, as the device components become smaller, for example in fluid channels of a sub-10-nanometer cross-section [4], the effects of interactions of the solutes with the device surface are magnified and can lead to degradation of the device [18]. Having methods to model the device–solution interface will not only allow for designs to prevent device breakdown, but allow designers to take advantage of these properties and open up a whole new range of applications.

The ability to create such small features in semiconductor materials has led to the development of synthetic nanopore technologies [19]. Synthetic nanopores are small holes, with diameters measured in nanometers, created in solid-state [20] or polymers [21] that can mimic protein nanopores in both size and sensitivity. These devices can take advantage of the small constriction to limit passage to one molecule at a time, and perform fine measurements on the passenger molecules, such as discriminating between bases in a DNA molecule for high-throughput DNA sequencing [22]. Control over the charge and chemistry of the pore can allow for current rectification similar to a ion channel protein [23]. These technologies have made such an impact that IBM has bought in and is developing nanopore technology called a "DNA transistor" [24]. To create successful devices, the high sensitivity to detect single molecules needs to aided by models that can decipher differences in electronic signals originating from the nanoscale properties of the passenger molecules [25].

Nanoscale engineering has progressed to the point where it is possible to design devices to mimic the behavior of biological machinery like proteins. However, biological molecules can already be constructed with atomic-scale accuracy and operate with atomic-scale precision. By designing new devices made from a combination of synthetic materials and biological components, researchers can get the best of both worlds: the durability, fine control over electromagnetic properties, and large-scale manufacturing base that synthetic components offer and the high specificity, atomic-scale accuracy in production, and access to all of evolution's inventions offered by biomolecules. To take advantage of the high specificity of biomolecules, researchers have created a new type of chip, called an immunosurface, to detect distinct molecules by layering antibody proteins on synthetic surfaces [2, 26]. The atomic-scale accuracy in protein production has led some researchers to use protein nanopores for single-molecule detection, as the pore interiors can be systematically designed on the level of groups of atoms [27]. These protein pores can then be embedded in synthetic lipid bilayers [27] or solid state membranes [28]. The combination of biological and synthetic components into new devices opens many possibilities, of which these applications are just two. It will be fascinating to watch the development of this art over the coming years. However, hybrid devices remain difficult to design because the interactions of the biomolecules and synthetic surfaces are often very strong,

leading to the adsorption of biomolecules and the breakdown of the device [2, 29].

The wedding of biology and nanotechnology holds amazing promise for new and revolutionary technologies. While the goals of the individual research programs may be completely different, covering anything from shrinking the cost of drug manufacturing, to creating *in-situ* bacteria detectors, to efficiently sequencing DNA, to creating new types of synthetic biocompatible materials, the problems the researchers face are similar. First and foremost, it is often not possible to image the devices on the scale of their functional components. The environment necessary for biology and the function of biomolecules is incompatible with the imaging methods, such as electron microscopy, usually applied to the nanoscale. Furthermore, many of the devices being made are "one-shot" devices; the atomic-scale properties vary from device to device, leading to differences in behavior. In order to overcome these setbacks and create devices that can be manufactured in bulk, theoretical tools need to be created that will enable the optimization and design of these types of devices.

While the physics surrounding the construction and operations of these devices is well understood [30, 31, 32], there is no one theoretical model that will be able to describe all parts of the device efficiently. The different time- and length-scales and physical phenomena inherent in a single device call for specialized techniques to model different parts of these devices [33]. For example, continuum models work well for modeling the pressure-driven or electroosmotic fluid flow through micro- and nanofluidic devices [31, 32, 34], but these models break down in the regions of fluid near surfaces [32] or macromolecules [35], where the atomic-scale characteristics of the solvent, solutes, and surfaces, which can be on the order of nanometers [29, 36], become important. When the interactions within these regions becomes significantly affect device function or behavior, such as the adsorption of solutes [37] that could lead to clogging of the device [18], the use of discrete methods like classical molecular dynamics (MD) becomes necessary. In my published work [38, 39, 29, 37, 40, 41, 42], I have used MD as a tool to describe the atomic-scale interactions driving the function of biomolecules and their interface with solid-state devices and sought to use it as a starting point to create new methods for modeling, designing, and optimizing these interactions.

Classical molecular dynamics, often referred to as simply molecular dynamics or MD, is a computational technique used to simulate systems of point-mass particles in situations where all the forces are known but there are too many coupled degrees of freedom to write down an analytical solution. Starting with an initial set of coordinates for all the particles of the system, time is advanced using Newton's equation,

$$\vec{F} = m\vec{a}, \tag{1.1}$$

where the force $\vec{F}$ is the derivative of some potential function, U. The choice of the potential function U is determined by the type of simulation being performed. For simulations of biomolecules, the potential function U will typically have the form

$$U_{\text{total}} = \sum_{\text{bonds } i} k_i^{\text{bond}} \left(r_i - r_{0i}\right)^2 + \sum_{\text{angle } i} k_i^{\text{angle}} \left(\theta_i - \theta_{0i}\right)^2 \tag{1.2}$$

$$+ \sum_{\text{dihedrals } i} k_i^{\text{dihed}} \begin{cases} \left[1 + \cos\left(n_i\phi_i - \gamma_i\right)\right] & n_i \neq 0 \\ \left(\phi_i - \gamma_i\right)^2 & n_i = 0 \end{cases}$$

$$+ \sum_i \sum_{j>i} 4\epsilon_{ij} \left[\left(\frac{\sigma_{ij}}{r_{ij}}\right)^{12} - \left(\frac{\sigma_{ij}}{r_{ij}}\right)^{6}\right] + \sum_i \sum_{j>i} \frac{q_i q_j}{4\pi\epsilon r_{ij}}, \tag{1.3}$$

where the first term is a two-body interaction representing chemical bonds, the second term a three-body term representing the angle between bonds, the third term a four-body term representing the twist between a pair of bonded atoms, the fourth term a two-body interaction representing van der Waals forces and the fifth term a two-body interaction representing the explicit Coulomb interaction. The set of constants is known as the "force field" and is determined through *ab initio* quantum mechanics calculations and experiment [43]. On top of the potential function U, MD simulations can be performed with additional stochastic forces used to regulate the temperature and pressure of the systems. Typical MD simulations containing biomolecules or biomolecules and solid-state components usually contain anywhere from 50 k to 5 M atoms and are therefore solved with optimized parallel programs, like NAMD [43], on a supercomputer.

While MD is a brute force technique, it offers the advantage that it can explicitly calculate inter-particle interactions with all-atom precision, and it has been used extensively to simulate biological molecules [43, 44, 45, 46, 47]. Recent advancements in biomolecular-compatible inorganic forcefields [48, 49, 50, 51, 52, 53] have made it possible to computationally model the interactions of biomolecules with inorganic substrates with all-atom detail [48, 54, 51, 55, 56, 53]. Indeed, the use of MD in simulations of hybrid biological and synthetic systems is a growing field [41], and can provide much needed insight into the interfacial region between the worlds of biology and technology.

In my work, I have pushed the use of MD as a tool to study the physical interface between solid-state devices and biological molecules and sought to show that MD should be considered an invaluable tool for device design and optimization in bionanotechnology and nanobiotechnology. I think of MD as a brute force tool, but one that can also be used for precision. When I approach a new system, I can use straight MD simulations to observe the dynamics and characteristics of the system. These simulations, while simple, can produce enormous amounts of data from which I can extract statistics and gain quantitative knowledge of

the system. From here, I can perform additional simulations directed at specific characteristics of the system. For example, I can run many simulations with varied parameters, calculating the change in system behavior as a function of these variables, much like a computational experiment, or I can use MD with external forces added in to calculate specific quantities like the potential of mean force (PMF, the free energy along a set of coordinates). In this way, I can use MD as a springboard to create higher level theories. In my dissertation, I present my published work that details my methodologies and the new techniques that I have developed, showing by example how MD can be used as a successful tool to quantitatively characterize the interface of biology and technology.

In Chapter 2, I present research done in collaboration with the research groups of Bashir, Hamers, Carlisle and King in which I employ MD as an analytical tool to diagnose the nanoscale behavior of a prototype immunosurface for detecting bacterial pathogens. Pathogens in food and water supplies can cause serious illness and death. Outbreaks of food and water-borne bacteria are often caused by contamination of the food or water supply by outside sources, and as such, should be preventable given real-time detection tools. Immunosurfaces are a hybrid material that combines biological components from an organism's immune system, antibodies, with inorganic nanostructures, which would allow the real-time sensing and detection of bacteria in food and water supplies. In this chapter, I present molecular dynamics studies performed to quantitatively characterize the behavior of prototype immunosurfaces created with two different types of functionalized substrates. These simulations show that the functionalized substrate has an impact on the access of solution proteins to the surface and therefore to the ability of proteins to bind to the immunosurface. The work presented here should allow for the optimization of device design, leading to longer and more predictable device lifetime and enable the creation of real-time detection systems for bacterial pathogens.

In Chapter 3, I look explicitly at the interactions between a protein and the inorganic surface of a nanochannel. Reducing the size of a nanofluidic channel not only creates new opportunities for high-precision manipulation of biological macromolecules, but also makes the performance of the entire nanofluidic system more susceptible to undesirable interactions between the transported biomolecules and the walls of the channel. In this chapter, I report molecular dynamics simulations of a pressure-driven flow through a silica nanochannel that characterized, with atomic resolution, adsorption of a model protein to its surface. Although the simulated adsorption of the proteins was found to be nonspecific, it had a dramatic effect on the rate of the protein transport. To determine the relative strength of the protein–silica interactions in different adsorbed states, we simulated flow-induced desorption of the proteins from the silica surface. The analysis of the protein conformations in the adsorbed states did not reveal any simple dependence of the adsorption strength on the size and composition of the protein–silica contact, suggesting that the heterogeneity of the

silica surface may be a important factor in protein binding.

In Chapter 4, I focus on the details of the adsorption of biomolecules by studying the adsorption of small organic molecules to inorganic surfaces. Adsorption of dissolved molecules onto solid surfaces can be extremely sensitive to the atomic-scale properties of the solute and surface, causing difficulties for the design of fluidic systems in industrial, medical, and technological applications. In this chapter, I show that the Langmuir isotherm for adsorption of a small molecule to a realistic, heterogeneous surface can be predicted from atomic structures of the molecule and surface through molecular dynamics simulations. I highlight the method by studying the adsorption of dimethyl-methylphosphonate (DMMP) to amorphous silica substrates and show that subtle differences in the atomic-scale surface properties can have drastic effects on the Langmuir isotherm. The sensitivity of the method presented is sufficient to permit the optimization of fluidic devices and to determine fundamental design rules for controlling adsorption at the nanoscale.

In Chapter 5, I use our knowledge of the surface–solute interaction to parameterize a multiscale model of solute transport through micro-and nanofluidic devices. Transport of solutes through micro- and nanofluidic devices is challenging to model because the devices components typically measure in hundreds of nanometers to microns, but the adsorption of solute on the device surfaces is sensitive to the atomic-scale properties of the solute and surface. However, without an accurate model, it is difficult to optimize and design devices to have solute-specific transport. In this chapter, I present a multiscale model for simulating the transport of solutes through micro- and nanofluidic devices with atomic precision and show that it fully recreates the results of all-atom molecular dynamics simulations. I highlight the method by simulating the filling and draining of a 500-nm nanochannel and show that the atomic-scale properties of the device surfaces affects solute transport through 100-nm nanochannels. The accuracy and efficiency of the model presented here will allow for the design and optimization of micro- and nanofluidic devices for solute-specific transport.

In Chapter 6, I present research done in collaboration with the research groups of Weinstock, Sivaprasadarao, and Müller in which we use MD to develop a protocol for embedding a synthetic device in a biological environment. Porous polyoxometalate nanocapsules of Keplerate type are known to exhibit the functionality of biological ion channels; however, their use as artificial ion channel is tempered by the high negative charge of the capsules, which renders their spontaneous incorporation into a lipid bilayer membrane unlikely. In this chapter I report coarse-grained molecular dynamics simulations that demonstrate a route for embedding negatively charged nanocapsules into lipid bilayer membranes via self-assembly. A homogeneous mixture of water, cationic detergent, and phospholipid was observed to spontaneously self-assemble around the nanocapsule into a layered, liposome-like structure, in which the nanocapsule was enveloped by a layer of cationic detergent followed by a layer of phospholipid. Fusion of such a layered liposome with a lipid

bilayer membrane was observed to embed the nanocapsule into the lipid bilayer. The resulting assembly was found to remain stable even after the surface of the capsule was exposed to electrolyte. In the latter conformation, water was observed to flow into and out of the capsule as Na^+ cations entered, suggesting that a polyoxometalate nanocapsule can form a functional synthetic ion channel in a lipid bilayer membrane. The use of a synthetic device to mimic biological ion channels would permit a step-by-step study of the atomic-scale properties that allow the channels to perform their biological function, for example, selective transport of specific ions. Furthermore, such devices would assist in the development of synthetic systems for the purposes of biotechnology by exploiting the same mechanisms found in proteins.

The ability to interface solid-state technology with biological molecules presents an amazing opportunity to create revolutions in medicine and personal technology. However, there needs to be a clear a way to interface these two worlds in a way that allows the two to exist in their independent environoments while also interacting regularly through well-understood channels. To accomplish this, we must have the ability to design and optimize interactions of biomolecules and solid-state materials down to the atomic scale. In my dissertation, I have tried to show by example the methodologies that I use in my work and the range of possibilities that they present for researchers in the field. It is my hope that the research that I have performed in my doctoral studies here at the University of Illinois at Urbana-Champaign will be a template for future research and science. The work I have done here has both shown the possibilities of the MD method for studying the physical interface of biological and synthetic components, and I have developed new techniques that can be used by researchers in field to further the science and engineering of bionanotechnology and nanobiotechnology.

Chapter 2

Immunosurfaces for Bacterial Detection

Reproduced in part from: Radadia AD, Stavis CJ, Carr R, Zeng H, King WP, Carlisle JA, Aksimentiev A, Hamers RJ, Bashir R (2011) Control of Nanoscale Environment to Improve Stability of Immobilized Proteins on Diamond Surfaces. Adv. Funct. Mater. *21(6):1040-1050 [2] (Copyright © 2011 WILEY-VCH Verlag GmbH & Co.); and Carr R, Comer J, Aksimentiev A (in press) Modeling the Interface between Biological and Nanotechnological Systems. In* Simulations in Nanobiotechnology. *(Copyright © 2011 CRC Press, LLC) [41].*

Outbreaks of food and water-borne pathogens like e-coli in the general population can lead to serious illness and even death. Such outbreaks from food sources can lead to a recall of the contaminated food supplies, which can be devastating for the businesses involved [57]. These outbreaks are often caused by contamination of the food or water supply from outside sources like cattle feces [57, 58, 59], and would be preventable if there were reliable and affordable methods for on-site, real-time testing [2]. In this chapter, we discuss our collaborative effort with the research groups of of Bashir, Hamers, Carlisle and King to design and validate next-generation, hybrid bio-nano devices called "immunosurfaces," which could function as a real-time early warning system for pathegen detection in food and water supplies.

The immunosurface is an example of a hybrid material that combines biological components from an organism's immune system, antibodies, with inorganic nanostructures to perform sensing and detection of foreign substances. A schematic diagram of an immunosurface is shown in Figure 2.1 a. Antibodies are covalently tethered to an inorganic substrate so that the antibodies remain exposed in solution to preserve their activity and stay bound to a particular region of the substrate. This also prevents aggregation of the antibodies, as occurs in solution. Proteins, such as antibodies, tend to bind to inorganic surfaces strongly and nonspecifically [29]. To prevent adhesion of the antibodies to the substrates, the inorganic substrates are functionalized, or covalently coated, with a layer of protective molecules known as the functionalization layer. This functionalization layer also provides the binding site for the molecules that tether the antibodies to the surface.

Antibodies are a powerful addition to a sensor, because they bind their targets strongly and specifically,

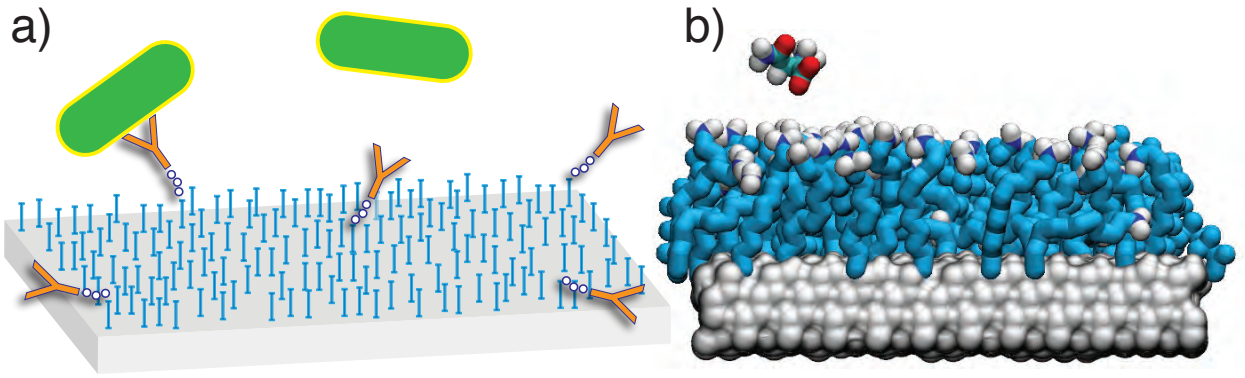

Figure 2.1: Immunosurfaces for bacterial detection. a) Schematics showing an immunosurface that consists of a solid-state substrate, such as glass or diamond (shown in grey as a gray slab), functionalized with organic coating (blue lines) to which linker molecules (blue circles) anchor antibodies (orange Ys) against pathogens like bacteria (green ovals). The individual components are not drawn to scale. b) A close up view of an all-atom model of an immunosurface used for MD simulations. The inorganic substrate (ultra nanocrystalline diamond) is shown as a grey molecular surface, the aminodecane functionalization layer is shown as tealgray chains with nitrogen in bluedark gray and hydrogen in white, and an asparagine peptide is shown as tubes with carbon in cyangray, nitrogen in bluedark gray, oxygen in redblack and hydrogen in white. The water molecules that fill the system are not shown.

in a way that is currently not possible to achieve with a purely synthetic device. Antibodies, or immunoglobulins, are proteins typically composed of two heavy chains and two light chains, which are cross-linked with disulfide bonds to form a Y-shape. The tips of the Y are known as variable regions, because the amino acid sequence varies greatly between antibodies in the same organism. This high variability gives an antibody its high specificity for the ligand, or antigen, to which it binds. However, if an antibody binds to a inorganic surface, it will rapidly lose activity as the protein becomes unstructured or oriented in a way that the antigen can't diffuse into the variable region.

In collaboration with the research groups of Bashir, Hamers, Carlisle and King, we are working to create immunosurfaces capable of detecting different strains of bacteria with the goal of monitoring the purity of water and food supplies [2]. In order to be successful, these immunosurfaces must be able to operate under physiological conditions for extended periods of time. Glass or gold substrates are typically used for anchoring proteins such as antibodies, but the polyethylene glycol and lipid bilayer coatings commonly used to prevent protein adsorption to their surfaces break down within two days [60]. Ultrananocrystalline diamond (UNCD) is a novel substrate composed of 2-5 nm diameter, phase-pure diamond grains on which alkene functionalization layers show excellent stability [1]. To compare the performance of immunosurfaces made with UNCD substrates to those made with a typical glass slide, immunosurfaces were created by covalently attaching antibodies to either UNCD films functionalized with aminodecane or Corning GAPS II amine-terminated glass (GAPSG) slides. A complete description of the experimental protocol used to create

the immunosurfaces is available in the published manuscript [2].

To test the long-term stability of the immunosurfaces operating under physiological conditions, each immunosurface was submerged in phosphate buffered saline and monitored over a period of two weeks. The half-life of the antibody activity was found to be around 4 days for the immunosurfaces created with the GAPSG substrate as compared to about 11 days for those with the UNCD substrate. While there was about 25% loss of antibodies from the GAPSG substrate in the first week, and 13% loss from the UNCD substrate in the second week, these losses alone are not enough to explain the magnitude of degradation in immunosurface performance [2]. A complete description of the experimental protocol and results is available in the published manuscript.

One explanation for this loss in performance is that the antibodies could be binding to the substrates, somehow bypassing the functionalization layer meant to prevent binding. It is known that without a protective coating of aminopropylsilane on silica or aminodecane on diamond surfaces, the antibodies can bind nonspecifically to both surfaces [61, 29], losing their conformation and specific affinity to antigens. However, it is not known how the antibody proteins could interact with the substrates in the presence of the functionalization layer and how the functionalization layer degrades in solution. While it is not possible to resolve such dynamics in solution experimentally, the molecular dynamics (MD) method offers a route to model the dynamics of such systems with all-atom precision.

To gain insight into the interactions of antibodies with the functionalized UNCD or GAPSG surfaces, we first performed MD simulations of all-atom model functionalized diamond and SiO_2 substrates. Close-ups of the simulation systems highlighting the substrates and functional layer are shown in Figure 2.2. Aminodecane-terminated diamond surfaces (2.6×10^{14} molecules/cm^2, Figure 2.2a) and aminopropylsilane-terminated SiO_2 (4.0×10^{14} molecules/cm^2, Figure 2.2b) were submerged in a 0.137 M NaCl saline solution approximating the PBS buffer used in experiment (the concentrations of other solutes, like phosphate, were too low to accurately represent in such a small volume, $5 \times 5 \times 10$ nm^3). Each system was then simulated with the MD method in the NPT ensemble for at least 40 ns. A complete description of how we modeled and simulated these systems is given in Appendix A.

By analyzing the steady-state of the MD simulations for the different model functionalized substrates, we can determine the effect of the substrate and functionalization layer on water density near the surfaces. As shown in Figure 2.2a, the aminodecane layer of the UNCD surface effectively blocks water access to the diamond substrate, whereas small pockets of water were observed in the aminopropyl layer of the SiO_2 surface (Figure 2.2b). To model the effect of variations in functionalization layer density, we have simulated UNCD and SiO_2 substrates with a range of functional group densities. Figure 2.3 shows the average density

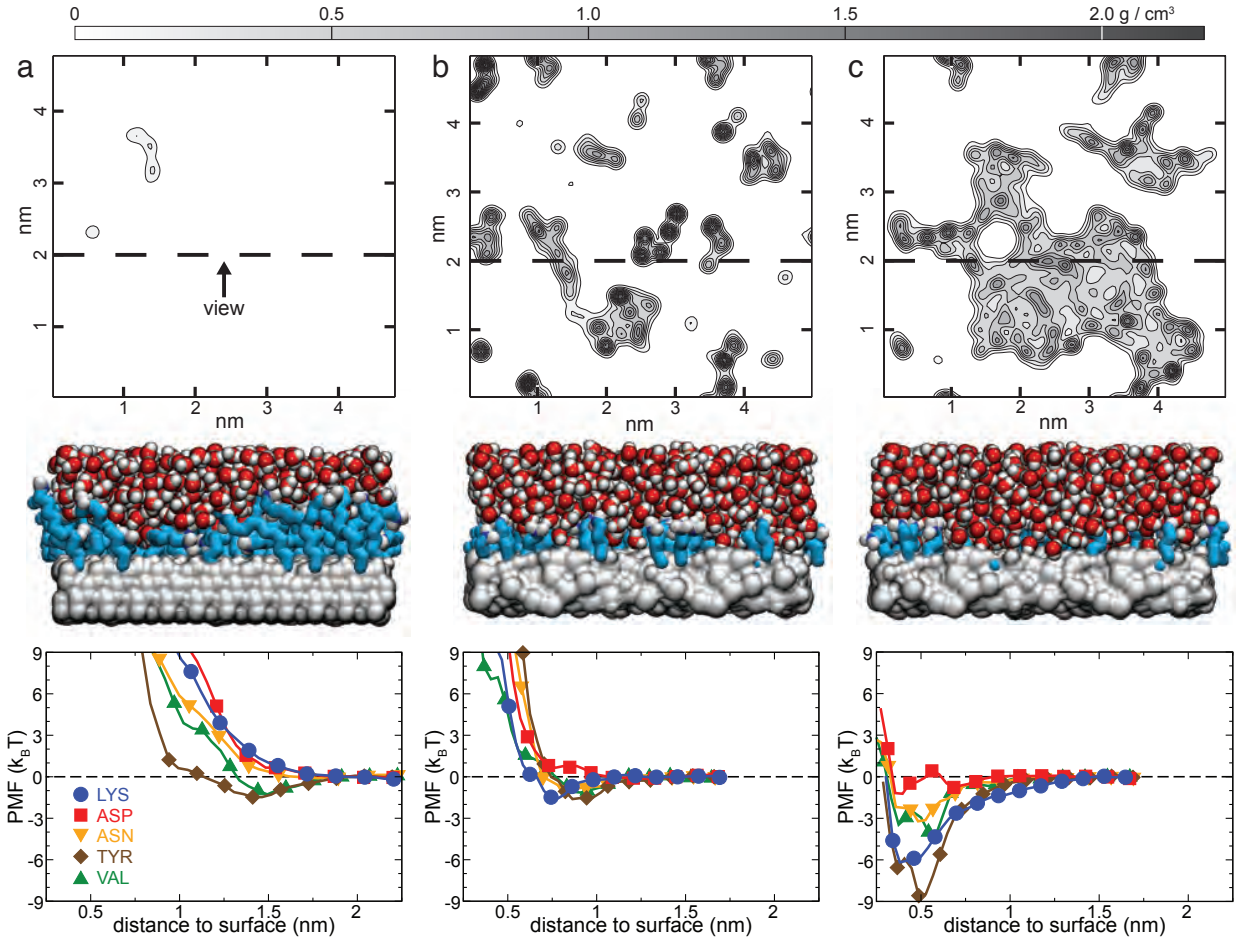

Figure 2.2: Water pockets on the immunosurfaces revealed by molecular dynamics (MD). a H-terminated UNCD coated with 2.6 x 1014 molecules/cm2 aminodecane. The top panel shows a contour plot of the water density within 0.5 nm of the diamond surface, averaged over a representative 1 ns period of the 40 ns MD trajectory. The center panel shows a cut-away view of the same surface; the location of the cut away surface is indicated at the top panel as a dashed line, UNCD is shown as a grey molecular surface, aminodecane as teal chains with nitrogen in blue and water as vdw spheres (oxygen in red and hydrogen in white). The bottom panel shows the potential of mean force (PMF) for bringing different types of amino acids from bulk solution to the surface. b, Water density (top), a cut away view (center) and the PMF profiles (bottom) for the silica surface coated with a 4.0 x 1014 molecules/cm2 layer of aminopropylsilane. Silica is shown as a gray molecular surface and other molecules are shown as in panel a. c, Water density (top), a cut away view (center) and the PMF profiles (bottom) for partially degraded the silica surface (see text). The degradation of the functionalization layer on silica creates pockets of water within the functionalization layer, which facilitates binding of amino acids as revealed by the PMF plots.

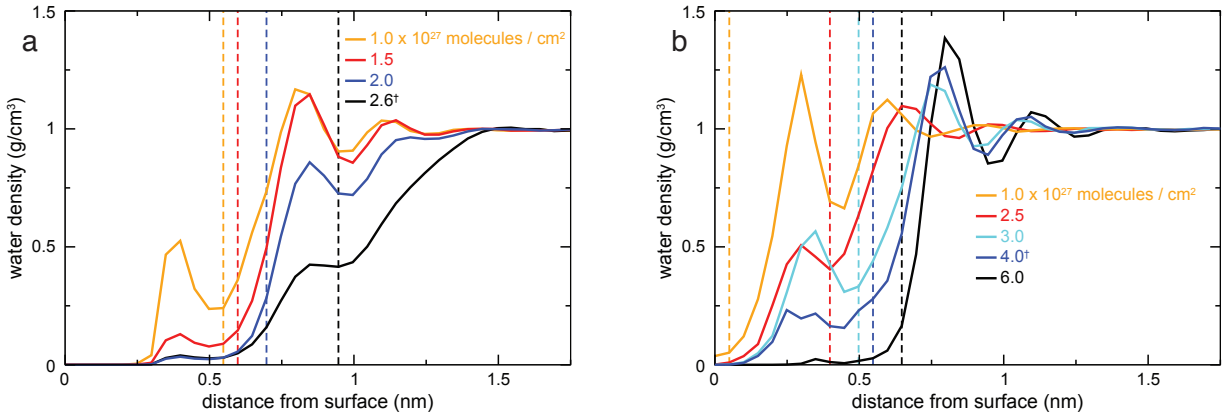

Figure 2.3: Simulated density of water near functionalized UNCD and silica substrates. a The average density of water versus the distance from the UNCD substrate coated with aminodecane to different surface density. Dashed lines indicate the distance at which the density of aminodecane becomes equal to the density of water. b The average density of water versus the distance from the silica substrate coated with aminopropylsilan to different surface density. Dashed lines indicate the distance at which the density of aminopropylsilane becomes equal to the density of water. †Corresponds to the expected experimental density of the functional groups.

of water versus the distance from the surface for each substrate for all functionalization group densities considered.

Modeling antibody proteins with all-atom MD simulations is challenging, because antibodies are large and complex proteins, which require long-timescale simulations to study even diffusive motion. To simplify the problem, we have studied protein–substrate interactions using individual amino acids in the place of an entire antibody protein. By focusing on the interactions of a substrate with individual amino acids we can estimate the interactions of a given protein with the substrate by looking at the amino-acid composition of the protein surface [29]. We have modeled the interaction of each substrate with amino acids from each of the representative types — positively charged, negatively charged, polar, nonpolar and aromatic — by creating new simulation systems with an amino acid in solution above a functionalized substrate. A typical simulation system is shown in Fig. 1 b.

To quantify the affinity of amino acids for the two substrates, we computed the potential of mean force (PMF) for each representative type of amino acid as a function of the distance from the substrate (Figure 2.2 bottom panels). The PMF calculated in such a way can be thought of as the change in free energy for bringing the amino acids from bulk solution to the respective substrates. If the PMF decreases as the amino acid nears the surface, then the interaction is attractive and the amino acid will bind to the surface if the interaction is greater than about 1 k_BT (the thermal energy); if the PMF increases as the amino acid approaches the surface, then the interaction is repulsive on average, and the amino acid will tend not to bind. For tyrosin and valine, the adhesion energy to functionalized UCND did not exceed 2 kBT, whereas charged (Lys, Asp)

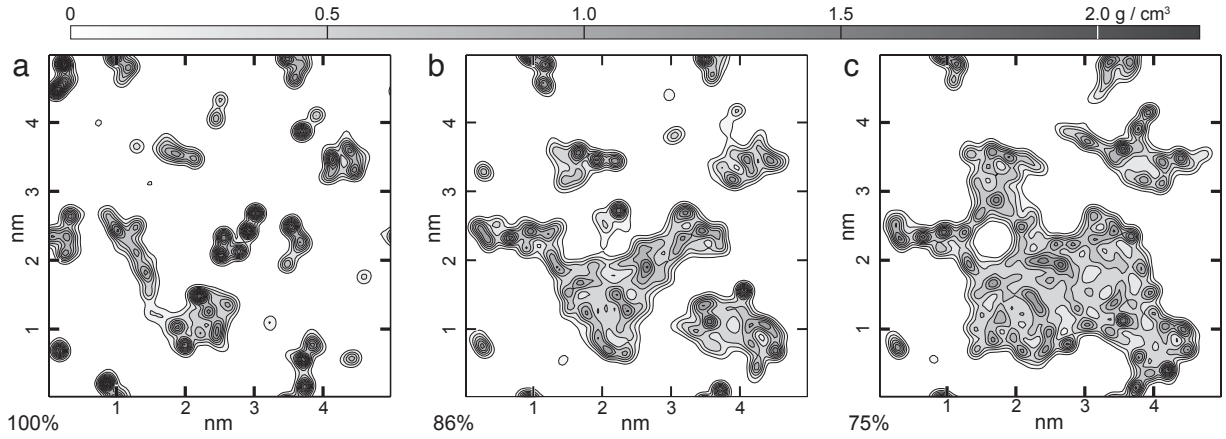

Figure 2.4: Growth of water pockets associated with degradation of GAPSG functionalization layer. a Contour plot of the water density within 0.5 nm of the silica substrate coated with 4.0 x 1014 molecules/cm2 of aminopropylsilane, averaged over a representative 1 ns period of the 40 ns MD trajectory. Starting from this structure, functional groups were removed using a procedure described in the Supporting Methods. b The water density on the silica substrate with 86% of the functionalization groups remaining. c The water density on the silica substrate with 75% of the functionalization groups remaining.

and polar (Asn) amino acids were repelled from the surface. Similar PMF profiles were obtains in the case of the functionalized silica, indicating that both surfaces are unlikely to bind proteins.

However, it is known that the GAPSG surface loses 25% of its functionalization layer when exposed to solution. To determine the effect of the degredation of the functionalization layer on protein adsorption, we modeled the degradation process by iteratively removing 25% of the functionalized groups from the surface characterized in Figure 2.2b. The degredation process is shown in Figure 2.4 and detailed in Appendix A.

Performing the same simulations as before with a simulation system containing the SiO_2 substrate with a partially degraded functionalization layer (Figure 2.2c) showed dramatically different results. The water density plot (Figure 2.2c top) revealed large pockets of water near the degraded surface, whereas the PMF for bringing amino acids from the bulk solution to the substrate through one of such pockets (Figure 2.2c bottom) indicated adhesion energies exceeding 6 kBT. Thus, degradation of the functional layer exposes patches of unprotected substrate to the solution, which considerably increases affinity of the surfaces to proteins, facilitating reduction of the antibody activity.

By performing PMF calculations for bringing one amino acid of each type from bulk solution to each substrate, we can quantitatively characterize the interactions of proteins with the substrates. Furthermore, the data we get through our MD simulations shows us not only the binding affinities, but also the origin of the differences between the amino acidsubstrate interactions. By simulating the functionalized substrates submerged in a buffer solution without the presence of protein, we can characterize the dynamics of the functionalized substrates for different functionalization densities. In the case of the functionalized UNCD

and GAPSG substrates, we find that the UNCD substrate remains dry, but water pockets form in the functionalization layer of GAPSG and increase in size for lower functionalization layer densities, providing a route for proteinsubstrate binding.

In this project, we performed MD simulations of model systems to quantitatively characterize the energetics and dynamics of antibodies on inorganic substrates. This method of simulating a model system to identify dynamical features and following up with free energy calculations to quantify specific interactions is a robust way to characterize the properties of the interface between solutes in solution and inorganic surfaces. Here, we characterized the interface between functionalized substrates and biological molecules in solution, but such methods could readily be adapted to study the interface between any solutes and any type of surface, inorganic or biological.

Chapter 3

Modeling Protein Transport through Nanochannels

Reproduced in part from Carr R, Comer JR, Ginsberg MD and Aksimentiev A (2011) Modeling Pressure-Driven Transport of Proteins through a Nanochannel IEEE Tran. Nanotechnol. *10:75–82 (Copyright © 2010 IEEE). [29]*

Transport of liquids through nanometer size structures is a ubiquitous process in modern biomedical engineering. The proposed applications of nanofluidics range from lab-on-a-chip technology [18, 6], epigenetic information analysis [62, 63], and biosensors [64, 65], to protein crystallization [16], drug delivery systems [66], and electronics [67, 68]. To transport biomolecules through nanoscale structures, hydraulic pressure gradients and/or electric fields are imposed across the device elements [18, 30]. Today, it is already possible to fabricate macroscopic length channels of a sub-ten nanometer cross-section [4], and assemble them into regular macroscopic arrays [69].

Under typical experimental conditions, pressure-driven flow of water through nanometer-size channels is laminar, as the Reynolds number of the flow is very low [30]. Under such conditions, the hydrodynamic equations of motion simplify considerably and, knowing the geometry of the channel, the properties of the flow can be easily determined [34]. The presence of proteins in the solution complicates the matter at high protein concentrations, because the protein–water mixture no longer behaves as a Newtonian fluid. Complications also arise when the size of the channel becomes comparable to the size of the protein. In the latter case, the interactions of the protein with the channel surface can dominate the protein transport and lead to spurious effects such as nonspecific adsorption, surface accumulation and eventually clogging of the nanochannel system [18].

In the simplest theoretical model of protein adsorption, a protein is assumed to bind to the surface with a certain probability so that the fractional coverage of the surface θ is described as a Langmuir isotherm $\theta = \alpha C/(1 + \alpha C)$, where C is the protein concentration and α is the Langmuir adsorption constant. The Langmuir constant incorporates all the effects of the surface properties of the channel and protein, and can be empirically associated with quantities such as the total surface area of the protein, and the charge, roughness and hydrophobicity of the channel surface.

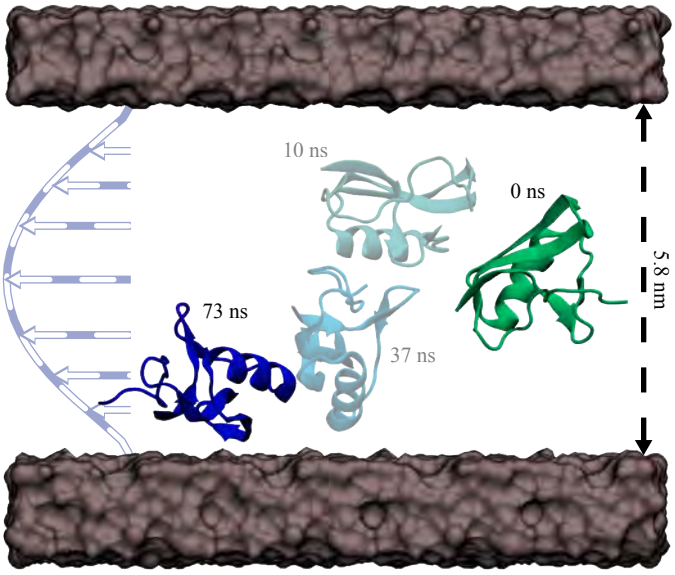

Figure 3.1: MD simulation of protein flow through a nanochannel. The protein is shown in cartoon representation; the silica nanochannel is shown as a gray molecule surface. Water and counterions are not shown. The water velocity profile is shown schematically as dashed lines and arrows. The snapshots illustrate the conformations of a protein in a typical MD trajectory.

Ideally, one would want to predict the macroscopic behavior of the protein flow through a nanochannel taking into account the microscopic properties of the protein and the nanochannel material. Molecular dynamics (MD) is a computational method that can accurately predict the forces between biomolecules and inorganic surfaces in water if their atomic structures are known. The MD method has already been applied to simulate flow and sorption of simple solutes in nanochannels within a Lennard-Jones model [70]. All-atom MD simulations have characterized DNA transport through solid-state nanopores [71, 51, 25] and the conformations of proteins near silicon surfaces [72]. The binding of individual amino acids, histidine and phenylalanine, to a platinum surface has been studied in all-atom detail using classical MD parameterized through iterative *ab initio* quantum mechanics calculations [73]. Steered-MD (SMD) has been used to study the friction of a 15-mer polypeptide on hydrophobic and hydrophilic surfaces [54] as well as protein adsorption and desorption near a hydroxyapatite surface [74].

In this manuscript, we describe the first (to our knowledge) MD simulations of pressure-driven transport of proteins through a nanochannel. We begin with a description of our simulation methodology and then test the method by simulating pressure-driven transport of water. Next, we use a model protein to characterize microscopic processes that govern protein transport through a nanochannel. For the silica channels studied in this manuscript, we find a strong tendency for the protein to spontaneously adsorb to the nanochannel surfaces. Hence, we investigate the statistical properties of the protein–silica contacts in the adsorbed states

and the process of protein desorption induced by the flow.

To produce the silica membrane used in this study, we created a $2.5 \times 2.5 \times 3.5$ nm^3 block of crystalline silica containing 500 silicon and 1000 oxygen atoms by replicating a unit cell of SiO_2. The resulting system was simulated for 20 ps at 7000 K using a $2.5 \times 2.5 \times 5.5$ nm^3 periodic cell, which produced an amorphous silica membrane with two relaxed surfaces (normal to the z-axis). The silica was simulated with the BKS potential, a two-body potential proposed by Beest, Kramer and van Santen which has been shown to reproduce some properties of silica [75, 76]. As in Vollmayer et al. [76], the form of the BKS potential was modified at small distances to prevent spurious behavior at high temperature. The Coulomb portion of the BKS potential was computed using the PME method [77], while the van der Waals portion was smoothly shifted to zero at an interatom distance of 0.55 nm. During the annealing procedure, an external force was applied to prevent the atoms from evaporating into the vacuum region. The temperature was maintained at 7000 K by a Langevin thermostat with a damping coefficient of 5 ps^{-1}. The resulting annealed silica structure structure was tiled in a four-by-four grid to create a $10.0 \times 10.0 \times 2.7$ nm^3 silica membrane consisting of sixteen identical slabs of silica.

As a model protein for this study, we used toxin II of the scorpion androctonus australis hector [78] (PDB access code 1PTX). This rather small protein consists of 64 residues and has both α-helical and β-sheet secondary structure elements. The atomic coordinates of the protein were taken from its X-ray structure; the coordinates of all missing atoms were determined according to the CHARMM [44] protein topology. To explore the stability of the protein in solution, a single copy of the protein was submerged in 10,000 TIP3P [79] water molecules with one chloride counterion to balance the positive charge of the protein—a system of 30,971 atoms. Following 2000 steps of energy minimization, the system's temperature was increased from 0 to 295 K within 25 ps by velocity rescaling. Following 0.5-ns equilibration with the protein backbone restrained to its X-ray coordinates, the system was equilibrated free of any restraints for 50 ns in the NPT ensemble.

An atomic-scale model of a nanochannel was created from the silica membrane by imposing periodic boundary conditions that defined the spacing between the nanochannel walls (the channel's height) and effectively made the channel infinitely long and wide. For our test simulations of the water flow, the volume between the walls of the channel was filled with pre-equilibrated water molecules, producing a system of 78,696 atoms.

Following a 2000-step minimization, the system was equilibrated for 2.5 ns in the NPT ensemble with the SiO_2 atoms harmonically restrained to the coordinates obtained at the end of the annealing simulation. In the silica membrane, harmonic bonds of the same strength (6950 pN/nm spring constant) were applied between

the nearest neighbors. After equilibration, the volume inside the nanochannel unit cell had dimensions of $9.9 \times 9.9 \times 5.5$ nm^3; the density of water was 1.01 g/cm^3. In the subsequent analysis of the MD trajectories, we define the boundary between the silica membrane and water to be where the average local number density of silica equals five times that of water.

To study the transport of proteins through nanochannels, we created three systems (A, B and C of 83,542, 83,398 and 83,377 atoms, respectively) by placing water, two copies of the protein and two chloride counterions inside each copy of the silica nanochannel. The resulting ionic strength and protein concentration were 5.8 mM in each nanochannel system. Such low ionic strength environment allowed us to probe protein–surface interactions in the absence of an electric double layer. As the surfaces of our nanochannel were electrically neutral, the systems considered correspond to the experimental situation at the isoelectric point of silica (pH 4–5). Our model also applies to weakly charged nanochannels, where the distance between the localized surface charges is greater than the average diameter of the protein. In the case of a highly charged surfaces, we expect to observe an electric double-layer near the surface and streaming currents arising from the water flow [80]. In each system, the proteins were placed in a random orientation with respect to the surface of the channel, representing a unique initial condition. The minimum surface–to–protein distance was 0.55 nm in system A and 1.15 nm in systems B and C. After 2000 steps of minimization, the systems were equilibrated in the NPT ensemble for 0.3 (system A) or 0.6 (systems B and C) ns, with the SiO_2 atoms restrained to their coordinates at the end of the NPT equilibration of the water-only channel system. The latter restraints had spring constants of 13900 pN/nm; the nearest neighbor atoms of the silica membrane were connected by harmonic bonds of 1390 pN/nm. Restraining the silica to the final coordinates of the NPT equilibration, rather than to the annealed structure, reduced the periodicity of the channel surface introduced by the tiling method that we used to create the systems. The dielectric constant of the silica membrane in the water-channel and protein-channel simulations were 5.5 and 4.0 (± 0.2), respectively, due to the difference in the harmonic restrains that applied to silica [81]. After equilibration, the unit cell of each system had dimensions of $10.0 \times 10.0 \times 5.8$ nm^3.

To induce water flow through the nanochannel, a constant pressure difference was created by applying a lateral force to all the water molecules in the system. As detailed in Zhu et al. [82], applying a lateral force, F, to N atoms results in a pressure difference across the system of

$$\Delta P = N \cdot F/A, \tag{3.1}$$

where A is the area perpendicular to the applied force.

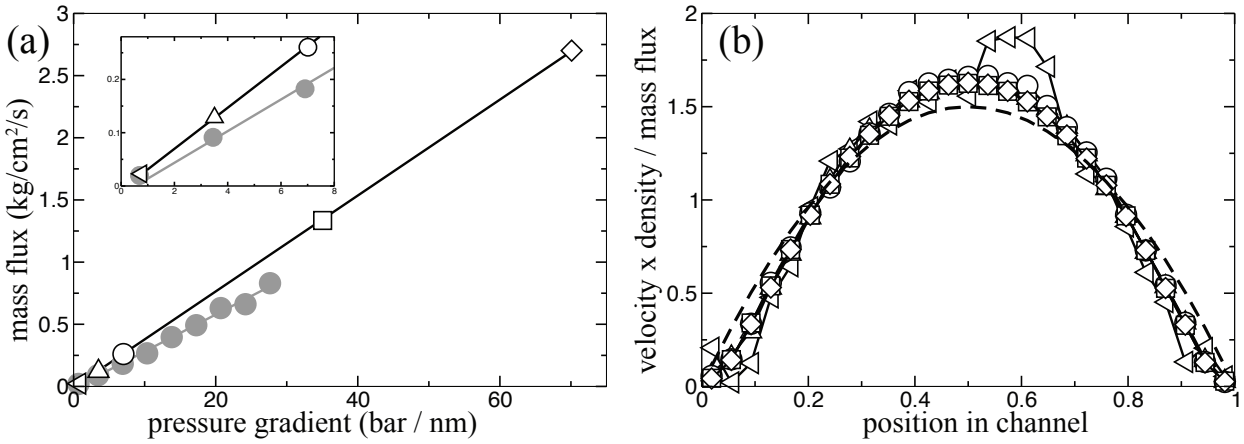

Figure 3.2: MD simulations of water flow through a nanochannel. a) Mass flux versus pressure gradient in the water-only (black) and protein–water (gray) systems. The inset shows an enlarged view of the main plot at small pressure gradients. b) Simulated velocity profile of the water flow. The dimensionless average velocity of flow is plotted versus dimensionless position in the channel (see text). The normalized velocity profiles are shown for five simulations at different pressure gradients; the symbols are defined in panel a. The theoretical Poiseuille flow profile is shown as a dashed line. The simulated absolute flow velocities at the center of the nanochannel were 0.39, 2.4, 4.6, 24, and 48 nm/ns for the pressure gradients of 0.70, 3.5, 7.0, 35 and 70 bar/nm, respectively.

To test our computational method, we simulated the flow of water through a nanochannel at five different pressure gradients. Each simulation lasted from 10 to 25 ns. Figure 3.2 summarizes the results of these simulations.

First, we determined that the mass flux of water through the nanochannel scales linearly with the applied pressure gradient within the entire range of pressure gradients (spanning three orders of magnitude) tested, Figure 3.2 a. The mass flux was computed by measuring the average displacement of all atoms in the nanochannel over a time interval Δt [83] divided by the channel's cross sectional area A_{channel}:

$$Mass\ Flux = \frac{1}{A_{\text{channel}}} \sum_{i=1}^{N_{\text{atoms}}} \frac{M_i \Delta x_i / \Delta t}{L_{\text{channel}}}, \tag{3.2}$$

where M_i is the mass of atom i, L_{channel} is the dimension of the unit cell in the direction of the flow and Δx_i is the displacement of atom i in Δt.

Next, we investigated the dependence of the water velocity on the distance from the surface of the channel. In Figure 3.2 b, we plot the dimensionless average water velocity (scaled with its density and normalized by the total flux) versus the distance from one surface of the channel normalized by the channel height. The simulated dimensionless flow profiles at five pressure gradients overlap, indicating a linear scaling of the flow profile with the pressure gradient. The water velocity profiles were calculated through the following process. First, the velocity of each water oxygen along the direction of the pressure gradient was computed from its

displacement over a 10-ps interval. Next, these velocities were grouped into bins spaced by 0.2 nm along the height of the channel. Water molecules that moved between the bins were given fractional counts for the respective bins. Finally, the velocities were averaged over each bin in the last 9 to 19 ns of each simulation.

The simulated water profiles could be accurately described as a Poiseuille flow through an infinite slit [34]:

$$U_p(x) = \frac{\Delta p}{8\eta L}\left(h^2 - 4x^2\right), \tag{3.3}$$

where η is the viscosity, $\Delta p/L$ is the pressure gradient, h is the channel height and x is the position in the channel, defined such that $x = \pm\frac{h}{2}$ at the channel's surface. The dimensionless profile of the Poiseuille flow is shown in Figure 3.2 b as a dashed line. To compute the theoretical curve, we used the simulated viscosity of our water model (TIP3P) at 298 K [84]. Some deviations from the theoretical predictions were observed near the surface of the channel, where the breakdown of the continuum description could be expected. Considerable deviations of the flow profile from the master curve were observed in the simulation at the smallest pressure gradient (0.70 bar/nm). The time scale of this simulation (20 ns) was too short for the flow velocity to attain a stable, symmetric profile, although the total water flux already attainted a value consistent with the linear pressure–flux dependence, Figure 3.2 a. Even though our temperature control applied only the silica membrane, the temperature of the entire system remained within 1.2% of that observed in the absence of the flow.

Once we had tested our protocol for simulating a pressure-induced flow through a nanochannel, we applied this method to study the transport of proteins. In our first simulation, the two proteins were initially positioned near the surface with a minimum surface–to–protein distance of 0.55 nm (system A). For this system, we performed two simulations applying different pressure gradients, 0.69 bar/nm and 3.5 bar/nm, lasting 97 and 86 ns, respectively. The proteins became bound to the surface of the nanochannel within 10 and 32 ns from the beginning of the simulations at 0.69 and 3.5 bar/nm pressure gradients, respectively. As depicted in Figure 3.1, the proteins twist and roll as they flow through the nanochannel, adopting many conformations before eventually binding to the surface.

To determine the influence of the initial conditions on the protein orientation in the adsorbed state, we simulated two additional systems (B and C) that had the proteins positioned further away (1.15 nm) from the surface. These simulations were performed applying a pressure gradient of 0.69 bar/nm for 62 (system B) and 57 (system C) ns. Thus, from the four simulations of two proteins each, we obtained eight independent protein trajectories in total. The protein motion through the channel is characterized in Figure 3.3 a, which shows the closest distance between the protein's α-carbon atoms and the silica surface. The graph indicates

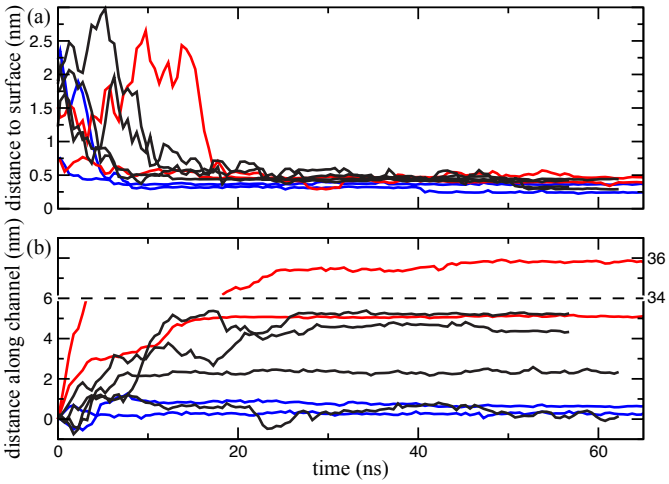

Figure 3.3: Spontaneous adsorption of proteins to the nanochannel surface. (a) The shortest distance between the channel surface and any α-carbon atom of the protein. (b) The distance travelled by a protein in the channel in the direction of the flow. The center of mass of the protein is plotted relative to the initial position of the protein in the channel. The data for the two proteins of system A were obtained at two pressure gradients, shown in blue (0.69 bar/nm) and red (3.45 bar/nm); the data for the proteins in systems B and C were obtained at 0.69 bar/nm and are shown in black. Only the first 65 ns of the simulations of system A are shown.

that all proteins eventually bound to the surface. To determine if the proteins could tumble or slide along the surface, we plotted in Figure 3.3 b the distance each protein traveled along the direction of the flow. The figure indicates that regardless of the initial conformation and the applied pressure gradient, the distance travelled by a protein along the channel reached a constant value, meaning that all proteins eventually adhered to the surface and became immobile. Figure 3.3 a and b also show that some proteins did not bind to the surface immediately after they first encountered the surface. Rather, they rolled and slid along the surface for some time before becoming immobile.

Visual inspection of the obtained trajectories revealed that the proteins bound to the surface of the nanochannel in different conformations. To determine if there was any underlying order, we inspected the amino acid makeup of the protein parts that made the contact with the silica membrane. We defined an amino acid to be in contact with the silica surface if any of its non-hydrogen atoms were located within 5 Å (center to center) of any silica atom. An amino acid was considered bound to the surface if its contact with the surface lasted more than 75% of the time interval that any residue of the protein was in contact with the surface.

Table 3.1 and Figure 3.4 summarize the results of our analysis. In eight binding events, different sets of amino acids were found to form contacts with the silica surface. The contacts were found to contain clusters of neighboring residues, indicating that, in addition to any specific interactions between silica and particular

System-Protein	∇P (bar/nm)	# Res. in contact	Bound residues	Surface area (nm^2)
A-1	0.69	8.0 ± 1.4	Asp9 Asp53 His54 Arg56 Cys63 His64	4.0 ± 0.4
A-2	0.69	6.0 ± 1.4	Val1 Asp53 Pro60 His64	4.9 ± 0.7
A-1	3.5	8.5 ± 1.4	Asp9 Val10 Asn11 Lys30 His54 Arg56 His64	5.8 ± 1.1
A-2	3.5	13.0 ± 1.1	Arg18 Asn19 Glu32 Ser33 Tyr35 Cys36 Gln37 Trp38 Ala39 Tyr49 Lys50 Arg62 His64	6.5 ± 0.5
B-1	0.69	6.4 ± 1.2	Asp9 Lys28 Lys30 His54 Arg56	4.3 ± 0.4
B-2	0.69	8.7 ± 1.3	Ala39 Ser40 Pro41 Tyr42 Gly43 Arg62 His64	4.5 ± 0.6
C-1	0.69	8.9 ± 1.4	Asp53 Arg56 Lys58 Pro60 Arg62	5.3 ± 0.8
C-2	0.69	9.6 ± 1.2	Asp3 Glu32 Tyr35 Trp38 Ala39 Tyr49 Lys50	5.1 ± 0.4

Table 3.1: Properties of the protein–silica contacts formed by spontaneous adsorption.

types of amino acids, the three-dimensional structure of the protein plays a major role in determining which amino acids bind the surface. The protein–silica contacts were found to involve from 6 to 13 protein side chains and have contact area from 4.0 to 6.5 nm^2. The binding site were found to contain all types of amino acids—acidic, basic, polar, nonpolar, aromatic; each binding site contained at least one charged residue.

In Figure 3.4, we plotted the fractional area of the binding sites contributed by the amino acids of different types and compared that to the amino acid content of the protein surface in bulk water. The plot indicates that residues with bulky side chains are more likely to bind silica than residues with smaller side chains. This is likely due to the fact that side chains with more atoms have a higher probability of encountering the silica membrane than side chains with fewer atoms. Apart from this observation, the binding did not appear to involve any particular set of residues, nor was there any indication that certain residue types bind the surface more frequently than others. Thus, we concluded that the protein binding observed in our simulations was nonspecific.

To determine the relative binding strength of each protein conformation, we attempted to remove the proteins from the surface by gradually ramping up the pressure gradient. Initially, we increased the pressure gradient in the simulations of systems A, B and C from 0.69 to 3.45 bar/nm, the same pressure gradient

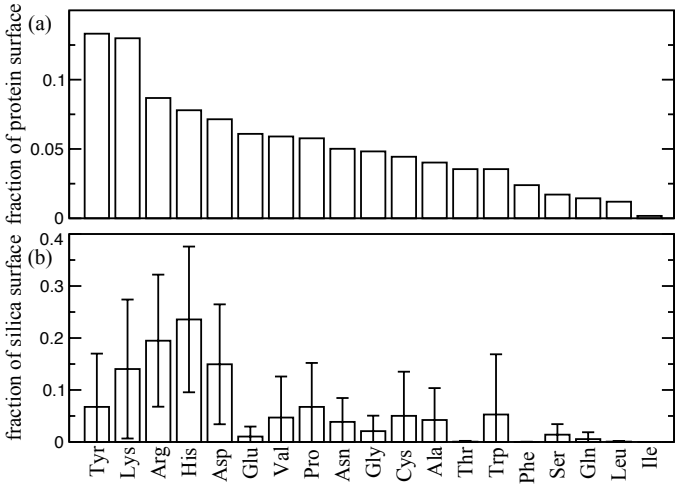

Figure 3.4: Amino acid content of protein–nanochannel contacts. (a) Fractional area of the solvent accessible surface of the protein in bulk water associated with each amino acid type. The solvent-accessible area was calculated using VMD [85] and a solvent probe radius of 1.4 Å. The values given were obtained by averaging over an ensemble of instantaneous conformations observed within the last 30 ns of a 50 ns trajectory sampled every 5 ps. (b) Fractional area of the protein–silica contact associated with each amino acid type. The contact area was defined as a solvent-accessible area of a silica membrane located within 5 Å of the protein. The data shown were obtained by averaging over ensembles of conformations observed in all bound states, weighted with the respective average area of the contact and sampled every 5 ps. The sum of the fractional area over all amino acid types is greater than 1 because the same silica atoms can be in contact with more than one amino acid. The protein considered in this work does not contain methionine residues.

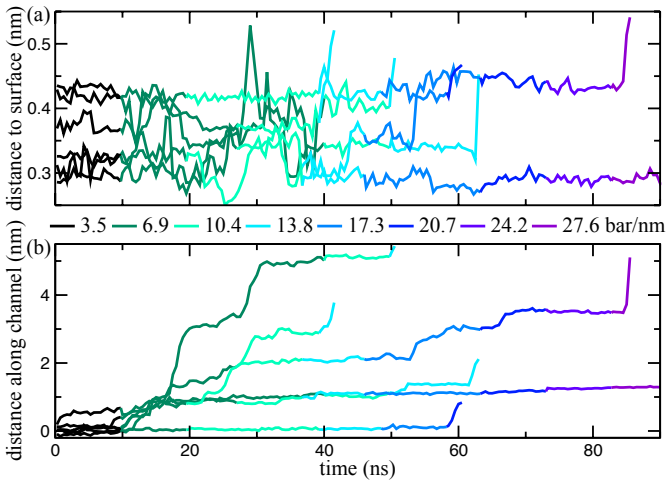

Figure 3.5: Flow-induced desorption of proteins bound to nanochannel surfaces. (a) The shortest distance between the channel surface and any α-carbon atom of the protein. (b) The distance travelled by a protein in the channel in the direction of the flow. The center of mass of the protein is plotted relative to the initial position of the protein in the channel. During desorption, proteins were observed to roll along the channel surface and occasionally rebind before entering bulk water. The data are colored according to the pressure gradient.

used in the second simulation of system A. The conformations of the two proteins in each systems remained stable within the 10 ns simulation at the new pressure gradient: neither unbinding nor rolling was observed. Subsequently, we increased the pressure gradients (and hence the shear force of the flow on the protein) in 3.45 bar/nm increments, running the simulation at each value until the proteins either detached from the surface or remained stably bound for at least 10 ns. If, upon switching to a higher pressure gradient value, the protein was observed to roll on the surface and rebind at a different location, the simulation was run until the protein was stable for 10 ns in the new conformation. From these simulations, we have calculated the mass flux of the protein–water mixture in the nanochannel as a function of the pressure gradient and plotted the result in Figure 3.1 a, alongside the data for the pure water system. As in the case of the pure water system, the protein solution's mass flux was found to increase linearly with the pressure gradient, but with a slightly smaller slope, presumably because of the higher effective viscosity of the water-protein mixture.

System-protein	∇P (bar/nm)	number of contact residues	Contact residues	Contact area (nm^2)
A-2	3.5	6.5 ± 1.3	Val1 Asp53 Pro60 Cys63 His64	4.9 ± 0.4
B-2	3.5	8.7 ± 1.3	Ala39 Ser40 Pro41 Tyr42 Gly43 Asn44 Arg62	4.4 ± 0.6
C-1	6.9	9 ± 2	Asn11 Asp53 His54 Arg56 Pro60 Arg62	6.2 ± 1.0
A-2*	10.4	12.0 ± 0.8	Arg18 Asn19 Ala20 Asn23 Glu32 Ser33 Tyr35 Ala39 Ser40 Pro41 Tyr42 Lys50	5.4 ± 0.3
C-1*	10.4	6.5 ± 1.5	Asp9 Lys30 His54	4.6 ± 0.7
A-1	13.8	9 ± 2	Asp9 Val10 Glu24 Lys28 Lys30 Arg56 Arg62 Cys63 His64	4.3 ± 1.3
B-2*	13.8	13.8 ± 1.6	Asp9 Val10 Phe15 Gly17 Arg18 Tyr21 Ala39 Ser40 Pro41 Arg62 His64	7.7 ± 0.7
C-2	17.3	11.3 ± 1.1	Asp3 Glu32 Tyr35 Trp38 Ala39 Tyr47 Tyr49 Lys50 Arg62 His64	6.6 ± 0.5
B-2*	24.2	9.8 ± 0.9	Asp8 Asp9 Val10 Arg18 Tyr21 Glu24 Lys28 Arg56 Arg62	5.0 ± 0.4
B-1†	27.6	13.0 ± 0.5	Val1 Lys2 Asp8 Asp9 Val10 Asn11 Asp53 His54 Arg56 Thr57 Lys58 Arg62 His64	6.6 ± 0.2

Table 3.2: Properties of the protein–silica contacts before unbinding from the surface of the nanochannel. ∇P specifies the highest pressure gradient for which the proteins remained bound to the surface. Proteins listed more than once were observed to unbind and rebind. * Conformations due to rebinding. † This protein did not unbind.

The protein desorption process is characterized in Figure 3.5, which is analogous to Figure 3.3. The protein displacement in the direction normal to the surface of the channel is plotted in Figure 3.5 a, which shows the closest distance between any α-carbon atom of the protein and the silica surface. The protein displacement in the direction of the flow is plotted in Figure 3.5 b. The trajectories terminate when the proteins unbind. Figure 3.5 reveals that desorption of the proteins occurs in a wide range of pressure gradients: from 6.9 to 27.6 bar/nm. One protein failed to desorb even when the pressure gradient reached 38.0 bar/nm; this simulation was terminated after 117 ns.

As the pressure gradients increased, the proteins were observed to change their conformations presumably because of the increased shear stress. Thus, over the course of the simulations, the center of mass of the bound proteins moved, on average, 0.3 nm closer to the silica surface, whereas the number of amino acid chains in contact with the surface and the contact area increased by 20–60 and 11–37 %, respectively. The changes in the conformation of the protein that failed to unbind, B1, were much larger, 53 and 225 %, respectively. It appears that the shear force of the flow can push the bound proteins toward the surface. In contrast, the conformations adopted by the proteins that rebound to the silica surface after sliding or rolling showed little or no change in the number of contacts and the contact area as the shear stress increased.

Table 3.2 lists the properties of the protein–silica contacts in the last stable conformation observed before the proteins detached from the surface. The proteins that were observed to unbind and rebind are listed multiple times. The protein that did not unbind (B1) is shown as a reference. Table 3.2 does not reveal any simple correlation between the number of protein residues bound to the silica surface, their composition and contact area with the ability of the protein-silica contacts to withstand the shear force of the flow. These results reinforce our conclusion that, in our simulations, the proteins bound nonspecifically to the silica surface. While we have thoroughly investigated the properties of the protein residues involved in binding the silica surface, our analysis did not take into account the atomic-scale heterogeneity of the silica. As each protein was bound to a different patch of the silica surface, the observed variations in the strength of the protein binding may, at least partially, be attributed to the local variation of the surface properties of silica, such as the surface roughness and the number of dangling bonds [49].

In this study, we have modeled the transport of proteins through silica nanochannels, and investigated the modes by which they bind to the silica surface. Reducing the strength of protein–surface interactions and/or designing surfaces to bind specific types of proteins is a task of outstanding importance. Through the use of combinatorial phage display techniques, researchers have been able to design short peptides that bind specifically to particular inorganic surfaces [86, 87, 88, 89]. These peptides can be included in a given protein to give it a moiety that will bind specifically to inorganic surfaces such as silica [90]. In contrast to

such specialized proteins, in our simulations we observed nonspecific binding of our model protein to silica. We have shown that such nonspecific binding can be of very high affinity and thus can have a dramatic effect on protein transport. Reducing or eliminating such nonspecific binding is one of the most challenging problems in the development of the next generation of nanofluidic devices for applications in biotechnology.

Ideally, one would want to predict the adsorption constant of a given protein simply from the knowledge of its atomic structure and material properties of the nanochannel. In order to design surfaces that minimize nonspecific binding, one needs to understand the mechanisms by which individual amino acids influence the affinity of the entire protein to an inorganic surface. By combining such information with the knowledge of the atomic structure of the protein, the binding affinity of the entire protein could be described in statistical terms, which would have numerous applications in nanobiotechnology [91, 92, 38, 93]. The availability of atomic-scale models for inorganic surfaces in aqueous environments would be critical to the success of such an approach, as their heterogeneous nature could only then be accurately taken into account.

Chapter 4

Microscopic perspective on the adsorption isotherm of a heterogeneous surface

Reproduced in part from Carr R, Comer J, Ginsberg M. D, Aksimentiev A. (2011) Microscopic perspective on the adsorption isotherm of a heterogeneous surface. J Phys Chem Lett *2:1804–1807.*

Adsorption of solutes from a liquid phase to a solid substrate is a process ubiquitous across industries and technologies, yet it is often difficult to predict and control. Specific adsorption has many applications, ranging from clarification in winemaking [94], to dialysis, filtration and the treatment of acute poisoning [95], to the purification of proteins [96]. At the same time, uncontrolled adsorption contributes to loss of product to vessel surfaces, clogging of small constrictions in coronary stents [97] or microfluidic devices [18] and performance deterioration of biosensors [98, 2]. The microscopic nature of adsorption phenomena requires the atomic structures of the solutes and the substrates be taken into account in order to design substrates to have set adsorption properties for specific solutes. In this communication, we describe a computational method for prediction of the adsorption isotherm specific to the atomic-scale details of the solute, solvent and substrate. Building on previous work in this area [49, 50, 52, 53, 92, 54, 55, 2], we demonstrate utility of classical molecular dynamics (MD) simulations for prediction of macroscopic, experimentally accessible adsorption behavior of realistic, heterogeneous surfaces.

Monolayer adsorption is commonly described by the Langmuir isotherm

$$\theta = \frac{\alpha C_{\text{bulk}}}{1 + \alpha C_{\text{bulk}}}, \tag{4.1}$$

where θ is the fractional area of the surface covered by the adsorbed solutes, C_{bulk} is the solutes' bulk concentration and the empirical parameter α specifies the solute–surface affinity, also known as the Langmuir constant. For a homogeneous surface containing a lattice of identical binding sites and solutes with no self-interaction, the Langmuir description is exact, with α being equal to the inverse of the bulk concentration at which half the surface is covered with the solute. In practice, most surfaces are neither periodic nor bind solutes with the same affinity everywhere on the surface, and hence the Langmuir constant α is determined from experiment. Below we demonstrate that, in the case of a realistic heterogeneous surface, the Langmuir

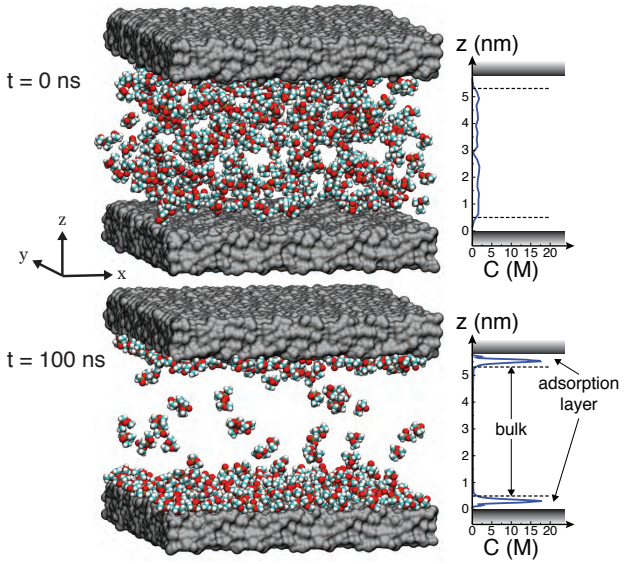

Figure 4.1: Molecular dynamics simulations of adsorption. (Top) Typical starting configuration containing randomly placed DMMP solute (shown as vdW spheres), two silica slabs (shown as gray molecular surfaces) and water (not shown). The plot specifies the average concentration of the solute along the z axis. (Bottom) The same system at the end of a 100-ns MD trajectory.

isotherm can be directly obtained from MD simulations and the Langmuir constant α can be computed from a 3-dimensional potential of mean force (3D PMF) for the solute near the surface.

To simulate surface adsorption in all-atom detail, we have modeled a small, enclosed chamber of solution, using dimethyl methylphosphonate (DMMP) as a model solute. Figure 4.1 (top) shows a typical starting configuration of a simulation system consisting of a 10×10 nm^2 slab of amorphous silica (SiO_2), tiled from sixteen identical 2.5×2.5 nm^2 patches, enclosing a 5-6 nm tall, well-mixed solution of DMMP. The system was made effectively infinite in the $x - y$ plane using the periodic boundary conditions. A pressure gradient was imposed in one of the directions, producing a Poiseuille-type flow (the magnitude of the flow had negligible effect on adsorption) [29]. A complete description of the system setup and the simulation protocols is provided in Appendix C.

After initial energy minimization and equilibration, the system was simulated for ∼100 ns using the classical MD method [43]. As the simulation progressed, the concentration of DMMP in the center of the chamber gradually reduced as DMMP adsorbed to the surfaces of the slab. Eventualy, the system reached a dynamic equilibrium state, Figure 4.1 (bottom), which we used to calculate the average density of adsorbed solutes n and the bulk concentration C_{bulk}, different from the starting concentration. Here we defined a solute as adsorbed at the surface if its center of mass lies within 0.5 nm of the surface. As detailed in Figure 4.1, the equilibrium profile of DMMP concentration exhibits pronounced maxima near both surfaces of the slab and is constant elsewhere, and hence we refer to these two regions as the adsorption layer and

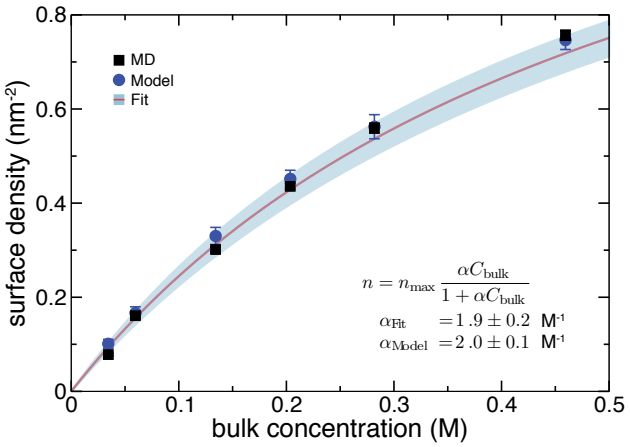

Figure 4.2: Adsorption isotherm. Black squares indicate the data directly obtained from all-atom MD simulations. The solid line shows the fit of the Langmuir isotherm to the MD data; the expected error of the fit is shown in light blue. Blue circles show the predictions of the theoretical model based on the 3-dimensional potential of mean force (see text).

bulk solution, respectively.

To obtain the adsorption isotherm, we repeated the above simulation having different starting amounts of DMMP in the chamber. The resulting dependence of the density of adsorbed solutes on the bulk concentration is shown in Figure 4.2 (black squares) along with the fit of the data to the Langmuir isoterm, 4.1 (solid line). The plot shows that the simulated adsorption obeys the Langmuir isotherm. To extract the Langmuir constant, independent MD simulations were performed to determine $n_{\max}$—the maximum adsorption density of DMMP, which is required to compute the fractional surface coverage θ using adsorption surface density n as $\theta = n/n_{\max}$ (see Figure C.1).

Thus, we have shown the utility of brute-force MD for predicting the Langmuir constant of a heterogeneous surface. Being essentially the numerical equivalent of an actual experiment, such an approach may not be optimal for designing surfaces with set adsorption properties, as it would require a large number of trials.

To link the local atomic-scale properties of the substrate and the solvent to the global adsorption properties of the surface, we express the Langmuir isotherm in terms of microscopic quantities. For a low-concentration solution, the Langmuir isotherm, 4.1 reduces to

$$\theta = \alpha \cdot C_{\text{bulk}}, \tag{4.2}$$

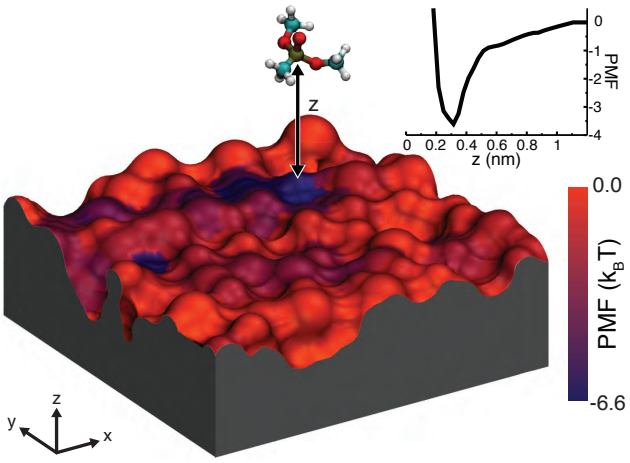

Figure 4.3: Potential of mean force (PMF) of a DMMP solute in proximity to a heterogeneous surface. The silica slab is shown as a molecular surface colored by the local minimum value of the PMF in the direction normal to the slab (see text). Inset shows the PMF averaged over the x-y plane as a function of the distance from the surface.

and the concentration near the surface can be obtained as

$$C(\vec{r}) = C_{\text{bulk}} e^{-F(\vec{r})/k_{\text{B}}T}, \tag{4.3}$$

where $F(\vec{r})$ is the free energy for a solute at position $\vec{r}$, set to zero in the bulk. By integrating the solute concentration over the adsorption layer (Figure 4.1) and dividing by the area of the surface, A_{surface}, the density of molecules adsorbed at the surface is

$$n = \frac{C_{\text{bulk}}}{A_{\text{surface}}} \int_{\text{adsorbed}} d\vec{r}\, e^{-\beta F(\vec{r})}. \tag{4.4}$$

Using $\theta = n/n_{\text{max}}$, we find $n = \alpha \cdot C_{\text{bulk}} \cdot n_{\text{max}}$, or

$$\alpha \cdot C_{\text{bulk}} \cdot n_{\text{max}} = \frac{C_{\text{bulk}}}{A_{\text{surface}}} \int_{\text{adsorbed}} d\vec{r}\, e^{-\beta F(\vec{r})} \tag{4.5}$$

$$\alpha = \frac{1}{n_{\text{max}} \cdot A_{\text{surface}}} \int_{\text{adsorbed}} d\vec{r}\, e^{-\beta F(\vec{r})}, \tag{4.6}$$

which expresses the Langmuir constant α in terms of the maximum adsorption density n_{max} and the free energy $F(\vec{r})$. In this expression, n_{max} contains the information about the high-concentration behavior of the system.

To determine the free energy of a solute as a function of its position near the surface, we performed umbrella-sampling simulations [99] of DMMP and the silica slab and obtained the 3D PMF using the

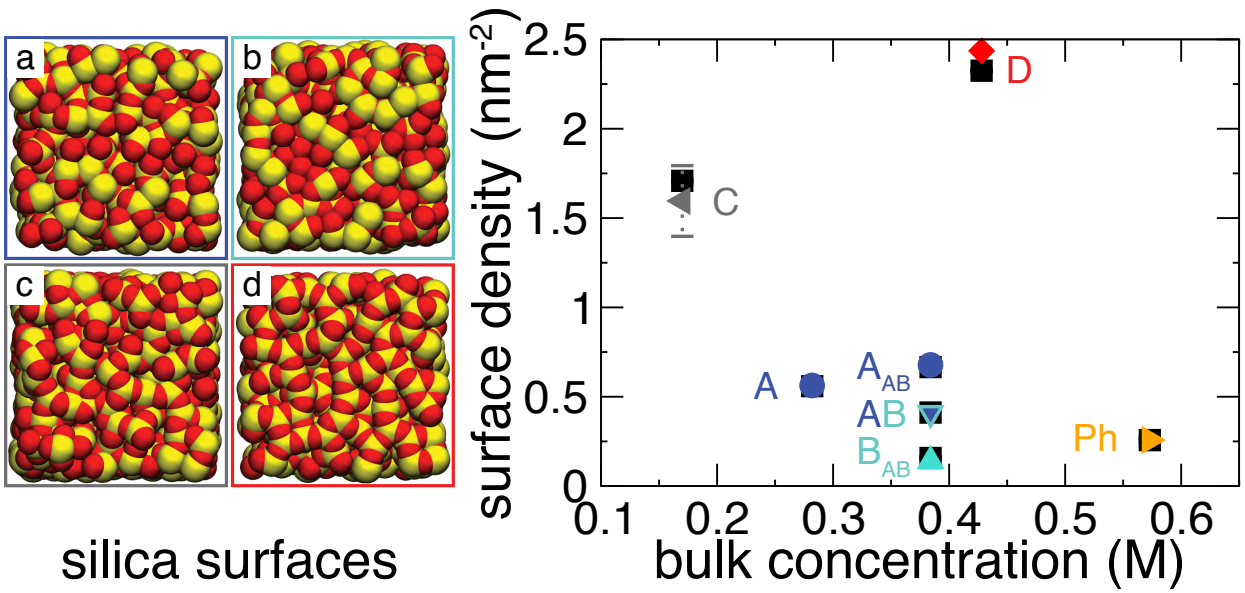

Figure 4.4: Test of the 3D-PMF model of adsorption using different heterogeneous surfaces. (a–d) Atomic models of four different surfaces of silica slabs. Oxygen and silicon atoms are shown as red and yellow vdW spheres, respectively. (e) Test of the model. Black squares indicate data directly obtained from MD simulations, other symbols show predictions of the 3D-PMF model. Labels A, B, C, and D indicate the surfaces the data were obtained for (also shown as panels a–d); AB labels the system that combined two different surfaces (A and B, labeled A_{AB} and B_{AB}), and Ph indicates a phantom surface.

weighted histogram method (WHAM) [100] generalized to three dimensions (see Appendix C). Such 3D PMF maps can be thought of as the change in free energy for bringing the solute molecule from the bulk solution to any point near the surface and reveals the variation in adsorption strength over the surface.

Figure 4.3 illustrates the results of such calculations, showing the silica surface colored by the local minimum value of the PMF for each (x,y) point. For this particular 2.5×2.5 nm^2 patch of amorphous silica surface, the depth of the PMF near the surface varies from 0 to -6.6 k_BT. The surface appears to have low and high affinity regions, highlighting its heterogeneous nature. The inset in Figure 4.3 shows the PMF as a function of z, averaged over the $x - y$ plane, revealing the short-range nature of the interaction. The shape of the average PMF is in accord with the steady-state concentration profile of DMMP in Figure 4.1.

Using 4.6, we have computed the Langmuir constant from the 3D PMF map shown in Figure 4.3 and the previously-determined maximum adsorption density n_{max}. The value predicted by the 3D PMF model: $\alpha_{Model} = 2.0 \pm 0.1$ M^{-1}, is in excellent agreement with the fit to the adsorption simulation data: $\alpha_{Fit} = 1.9 \pm 0.2$ M^{-1}, where the errors were estimated taking into account the uncertainty of determining n_{max} and the 3D PMF, or the surface concentration in the brute force MD data, respectively. Consequently, adsorption densities predicted by the model agree with the results of brute-force MD in the entire range of studied concentrations, Figure 4.2.

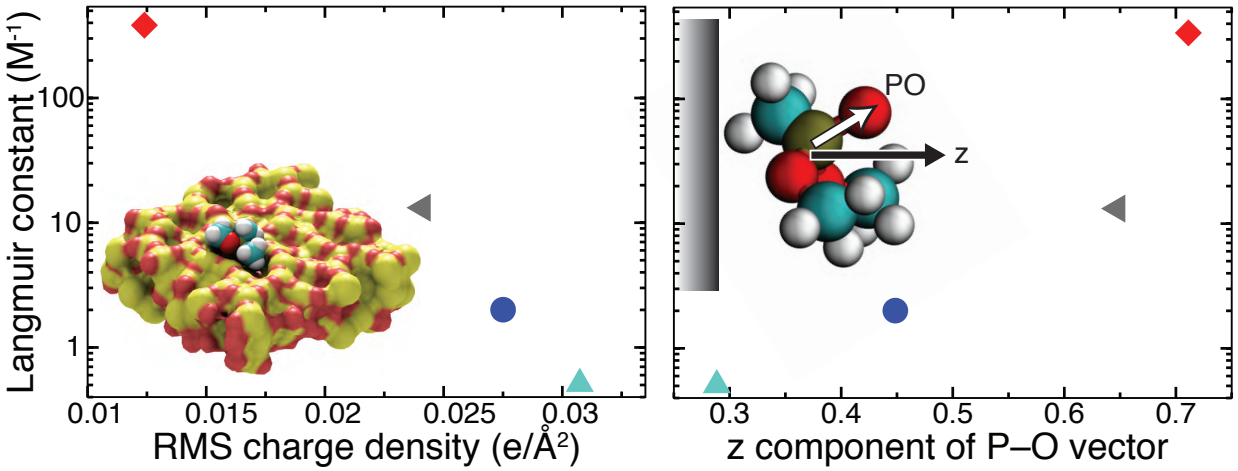

Figure 4.5: Atomic features affect adsorption. For the four silica surfaces, the Langmuir constant is plotted as a function of (a) the root mean square (RMS) surface charge density and (b) the conformation of the adsorbed solutes. The latter is characterized by the average projection of the P–O bond unit vector onto the normal of the slab. Colors and symbols are the same as in Figure 4.4 e. Inset to (a) shows a DMMP molecule bound to a small pocket (surface D).

To test the robustness of the 3D PMF model against variations in the atomic-scale features of the substrate surface, we repeated both brute-force and 3D PMF calculations for three additional amorphous silica slabs that had different surface features introduced by thermal annealing [49] (see Appendix C). Figure 4.4 (a–d) illustrate the atomic structures of the four surfaces; data presented in Figures 1, 2 and 3 pertain to surface A. Surface B was simulated in a chamber constructed using both surface A and B, which is referred to as system AB. For comparison, the same calculations were performed for a frictionless hydrophobic surface [81] (Ph) devoid of any atomic-scale features.

Figure 4.4 e compares the predictions of the 3D PMF model with the results of the brute-force MD simulations. In all cases, the two models produced quantitatively consistent results. Because of the considerable difference in the overall affinity of the surfaces to DMMP, to make the comparison statistically significant, different-affinity systems were simulated at different bulk concentrations of the solute.

In 4.6, $n_{\max}$ is assumed to be a constant global property of the surface, an assumption that may not hold for extremely heterogeneous or patterned surfaces. In these cases, constant $n_{\max}$ may still approximate large subsections of the surface and the global adsorption can be determined as a weighted average over the constant $n_{\max}$ subsections. Results for system AB illustrate this point: Figure 4.4, labels A_{AB} and B_{AB} show the predicted and simulated adsorption density on only surface A and B, respectively; AB shows the total on both surfaces.

The Langmuir constants of the four silica surfaces are plotted in Figure 4.5. Surprisingly we find that subtle variations in the arrangement of the surface atoms (see Figure 4.4 (a–d)) can alter the Langmuir

constant by three orders of magnitude. To determine the microscopic cause for such an effect, we have computed local maps of the atomic scale roughness and the surface charge density for each surface and compared the resulting 2D plots with the 2D plot of the PMF's local minima, see Figure C.2 in Appendix C. Whereas some correlation between the surface topography and the PMF maps is apparent (see the right-most column in Figure C.2), there is no consistent dependence, as indicated by the plot of the Langmuir constant versus the root mean squared (RMS) roughness of the surfaces, Figure C.3. Similarly, neither the local pattern of the surface charges correlate with the PMF maps nor does the global surface charge with the Langmuir constant, see Figure C.4.

Nevertheless, Figure 4.5 (a) shows a strong anticorrelation between the Langmuir constant and the RMS surface charge, suggesting a hydrophobic effect in the mechanism of DMMP attraction to silica. Indeed, it was previously shown that an amorphous silica surface becomes more hydrophobic as the number of dangling atoms (responsible for the high RMS charge density) is reduced [49]. The annealing procedure used to create the silica surfaces has exactly that effect. Inspection of the DMMP conformation in the bound state confirms this assertion: on average, the P–O bond of DMMP was found to point away from the surface, exposing the oxygen to the solution. As shown in Figure 4.5 b, surfaces that exhibit stronger adsorption of DMMP also produce a stronger orientational order. As the phantom surface, a neutral barrier with no atoms, has a smaller Langmuir constant than any of the silica surfaces, the adsorption of DMMP to silica is not primarily driven to minimize water-DMMP contacts, but rather to exclude water from hydrophobic patches of silica. Here, the local properties of the solution clearly play an important role, as they are known to depend on the atomic-scale features of the surface [36, 101].

In this communication, we have described and validated a computational method for predicting the Langmuir adsorption isotherm of realistic heterogeneous surfaces. The method permits macroscopically observable properties to be directly related to the atomic structure of the solute, solvent and the substrate and can be applied to study adsorption of any small, weakly interacting solutes and broad range of surfaces, including metals, oxides, polymers and functionalized and patterned substrates, provided the solute-substrate interactions are appropriately described [73, 102]. The exquisite sensitivity of the method to the atomic-scale features of the systems will find practical application in rational design of surfaces to minimize non-specific adsorption, maximize selective binding of desired solutes, and determine fundamental design rules that govern adsorption at the nanoscale.

Chapter 5

Atoms-to-microns model for small solutes transport through sticky nanochannels

*Reproduced in part from Carr R, Comer JR, Ginsberg MD and Aksimentiev A (*in preparation*) Atoms-to-microns model for small solutes transport through sticky nanochannels.*

Lab-on-a-chip technologies exploit the transport of solutions through micro- and nanometer sized structures to operate more efficiently and open a whole new range of applications and sensitivity [18, 6]. The advance of micro- and nanofluidic technologies has enabled new devices for applications like epigenetic analysis [62, 63], protein crystallography [16] and the direct, quantitative study of interfacial phenomena like adsorption [17]. However, in these devices, the ratio of area relative to volume of solution is magnified, exposing the device to new bottlenecks and failure mechanisms [18]. To overcome these obstacles and take advantage of the opportunities the large surface areas present, it will be necessary to have accurate models to properly optimize device design. [33]

While the physics of micro- and nanofluidic devices is well understood [30, 31, 32], there is no one theoretical model which can describe all parts of the device efficiently [33]. The variety of time- and length-scales of the pertinent physical phenomena call for specialized techniques to model different parts of these devices [33]. For example, continuum models work well for modeling the pressure-driven or electroosmotic fluid flow through micro- and nanofluidic devices [31, 32, 34], but break down in the regions of fluid near surfaces [32] or macromolecules [35], where the atomic-scale characteristics of the solvent, solutes and surfaces become important, which can be on the order of nanometers [29, 36]. When the interactions within these regions become important to device function or behavior, such as when adsorption of solutes [37] can lead to clogging of the device [18], discrete methods like classical molecular dynamics (MD) become necessary.

MD has the advantage that it can explicitly calculate inter-particle interactions with all-atom precision, and has been used extensively to simulate biological molecules [43, 44, 45, 46, 47]. Recent advancements in biomolecular-compatible inorganic force fields [48, 49, 50, 51, 52, 53] have made it possible to computationally model the interactions of biomolecules with inorganic substrates with all-atom detail [48, 54, 51, 55, 29, 53]. However, the accuracy of MD comes at a high computational cost that makes it impractical to simulate more than small segments of micro- or nanofluidic devices. To overcome these difficulties, it is common to

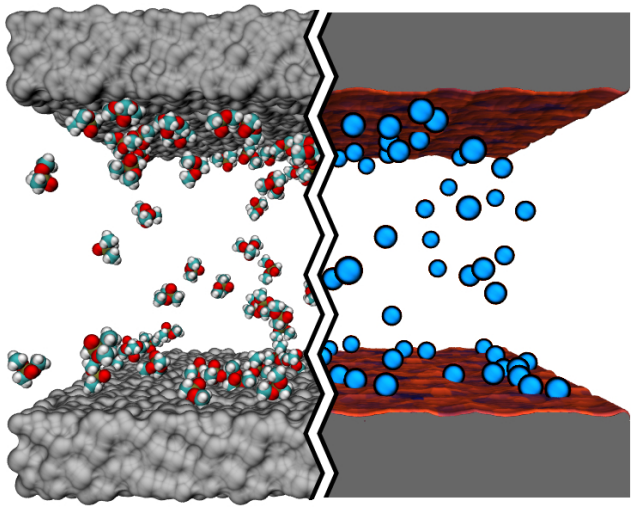

Figure 5.1: Atom-resolution models of small solute transport through a nanochannel. The left hand side of the image illustrates a conventional all-atom MD model: the silica walls of the nanochannel are shown as grey molecular surfaces, the solutes (DMMP) are shown in space-filling representation (C teal, O red, P tan and H white); water is not shown. The right hand side of the image illustrates our atomic-resolution BD model that describes the walls of the nanochannel by means of a three-dimensional potential of mean force (3-D PMF) computed at atomic resolution. The silica walls of the nanochannel are shown as molecular surfaces colored according to the local values of the 3D-PMF (see also Figure 5.2). The solutes are shown as blue spheres.

use particle-based methods like Brownian dynamics [103] to simulate transport in micro- and nanofluidic devices [104], which can be run at a fraction of the cost as MD, but with the loss of atomic-scale precision.

In this manuscript, we present a multi-scale method for computationally modeling the transport of solutes through micro- and nanofluidic devices with atomic-scale precision. Our method employs Brownian dynamics simulations parameterized through all-atom molecular dynamics simulations, similar to work done by Im and Roux in ion channel studies [105]. We show that our model is capable of recreating all-atom MD simulations of solute transport through nanochannels and extend the model to describe experimentally-relevant nanofluidic device components. To demonstrate the capabilities of this method, we have performed exemplary simulations modeling solute transport through a nanochannel measuring 500 nm $\times$ 10 nm, and show that both atomic detail and solute–solute interactions are necessary to properly describe the observed dynamics. The accuracy and efficiency of the model presented here will allow for both the design and optimization of micro- and nanofluidic devices for solute-specific transport, and should complement existing methods.

In this section, we describe our atomic-resolution BD method for modeling transport of small solutes through sticky nanochannels and validate the method through comparison with the results of conventional all-atom MD simulations. Following that, we demonstrate the potential of our method by performing a

sub-millisecond simulation in which a half-micron-long sticky nanochannel is filled with solutes and later drained of solutes and show that the atomic-scale features of a nanochannel's surface can have a dramatic effect on its filling and draining kinetics. In all simulations, we use dimethyl methylphosphonate (DMMP) as a model solute.

The transport of small solute through a micro/nanofluidic system combines diffusion of the solute in the solvent, drift of the solute with the flow of the solvent and adsorption/desorption of the solute to/from the walls of the system. In our atomic resolution BD method, we describe the above transport modalities with atomic-scale precision by extracting the essential parameters for the model from all-atom molecular dynamics (MD) simulations. By eliminating the need to explicitly simulate the solvent and the nanochannel material, our method permits simulations of transport with atomic-scale resolution at a fraction of computational cost of all-atom MD, simultaneously expanding the spatial and temporal range of atomic-scale simulations from tens of nanometers and single-digit microseconds to microns and milliseconds. In our BD method, trajectories of individual solute particles are found by applying the following update rule: [106]

$$\begin{aligned} \mathbf{r}_i(t+\Delta t) &= \mathbf{r}_i(t) + \mathbf{v}_{\text{flow}}\left(\mathbf{r_i}\right)\,\Delta t + \frac{D}{k_{\text{B}}T}\mathbf{F}\left(\mathbf{r}_i(t)\right)\,\Delta t \\ &\quad + (2D\Delta t)^{1/2}\mathbf{R}(t). \end{aligned} \tag{5.1}$$

Here, $\mathbf{r}_i(t)$ is the position of solute i at time t, Δt is the integration timestep, D is the diffusion coefficient, $\mathbf{v}_{\text{flow}}(\mathbf{r_i})$ is the the local velocity of the solvent, $\mathbf{F}$ is the force on molecule i and $\mathbf{R}$ is a vector of independent normal deviates with a mean of zero and a standard deviation of one. The last term in Eq. 5.1 produces random displacements of the solute, mimicking the stochastic force of the solvent.

To capture atomic-scale information in our model, the diffusion coefficient D and force $\mathbf{F}$ are derived from all-atom MD simulations. The diffusion coefficient D can be calculated directly from MD simulations, as we have done previously for DMMP in water [37]. Here, we use the same diffusion coefficient everywhere in the system, but it is also possible to implement a position-dependent diffusion coefficient [107, 108] to better describe diffusion in close proximity to the walls of the channel.

For several simple geometries, the flow velocity in a nanochannel $\mathbf{v}_{\text{flow}}(\mathbf{r})$ can be obtained analytically [109]. For more complicated geometries, the flow profile can be computed numerically using a variety of methods [33, 110]. It is also possible to obtain the flow velocity directly from all-atom MD simulations [29]. Thus, using the all-atom MD method, we have previously shown that pressure-driven flow of water through a silica nanochannel is accurately described by the Poiseuille formular [29]. Hence, we use the following

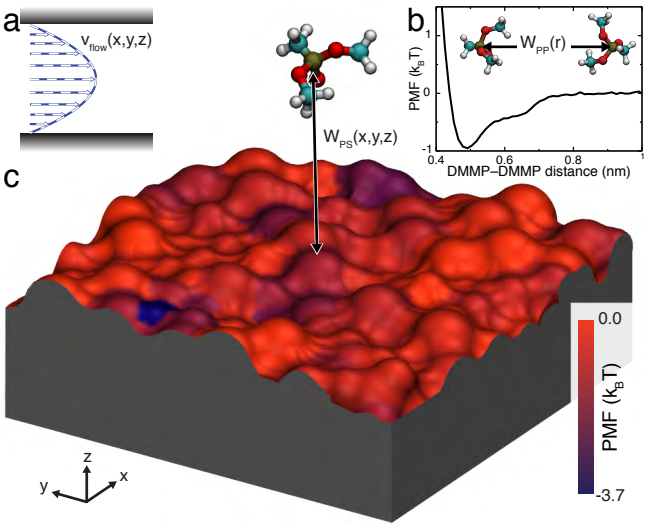

Figure 5.2: Elements of our BD approach to modeling solute transport through sticky channels. a Representative profile of a pressure-driven flow through a nanochannel. b 1D-PMF between two DMMP solutes in water. c 3D-PMF of a DMMP solute in proximity to a silica surface. The silica slab is shown as a molecular surface colored by the local minimum value of the PMF in the direction normal to the slab. Both 1D and 3D PMFs result from from all-atom MD simulations.

analytic expression for $\mathbf{v}_{\text{flow}}(\mathbf{r})$:

$$\mathbf{v}_{\text{flow}}(\mathbf{r}) = \frac{\Delta \mathbf{p}}{8\eta L}\left(h^2 - 4\left(\mathbf{r}\cdot\hat{\mathbf{z}}\right)^2\right), \tag{5.2}$$

where η is the viscosity, $\Delta\mathbf{p}/L$ is the pressure gradient, h is the nanochannel height, $\hat{\mathbf{z}}$ is the unit vector in the direction of the surface, and the coordinate system is defined so that $\mathbf{r}\cdot\hat{\mathbf{z}} = 0$ at the center of the nanochannel. The velocity profile of such flow is schematically shown in Figure 5.2 a. Note that we consider a pressure-driven flow for the sake of example and other flow patterns, such as plug flow [34], can be easily incorporated into our model.

In our approach, the force on a solute $\mathbf{F}$ has two sources: the interaction with other solutes $\mathrm{W_{PP}}$; and the interaction with the channel's surfaces $\mathrm{W_{PS}}$. Thus,

$$\mathbf{F}\left(\mathbf{r}_i(t)\right) = -\partial_r \mathrm{W_{PS}}\left(\mathbf{r_i}\right) - \sum_{j=1,\, j\neq i}^{N} \partial_r \mathrm{W_{PP}}\left(|\mathbf{r_i} - \mathbf{r_j}|\right), \tag{5.3}$$

where $\mathrm{W_{PP}}$ and $\mathrm{W_{PS}}$ are solute-solute and solute-surface potentials of mean force (PMFs). The PMF between a solute and a surface (or a second solute) represents the change in free energy upon bringing the solute from a distant point to a particular position with respect to the surface (or the second solute), and includes all electrostatics, van der Waals, entropic and solvation effects.

Figure 5.2b shows the PMF of the DMMP–DMMP interaction, computed from all-atom MD simulations

using the umbrella-sampling [99] and weighted histogram analysis [100] methods. Details of all PMF calculations are given in Appendix D. W_{PP} has a shallow (< 1 k_BT) short-range attractive well and a steep excluded volume repulsive part at short distances. The depth of the minima is in agreement with the results of our MD simulations where no aggregation of DMMP was observed [37].

Figure 5.2c illustrates the 3D-PMF of DMMP in proximity to a representative patch of a silica surface. The silica surface is colored by the local minimum value of the PMF for each (x,y) point, revealing the heterogeneous nature of the solute–surface interaction. The 3D solute–surface PMF was computed from all-atom MD simulations using a generalization of umbrella-sampling and weighted histogram analysis methods. The details of the calculations are described in Appendix D and in Carr et al. [37]

Note that in our all-atom calculations of both W_{PP} and W_{PS}, the rotational degrees of freedom of the solute are averaged out as the time scale of the solute rotation is much smaller than the length of a typical MD simulation in one of the umbrella-sampling windows. Solute for which such calculations are possible are considered here as "small". In the form presented here, our atomic-resolution BD method is applicable only to those chemical compounds for which such calculations are possible.

We validate our BD method through comparison with the results of conventional all-atom MD simulations. Due to the time and length scale limitations of the latter method, the validation simulations were performed using relatively small nanochannel systems of $10 \times 10 \times 5.5$ nm^3.

Each all-atom system contained an infinite-slit silica nanochannel filled with aqueous solution of DMMP, shown in the left part of Figure 5.1. Each surface of the nanochannel was built by tiling 16 identical slabs of amorphous silica 2.5×2.5 nm^2 in area into a square. Figure 5.3a-d shows the four different silica tiles that we used to build nanochannels A, B, C, and D. Each tile has different arrangement of surface atoms, giving each surface a different overall affinity to DMMP [37]. The nanochannels were created by placing two silica slabs 5.5-nm (surface to surface) apart and filling the gap with pre-equilibrated solution of DMMP. Under periodic boundary conditions, the nanochannels were effectively infinite in two dimensions. Flow of the DMMP solution was induced in the channel by imposing a pressure gradient across the system [29]; the velocity of the flow was found to have a negligible effect on DMMP adsorption to the surface of the channel [37]. A complete description of the protocols used to build and simulate our all-atom models is available in Appendix D.

Figure 5.3e plots the average density of DMMP molecules adsorbed to the walls of the nanochannels as a function of time for each of the four MD simulations of the nanochannels. In less than 15 ns, each system reaches a steady state. Note that although all surfaces are made from the same material (silica), different arrangement of the surface atoms leads to different amounts of DMMP adsorbed in the steady state [37].

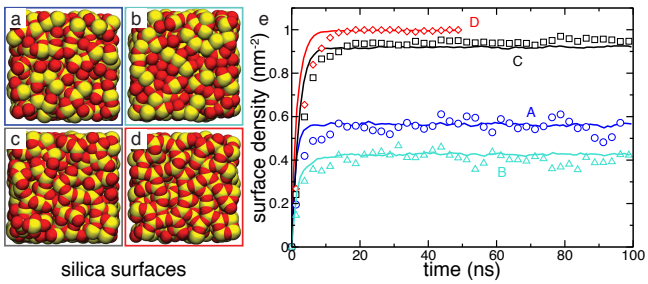

Figure 5.3: Surface adsorption of DMMP solute simulated using our BD and all-atom MD models of the same nanochannels. a–d All-atom models of four silica surfaces (A–D) used in our simulations of DMMP adsorption. Oxygen and silicon atoms are shown as red and yellow vdW spheres, respectively. e Surface density of DMMP adsorbed at the walls of four nanochannels versus simulations time. The BD data (solid lines) were averaged over 25 unique trajectories that began having the same coordinates of DMMP as the corresponding MD simulation (symbols).

To use the results of the above simulations as a test of our BD method, a BD model of each all-atom nanochannel system was build by replacing each DMMP molecule by a BD particle and each nanochannel surface by the corresponding 3D-PMF potential. To make an unambiguous comparison possible, each BD system had exactly the same dimensions as the corresponding MD system and the same initial coordinates of the DMMP particles were used.

The average density of adsorbed DMMP particles observed in 25 BD simulations (using different seeds for the random number generator) of each of the four nanochannels is plotted versus time in Figure 5.3e. The plot indicates excellent quantitative agreement between BD and MD methods in predicting the steady-state surface density of adsorbed DPPM solute and good quantitative agreement in predicting the kinetics of adsorption process.

To determine if the BD model is capable of reproducing the atomic scale features of different silica surfaces, we computed the 2D density maps of adsorbed solutes for all four surfaces considered. Figures 5.4 a and b shows the steady-state adsorption density maps for surface C; the plots for all four surfaces are available in Appendix D. Visual comparison of the maps reveals excellent quantitative agreement between the BD and MD methods. As the spatial resolution of the maps is 0.42×0.42 Å^2, we can say with confidence that our BD method has truly achieved atomic resolution.

Figure 5.4c shows a 2D map of the local PMF minima near surface C, computed for each point on the surface along the line normal to the surface plane. As expected, the pattern of adsorption density, Figures 5.4 a and b, closely matched the pattern of PMF minima, Figure 5.4c.

To test whether our BD method can model a nanochannel that combines surfaces of different adsorption properties, we constructed all-atom and BD models of a nanochannel that combined surfaces A and B, Figure 5.5. The steady-state profile of DMMP concentration across this channel is shown in Figure 5.5 for

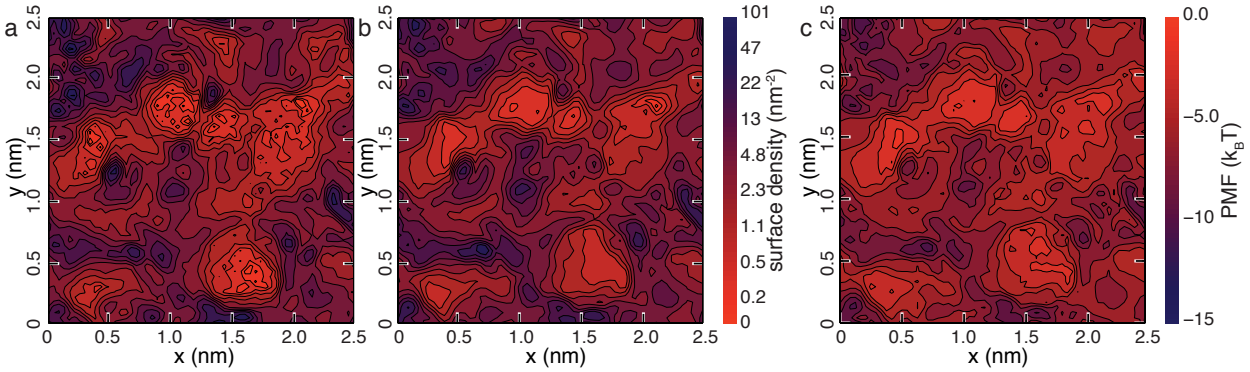

Figure 5.4: Atomic-scale features of DMMP adsorption. a, b Surface density maps of adsorbed DMMP in our MD (panel a) and BD (panel b) simulations of nanochannel C. The maps were computed by averaging over the steady-state parts of the corresponding trajectories and over the identical patches of the corresponding surfaces. The BD simulations quantitatively reproduce the results of the all-atom MD simulation. Note the use of logarithmic scale in coloring the surface density patterns. c Local minima of the solute-particle PMF near the surface of the nanochannel. The pattern of DMMP adsorption in both MD and BD models closely follows the pattern of the PMF minima. Similar plots for nanochannels A, B and D are available in Appendix D, Figure S1.

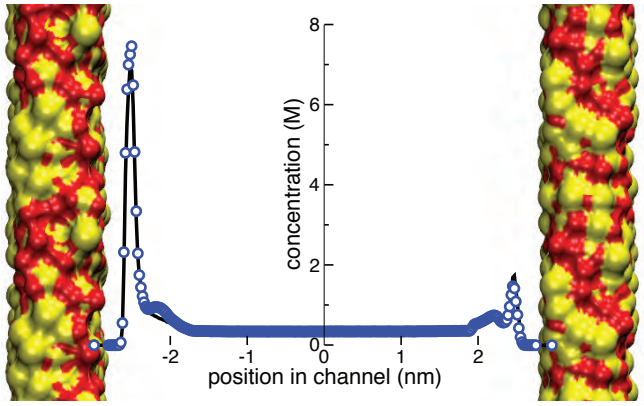

Figure 5.5: MD and BD simulations of a nanochannel that has two different-affinity walls. The two walls, surface A (left) and B (right) are shown as molecular surfaces colored according to the atom type (Si yellow, O red). DMMP has different affinity to these surfaces [37], which results in an asymmetric distribution of the DMMP in the channel. The plot shows the steady-state concentration profile of DMMP across the nanochannel (normal to the surfaces) obtained from MD (black line) and BD (blue circles) simulations. The data for the BD simulations represent the average of 25 independent trajectories.

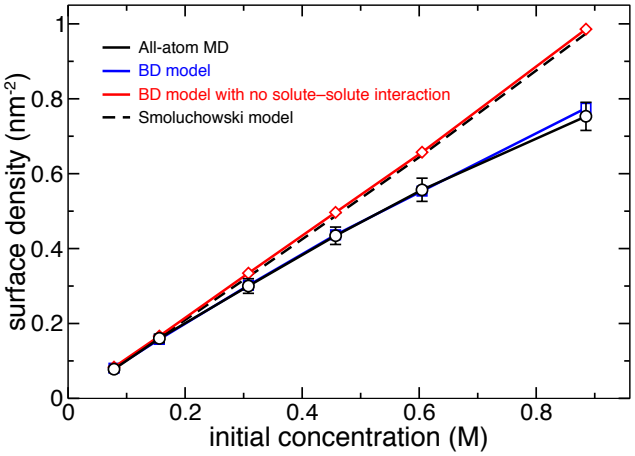

Figure 5.6: Density of adsorbed DMMP molecules versus its initial concentration in nanochannel A predicted using different simulation methods. Including the solute-solute interaction (Figure 5.2 b) is essential for proper description of the adsorption isotherm using the BD model at high bulk concentrations. Each BD data point represents the average of 25 independent trajectories; the error bars for the BD data are smaller than the symbols. The 1-D Smoluchowski model was based on the atomically precise 3D-PMF. Detailed description of the Smoluchowski model is provided in Appendix D.

both MD and BD models. Both models produced essentially identical results, showing preferential adsorption of DMMP to a higher affinity surface.

Figure 5.6 plots the dependence of the steady-state DMMP surface density on the initial concentration of DMMP particles in nanochannel A predicted using both the all-atom MD and atomic-resolution BD models. Again, we find the predictions of both models to be in quantitative agreement with each other. In general, the simulated adsorption isotherm of DMMP on silica was found to be in agreement with the Langmuir model of adsorption [37]. We note, however, that in the absence of the solute-solute interaction potential W_{PS}, the BD model predicts a linear dependence between the average surface density of adsorbed solute and the bulk concentration of DMMP, which overestimates the amount of adsorbed DMMP at high concentrations.

Finally, we compare our BD method with the following two alternative approaches: numerical solution of the Smoluchowski equation [111] and implicit solvent simulations [112]. The test of the Smoluchowski approach was performed using a one-dimensional projection of the 3D-PMF obtained by averaging the latter. The dependence of the steady-state adsorption density on the bulk concentration of DMMP is shown in Figure 5.6. The results of the Smoluchowski model quantitatively match the results of the BD and MD simulations at low solute concentrations, but deviate at higher concentrations as the Smoluchowski model neglects solute-solute interactions. We have also simulated adsorption of DMMP on silica using all-atom implicit-solvent MD. If compared to explicit-solvent MD, the use of implicit solvent did not cause a dramatic

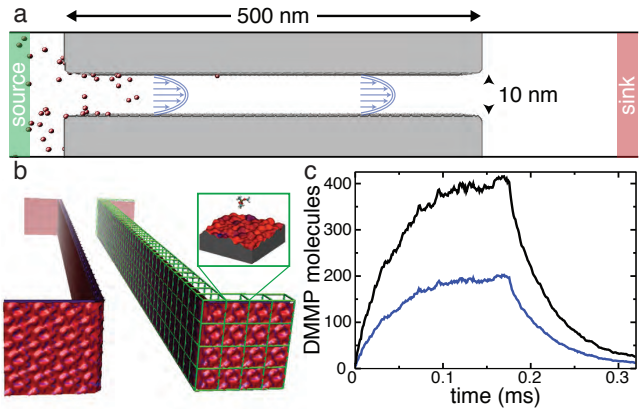

Figure 5.7: Atomic-resolution BD simulation of filling and draining of a sticky 0.5 μm-long silica channel. a Diagram illustrating the setup of a BD simulation. The walls of the channel are shown in gray, the solute particles are shown in red. Green and red regions indicate the source and sink reservoirs where the concentration of solute is maintained constant. The channel is not drawn to scale. b 3D-PMF representation of the surface of the nanochannel, obtained by combining atomically precise 3D-PMF maps of the representative patches of the surface (one is shown in Figure 5.2c). c Sub-millisecond simulation of filling the nanochannel with solutes and its subsequent draining (see text for details). The total number of DMMP solutes in the nanochannel (black) and number of DMMP adsorbed to the nanochannel's walls (blue) are plotted versus time.

improvement in the computational efficiency of the simulations. Furthermore, our implicit solvent model of DMMP transport through nanochannel systems failed to reproduce the results of our all-atom MD. A complete discussion of the implementation and results of the Smoluchowski and implicit-solvent MD models is provided in Appendix D.

To demonstrate the ability of our method to bridge the ångström and micron scales, we have constructed computational models of silica nanochannels 100- and 500-nm in length and simulated filling of the nanochannels with DMMP solutes and subsequent draining of them.

Figure 5.7 a illustrates a typical setup of these simulations. The particular channel shown is 500 nm in length, 10 nm in width and is effectively infinite in the plane normal to the figure due to the use of periodic boundary conditions. In our simulations of filling and draining, the total number of particles in the system can change as the simulation progresses. Two buffer regions away from the channel's inlets (labeled source and drain) maintain the prescribed concentrations by an algorithm that periodically adds or removes particles. The target number of particles at each instance the algorithm is active is randomly selected from the Poisson distribution with the mean set at the prescribed average number. Doing so not only maintains the prescribed average concentration in the buffer region but also introduces fluctuations in the buffer concentration consistent with the statistical mechanics of noninteracting particles in a uniform region. Systems that included constant concentration buffers were not periodic in the direction of the flow.

To build models of devices of microscopic size, we create complex structures by mixing and matching

3D PMFs for the particle–surface interactions, in analogy to laying bricks to create a wall. These grids of 3D PMFs provide the layout of the model nanofluidic device, which is completed with periodic boundary conditions that define the simulation box. The surface of the nanochannel was created by tiling 3D PMF maps of the solute–surface interaction, as detailed in Figure 5.7 b. Each 3D PMF tile had an area of 2.5×2.5 nm^2, resulting in a total of 1600 tiles on the interior of the nanochannel.

DMMP molecules were generated on one side of the nanochannel with a particle reservoir that maintained a constant concentration of 10 mM, shown in green in Figure 5.7. The particles entered the nanochannel through a mix of diffusion and solvent flow, which was modeled implicitly as a Poiseuille flow (Eqn 5.2) with a peak velocity of $v_0 = 0.005$ nm/ns in the center of the channel. Outside the channel, the solvent had a uniform velocity of $2/9v_0$ consistent with a constant mass current of solvent through the system. As DMMP molecules exited the nanochannel on the opposite side, they were absorbed by a second reservoir that maintained a zero-concentration region, shown in red.

Figure 5.7 c shows the dynamics of the 500-nm nanochannel simulation. Initially, the source reservoir was set to 10 mM, introducing DMMP into the channel. After 0.176 ms, the source was changed to a sink, so that the draining of DMMP from the channel could be observed. The simulation began with no particles in the nanochannel, and as the particle reservoir on the left created DMMP molecules, they diffused and flowed into the nanochannel. Inside the nanochannel, DMMP molecules adsorbed to the surface as they were transported through. The number of molecules in the nanochannel or adsorbed to the device surface during the simulation is shown in Figure 5.7 c, as black or blue lines, respectively. As the simulation progressed, more and more molecules adsorbed to the surface, until after about 0.12 ms the rate of adsorption became equal to the rate of desorption, and the number of molecules on the surface and in the channel reached a steady state. At this point, the reservoir on the left became a sink like the reservoir on the right, and the channel slowly drained, with the entire simulation spanning a time > 0.3 ms.

To study the effect of the solute–surface interaction on solute transport, we created four more model nanochannels, each with a different DMMP–silica 3D PMF map as the base. The silica surfaces used to create these 3D PMF maps are shown in Figure 5.3 a–d. Each simulation system was built the with the same dimensions as the 500-nm nanochannel simulation system, but with a nanochannel of length 100 nm. The simulation protocol was the same as before: DMMP molecules were added from a particle-reservoir set to 10 mM until a steady-state in the nanochannel was reached. The particle reservoir was turned off, and the DMMP slowly drained from the nanochannel.

Figure 5.8 detail the results of these simulations. Figure 5.8 a and b show the number of solute molecules adsorbed to the each nanochannel surface as a function of time during the filling (a) and draining (b) of the

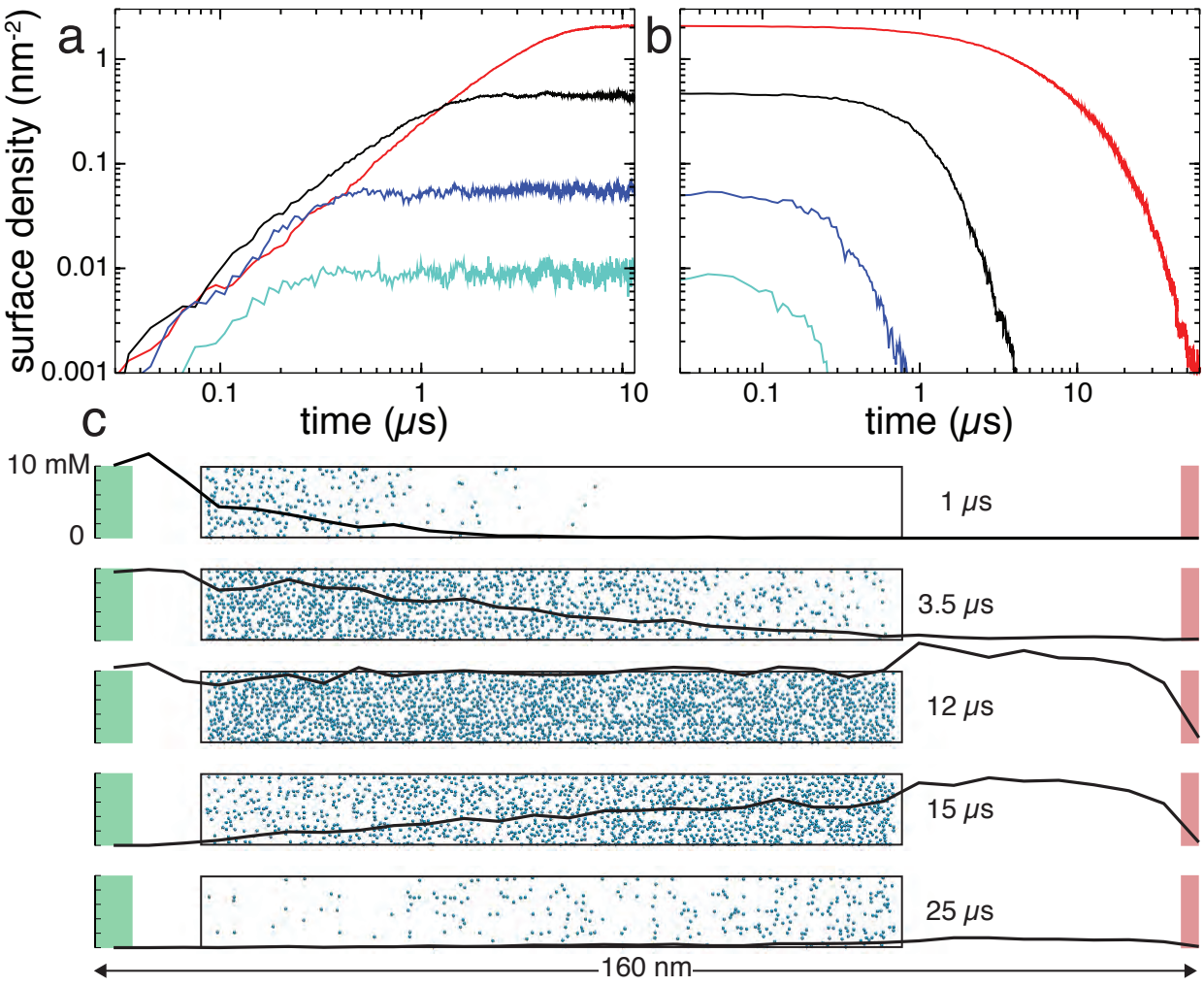

Figure 5.8: The effect of atomic-scale features on transport of small solutes through sticky sub-micrometer nanochannels. a,b The number of adsorbed DMMP molecules during filling (a) and draining (b) of the four same-size silica nanochannels having different atomic-scale features of their surfaces (shown in Figure 5.3 a–d). c The filling and draining of nanochannel D. Each of the five snapshots characterizes the state of the system at a different instance of the BD simulation. The nanochannel is shown as a transparent box with adsorbed molecules in blue. The black line shows the profile of DMMP concentration through the system, from the particle source (shown in green) to the sink in red, not including solute bound to the nanochannel surface.

nanochannel. The strength of the DMMP–silica interaction can be seen to determine not only the amount of DMMP adsorbed to the surfaces, but also the time it takes to both fill and drain the nanochannel. Figure 5.8 c highlights the simulation of nanochannel D, the nanochannel with the strongest DMMP–silica interaction. The bulk density in the simulation system, averaged over 1 μs, is compared with the amount of adsorbed DMMP molecules on one surface, at 5 different points during the simulation: Near the beginning of the simulation, when the channel is beginning to fill (averaged around 1 μs); at the halfway point to the steady state (3.5μs) ; during the steady state (12μs, not shown in Figures 5.8 e or f); at the halfway point of draining (15μs); and near the end of the simulation, when the channel is almost completely drained (25μs). From these figures, it can be seen that in general, the DMMP molecules flow through the nanochannel with the solution, but the sticky surfaces of the nanochannel cause a significant amount of DMMP to lag behind the bulk flow, as molecules are caught in attractive regions of the surface.

In this manuscript, we have presented a multi-scale computational method for accurately predicting the transport of solutes in situations where the solution–device interface has a significant effect. While no one theoretical model is be able to capture every aspect of transport in micro- and nanofluidic devices, our model should interface nicely with the existing techniques [33]. The multiscale method we have presented satisfies the need for a theoretical method to describe the boundary between bulk solution and the device surfaces, and opens up new possibilities for device design and optimization.

The results of our simulations in which the nanochannel was filled with and drained of solutes show that it is possible to view the nanochannel surfaces as a functional component of a nanofluidic device. For example, consider a situation where a surface can be created to interact strongly with one type of particle but weakly with another. With our model, it would be possible to design and optimize a device for filtering a solution or accurately diluting concentrations to control reaction rates on a computer before fabricating it in the lab. We believe that the accuracy and efficiency of the method presented here will allow for the design and optimization of micro- and nanofluidic devices for solute-specific transport and open up new opportunities for lab-on-a-chip technologies.

Molecular Dynamics simulations All molecular dynamics (MD) simulations were performed using the program NAMD [43], a 1 fs integration time step, particle mesh Ewald (PME) electrostatics [77], and periodic boundary conditions. Simulations in the NPT ensemble (constant number of particles N, pressure P and temperature T) were performed using a Langevin thermostat [113] and Nosé-Hoover Langevin piston pressure control [114] set at 295 K and 1 atm, respectively. The damping coefficient of the Langevin thermostat was 1 ps^{-1} and was applied only to the atoms of the silica surfaces. A smooth (1.0–1.2 nm) cutoff was used to

compute the Lennard-Jones forces. All simulations were performed using the TIP3P water model modified for the CHARMM [44] force field and a CHARMM-compatible model for silica [49]. A complete description of the simulation setup and analysis was reported previously in Carr et al. [37], and is available in Appendix D.

Brownian Dynamics simulations All Brownian dynamics simulations were performed using a custom multithreaded code developed in-house. The integration timestep Δt was 10^{-4} ns. A smooth (0.8–0.9 nm) cutoff was used for evaluation of solute–solute and solute–surface forces, as both forces are indistiguishable from zero at distances greater than the cutoff (see Figure 5.2). The concentration of particles in the constant-concentration reservoirs was checked every 0.05 ns, and particles were added or deleted to give the desired mean concentration and mean fluctuation of the concentration. The diffusion constant D of DMMP was 9.1 nm/ns^2 [37].

Chapter 6

Synthetic ion channels embedded in biological membranes

Reproduced in part from Carr R, Weinstock IA, Sivaprasadarao A, Müller A and Aksimentiev A (2008) Synthetic Ion Channels via Self-Assembly: a Route for Embedding Porous Polyoxometalate Nanocapsules in Lipid Bilayer Membranes Nano Lett. *8:3916–3921 (Copyright © 2008 American Chemical Society). [38]*

Transport of ions across the cell's boundaries is a fundamental process underlying many cellular functions, from the secretion of hormones to the beating of a heart. A lipid bilayer membrane encapsulating a biological cell is virtually impervious to ions. Therefore, a special class of proteins residing in the cell's membranes is required to direct traffic of ions into and out of the cell and cellular organelles [115, 116]. The structures of some ion channel proteins are known in atomic detail [117, 118, 119, 120, 121]. However, to fully understand the physico-chemical processes underlying the function of these remarkable systems, their synthetic analogs with functionality embedded by design have to be synthetized and characterized [122, 123, 124, 125]. In this manuscript we investigate the feasibility of assembling a biological lipid membrane with a particular class of compounds which exhibit the functionality of ion channels. Our molecular dynamics simulations suggest a route for transforming these systems into hybrid bio-inorganic assemblies which can model ion channels in biological settings.

A route to creating novel, synthetic models of ion channels may lie in the chemistry of polyoxomolybdates (POMs). Here we consider a porous POM nanocapsule [5, 126, 127, 128]:

$$[(\text{Pentagon})_{12}(\text{Linker})_{30}]^{72-} \equiv [\{(\text{Mo})\text{Mo}_5\text{O}_{21}(\text{H}_2\text{O})_6\}_{12}\{\text{Mo}_2\text{O}_4(\text{SO}_4)\}_{30}]^{72-} \tag{6.1}$$

made of twelve pentagonal molybdenum oxide regions, each linked to five other regions by binuclear molybdenum oxide-ligand type groups. The connection of the 12 pentagonal units forms 20 circular pores on the surface of the capsule. The structure of the capsule is shown in Figure 6.1 a; the total charge of the capsule is $-72e$, where e is the charge of a proton. The atomic coordinates of the capsule were taken from an earlier publication [129].

The high charge of the porous nanocapsules makes them soluble in water and attractive to cations. Studies

have shown that water and small inorganic cations can enter the capsule cavity through the pores [5, 130, 131]. Moreover, some organic cations, such as guanidinium, can reversibly block the passage of smaller ions through the pores, mimicking ligand-induced gating of biological ion channels [132, 130]. The structure of the groups lining the pore and hence the coordination of the passing ions can be adjusted, which provides a route for customizing the selectivity of the ion transport [5, 130]. Thus, it appears that the porous nanocapsules can serve as models of biological ion channels, whose structure can be engineered at the atomic level. To fully reproduce typical physiological conditions, a porous nanocapsule would, ideally, be placed in a lipid bilayer membrane. An underlying difficulty is, however, that the nonpolar, hydrophobic interior of the latter is not compatible with the high charge of the capsule.

In this manuscript, we detail molecular dynamics (MD) simulations demonstrating a route for embedding POM porous nanocapsules in lipid bilayer membranes via self-assembly. It was previously shown that such porous nanocapsules can be encapsulated with dimethyldioctadecylammonium (DODA) surfactants, amphiphilic cations consisting of a cationic ammonium group attached to two long nonpolar tails [133, 127]. Here, we show that the DODA–capsule interaction can be exploited to create a liposome-like, water soluble structure that can fuse with a lipid bilayer membrane and thereby embed a POM porous nanocapsule in the bilayer.

State of the art, all-atom MD simulations are limited to the timescale of hundreds of nanoseconds, which is considerably less than the timescales of liposome formation or fusion with a lipid bilayer membrane. Recently, a reliable coarse-grained (CG) model of lipid bilayers became available, which greatly extended the timescale and the scope of the MD method [134, 135, 136, 137, 138, 139]. In a CG model, groups of atoms are replaced by representative 'beads' that interact much like atoms in the corresponding all-atom model. Due to the simplification of the potential energy function (the force field), CGMD simulations can employ larger timesteps (20 fs), which, in addition to the reduction of the number of particles, dramatically increases the span of an MD simulation, up to 1,000 times [135].

To model interactions of our porous nanocapsule with a mixture of detergent, lipid and water we extended the Marrink CG model of phospholipids [134]. DODA was coarse-grained using existing bead types available to describe lipids, with the addition of two angle parameters taken from similar lipid configurations. For the CG model of the porous nanocapsule, we created new bead types using parameters derived from the capsule's shape. Strong bond and angle forces were introduced to keep the capsule rigid; the equilibrium values of the bonds and angles were derived from the all-atom structure. Nonbonded forces between the capsule and other beads were taken from the Marrink model. Thus, the beads comprising our porous nanocapsule were either charged, polar or apolar [134]. Figures 6.1 b and c illustrate the all-atom and CG

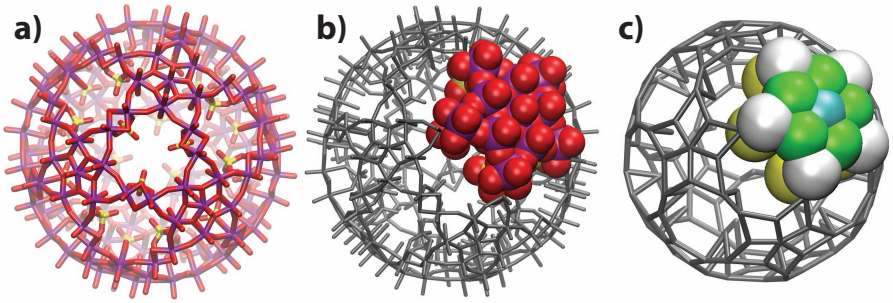

Figure 6.1: Mo_{132} type Keplerate capsule. a) All-atom structure of the capsule, oriented with a pore in the center. Three sulfate groups line each pore, forming a triangle with sides of 5.6 Å [130]. Molybdenum atoms are shown in purple, oxygen in red and sulphur in yellow. b-c) All-atom (b) and CG (c) models of the porous nanocapsule. The capsule considered here is made of 12 repeats of a pentagonal unit. Thus, specifying the mapping of one all-atom pentagonal unit and its linker units to the CG representation is sufficient to describe the mapping of the entire capsule. The colors in the CG representation highlight the four different types of beads used to model the capsule. The detailed description of the CG model is provided in Appendix E.

models of the porous nanocapsule (1), respectively. When six copies of the porous nanocapsule were placed in a 120 Å×120 Å×120 Åbox filled a 0.25 M solution of NaCl and simulated for 0.4 μs, no aggregation of the capsules was observed. Complete details of our CG model and simulation protocols for the CGMD simulations in Appendix E.

To test our parameters for the porous nanocapsule and DODA detergent, we simulated self-assembly of DODA with the nanocapsule in octane, a simple nonpolar solvent. Our simulations confirmed that DODA molecules, starting from a random distribution, would aggregate to form a steady-state hydrophobic spheroid. In accord to previous modeling work [133] on a porous CH_3COO-linker nanocapsule (the total charge of which is $-42e$), the concentration of DODA was observed to decrease with the radial distance from the capsule's surface. In our case, the total charge of the capsule–DODA spheroid varied from -2 to $-10e$ in the steady state. These simulations are discussion in more detail in Appendix E.

Once we were satisfied with our description of the system, we investigated the feasibility of obtaining a water-soluble, liposome-like structure encapsulating our porous nanocapsule by spontaneous self-assembly. Several systems were prepared, each containing a porous nanocapsule, DODA detergent, palmitoyloleoylphosphatidylcholine (POPC) lipid, water and enough ions to neutralize the system. The DODA to POPC ratio was held constant at 1:2.2; several concentrations of DODA/POPC were tested. In the starting conformation, DODA, POPC, water and ions were randomly distributed around the capsule, as would result from sonication in experiment. A summary of all runs performed is given in the manuscript's Supporting Information [38].

Our simulations revealed that a DODA/POPC mixture can spontaneously form a liposome-like structure

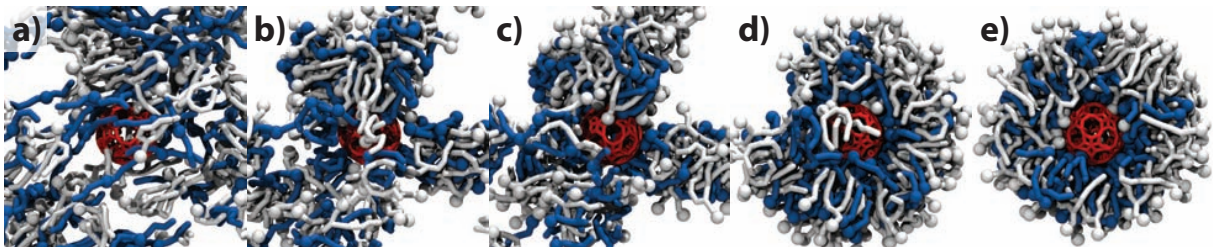

Figure 6.2: Self-assembly of a capsule liposome. The snapshots illustrate the molecular configuration obtained after 0 (a) 3.36 (b) 7.36 (c) 41.68 (d) 100.24 (e) ns of CGMD simulation. The porous nanocapsule is shown in red, DODA in blue, POPC in white, water and ions are not shown. An animation illustrating this simulation is available in the manuscript's Supporting Information [38].

around the porous nanocapsule. Figure 6.2 illustrates a typical self-assembly trajectory. In the capsule-liposome assembly, DODA forms a shell surrounding the capsule with its ammonium groups facing the capsule's surface. The charge of this inner layer is about $68 \pm 3e$. DODA's hydrophobic tails intermix with the hydrophobic tails of POPC, while the polar headgroups of POPC face the water, forming the outer layer of the liposomal structure. The presence of DODA molecules in the outer shell of the liposome renders the overall charge of the capsule liposome at about $+50e$. The structural details, as well as the kinetics of self-assembly at different conditions, are provided in Figure 6.3.

As detailed the manuscript's Supporting Information [38], some simulations did not result in a liposome-like assembly. Successful assembly was observed for the range of DODA concentration between 0.060 to 0.076 M. For lower DODA concentrations, there was not enough DODA/POPC molecules to completely cover the porous nanocapsule. For higher DODA concentrations, an interconnected network of POPC and DODA was formed instead of discrete liposomes. Furthermore, increasing ion concentrations to 0.25 M was enough to arrest the growth of the liposomal aggregate, because of the competition between the ammonium groups of DODA and the Na^+ ions for binding the porous nanocapsule. Figure S4 in the manuscript's Supporting Information [38] shows an example of such an outcome, where Na^+ ions surround the capsule, preventing DODA from approaching the capsule's surface.

Next, we tested whether a capsule liposome could deliver our porous nanocapsule into a lipid bilayer membrane. Fusion of two liposomes was previously studied using all-atom [140] and coarse-grained systems [141, 142, 143]. Note that even using a CG model, spontaneous fusion is too slow of a process to be observed in an MD simulation starting from a random conformation [143]. To make the observation of liposome fusion possible within the time scale of an MD simulation, several methods have been used, for example, restraining the two liposomes in close proximity to one another through either external force [141] or by introducing a linker molecules [143], applying external forces to move the liposomes into contact [142] or

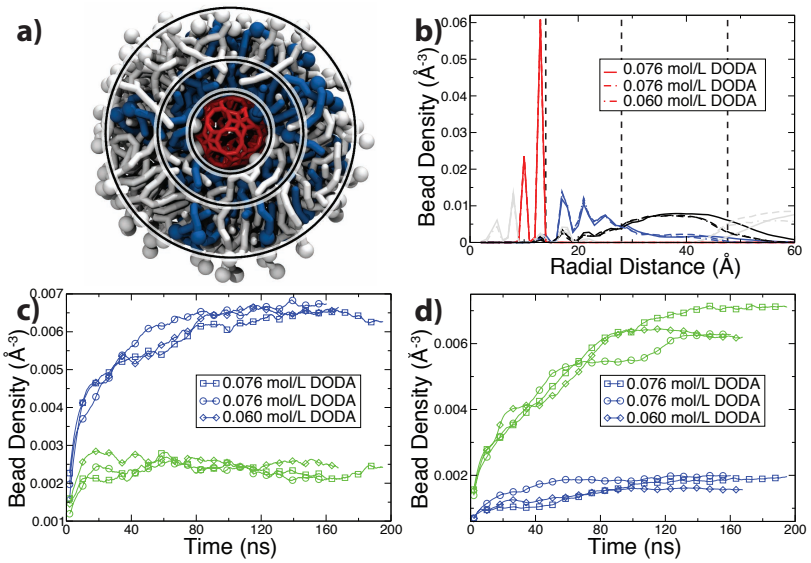

Figure 6.3: Structure and kinetics of capsule-liposome assembly. (a) Structure of the capsule liposome. The porous nanocapsule (red) is surrounded by a shell of DODA (blue) and a secondary shell of POPC (white). The three rings separate the capsule from DODA (inner), DODA from POPC (middle) and POPC from water (outer) according to the density plots, panel b. (b) Density of the porous nanocapsule (red), DODA (blue), POPC (black) and water (grey) versus radial distance from the center of the capsule. Dashed lines correspond to the location of the rings in panel a. Results of three independent runs are shown. (c,d) Density of DODA (blue) and POPC (green) beads versus time in three simulations. The densities were computed by averaging over the volume between the inner and middle (c) and middle and outer (d) rings.

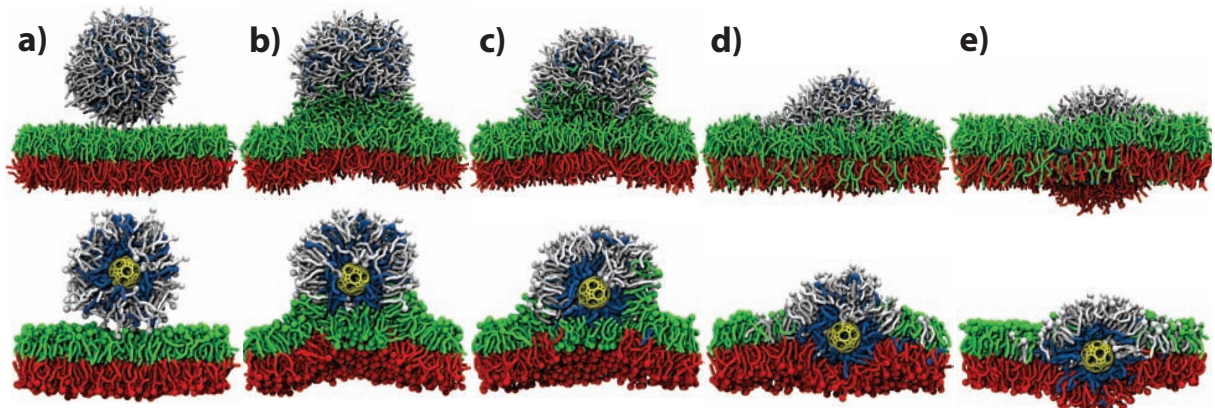

Figure 6.4: Fusion of a liposome with a lipid bilayer. Snapshots illustrate the state of the CGMD simulation after 0 (a), 125.2 (b), 431.6 (c), 607.36 (d) and 940.4 (e) ns. The porous nanocapsule is shown in yellow, DODA in blue, POPC in white, the top and bottom leaflets of the POPC bilayer in green and red, respectively. For each panel, the image in the bottom row is a cut-away view of the same configuration as shown in the top row. An animation illustrating this simulation is available in the manuscript's Supporting Information [38].

manually removing water between adjacent liposome headgroups [140].

We performed CGMD simulations starting from a model of a fully formed capsule liposome and a patch of pre-equilibrated POPC bilayer membrane solvated in 0.25 M aqueous solution of NaCl. Figure 6.4a shows one initial configuration. To induce liposome fusion, we tried four different methods. In our first method, we accelerated the approach of the liposome to the lipid membrane by pulling the center-of-mass of the capsule with a constant velocity towards the membrane using the standard protocol of Steered Molecular Dynamics (SMD) [144]. When the distance between the center of the capsule and the center of the membrane approached 60 Å (Figure 6.4 b), the SMD force was turned off. Alternatively, we placed the liposome a certain distance away from the surface of the membrane and let the system evolve freely. This method was successful for a closest-approach distance of 7 Å between the phosphate groups of the liposome and the bilayer. Both SMD and free equilibration methods led to essentially the same conformation (Figure 6.4 b), as a fusion stalk quickly formed, connecting the liposome to the bilayer. At distances greater than 12 Å, the liposome did not fuse with a lipid bilayer within the time scale of our simulation, even when a half of the lipid headgroups were replaced with negatively charged moieties or when a voltage bias was imposed across the system.

Once fusion was initiated, our systems were allowed to evolve under constant pressure. During this period of equilibration, lipid and detergent from the capsule liposome mixed with the lipids from the upper leaflet of the membrane. This process slowed the fusion and the bilayer became bowed because of the imbalance of the number of lipids in the leaflets of the bilayer. This effect is an artifact of the periodic boundary

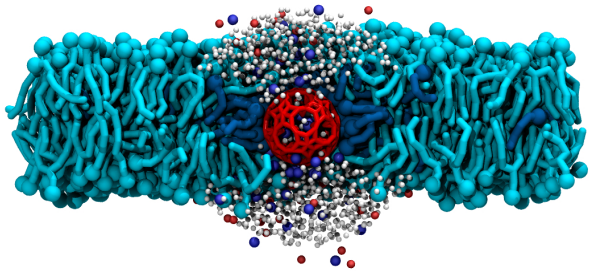

Figure 6.5: Porous nanocapsule as an ion channel. The snapshot illustrates the outcome of a CGMD simulation of a porous nanocapsule (red) held in a POPC bilayer membrane (cyan) by DODA (blue). The top of the capsule is open to water (white) and ions (blue Na^+, red Cl^-). Note the ions inside and around the capsule.

conditions used in our simulations, which do not permit the lipid bilayer to form a curved membrane with the radius of curvature greater than half the system size. A larger patch of a lipid bilayer is expected to flatten out, distributing the lipids from the liposome over a large area and thereby effectively equalizing the density of lipids in both leaflets.

To eliminate the effect of the periodic boundary conditions in our simulations of the liposome–bilayer fusion, we used the following method to equalize the number of lipids in the leaflets. The coordinates of randomly selected lipids from the top leaflet at the periphery of the system were reflected with respect to the plane passing through center of the bilayer, which effectively inserted them into the bottom leaflet. Following a short period of relaxation where all beads of the capsule, DODA and POPC, except for those moved to the bottom leaflet, were harmonically constrained, the system was equilibrated until the area of the bilayer became steady. This procedure was then repeated until the number of lipids in the leaflets became equal. This allowed the membrane to flatten out and expand, leaving the capsule in the middle of the bilayer, surrounded by DODA and POPC, Figure 6.4 e. An animation illustrating the fusion process is available in the manuscript's Supporting Information [38]

At the end of the fusion simulations, the capsule remained trapped inside the bilayer, not directly connected to the solvent. To test whether the capsule would be stable in a configuration open to water on either side of the membrane, we created a model of such a system by removing POPC and DODA above and below the capsule and filled the empty space with water and ions. Following a brief period where the capsule, DODA and POPC were constrained while the water and ions were allowed to assume a new equilibrium conformation, the system was simulated free of restraints under constant pressure conditions. Figure 6.5 illustrates one system obtained at the end of a 351-ns simulation. In the equilibrium configuration, water was observed to flow into and out of the capsule as Na^+ cations entered, showing that the capsule can be

both stable in this conformation and transport ions across the membrane, even though the capsule's charge is reduced by the presence of the cationic DODA. An animation illustrating this simulation is available in the manuscript's Supporting Information [38]. Inside the capsule, water beads were seen to form highly ordered configurations. From time to time, they were observed to rearrange themselves in quick cascades resulting in a net flow of water. From these simulations, we estimated the osmotic permeability to water of the porous nanocapsule at 3.5×10^{-15} cm^3/s, which is roughly three orders of magnitude less than that of the α-hemolysin channel [83]. This estimate should be taken with caution, as it is not known how accurate the CGMD method is for simulating ion and water conductance through narrow pores. Furthermore, based on the present isolated capsule (1) it has been proven that an equilibrium between Li+ cation uptake and release exists, and that encapsulated Li^+ cations can be exchanged by Na^+ [145, 146, 131, 130, 147, 148]. This means there is the option to study counterion transport systematically [130]. Furthermore, temperature dependent 7Li NMR studies provided a rough estimate of the rate of Li^+ ion exchange between the inside and outside of the capsule: $\sim3\times10^4$ per minute at 343K [personal communication]

Here we have detailed and simulated a method for embedding porous POM nanocapsules in lipid bilayer membranes. By combining the highly charged porous nanocapsule (6.1) with a cationic amphiphilic surfactant (DODA) and a model phospholipid (POPC) we demonstrated that liposome-like, water soluble structures form spontaneously around the capsule. These liposome-like structures were shown to insert the porous nanocapsule into lipid bilayer membranes. This process can be further optimized by using specific lipid types that facilitate membrane fusion and by covalently linking DODA-like moieties to the porous nanocapsule to prevent competition between DODA and smaller cations which can destabilize the capsule/bilayer assembly. Future studies are required to investigate the long-time stability of the capsule/membrane system and develop a method for exposing the surface of the capsule to the electrolyte via self-assembly. The latter will require employing lipids of specific spontaneous curvature, charge and hydrophobic tail length. The successful inclusion of porous nanocapsules in lipid bilayer membranes is the first step to creating a synthetic model of ion channels that would allow studies of ionic transport in greater detail than it is currently possible. In this context it is important that the capsule functionalities can be tuned by changing the internal ligands like sulphates (see formula above) and that the nanocapsules are stable in aqueous solutions [23].

Appendix A

Immunosurfaces for Bacterial Detection

Reproduced in part from: Radadia AD, Stavis CJ, Carr R, Zeng H, King WP, Carlisle JA, Aksimentiev A, Hamers RJ, Bashir R (2011) Control of Nanoscale Environment to Improve Stability of Immobilized Proteins on Diamond Surfaces. Adv. Funct. Mater. *21(6):1040-1050 [2] (Copyright © 2011 WILEY-VCH Verlag GmbH & Co.); and Carr R, Comer J, Aksimentiev A (in press) Modeling the Interface between Biological and Nanotechnological Systems. In* Simulations in Nanobiotechnology. *(Copyright © 2011 CRC Press, LLC) [41].*

A.1 Molecular dynamics methods

Molecular dynamics simulations of UNCD and silica immunosurfaces. All molecular dynamics (MD) simulations were performed using the program NAMD [43], particle mesh Ewald (PME) electrostatics [77], periodic boundary conditions, and a multiple time step integration scheme consisting of a 2-fs time step for bonded and non-bonded calculations and a 6-fs time step for long-range electrostatics. Water bonds and angles were kept rigid with SETTLE [149], while all other covalent bonds with hydrogen were kept rigid with RATTLE [150]. Simulations in the NPT ensemble (constant number of particles N, pressure P and temperature T) were performed using a Langevin thermostat [113] and Nos-Hoover Langevin piston pressure control [114] set at 310.15 K (37° C) and 1 atm, respectively; the area of the unit cell within the plane coincident with the plane of the surface was kept constant. The damping coefficient of the Langevin thermostat was 1 ps^{-1}; the thermostat was applied only to the atoms of the substrate (diamond or silica). A smooth (1.0–1.2 nm) cutoff was used to compute the van der Waals forces. All simulations were performed using the CHARMM [44] force field for diamond, aminopropyl, aminodecane, and the TIP3P water model, the CHARMM-compatible force field for ions [151] and a custom CHARMM-compatible force field for silica [49]. The CHARMM fore field has been shown to properly model both short- and long-range non-bonded interactions for diamond carbons at ambient temperatures [152]. The silica membrane was generated using the BKS potential [75, 76].

A.2 Details of the atomic-scale model

To produce the silica membrane used in this study, we created a 2.5 x 2.5 x 3.5 nm^3 block of crystalline silica containing 500 silicon and 1000 oxygen atoms by replicating a unit cell of SiO_2. The membrane was annealed through NVT simulations in a 2.5 x 2.5 x 5.5 nm^3 periodic cell lasting 20 ps at 7000 K, 20 ps at 5000 K , 50 ps at 2000 K, 100 ps at 1000 K and finally 50 ps at 300 K. The silica annealing was performed using the BKS potential [75], modified at small distances to prevent spurious behavior at high temperature [76], a 0.55 nm cutoff for the evaluation of the van der Waals forces, and a 5 ps^{-1} Langevin damping coefficient. To prevent atoms from evaporating into the vacuum region, external forces were applied with grid-steered molecular dynamics [153]. The resulting amorphous silica slab was tiled in a two-by-two grid to create a 5.0 x 5.0 x 2.6 nm^3 silica membrane with two exposed faces consisting of four identical patches of silica. To construct the diamond membrane, a diamond unit cell was replicated and cut along the (1 1 1) face to create a 4.8 x 4.8 x 2.5 nm^3 block, periodic in the plane orthogonal to the (1 1 1) face. The exposed carbon atoms were terminated with hydrogen atoms.

To model the immunosurfaces, each membrane was coated with a covalently attached layer of aminopropylsilane (on silica) or aminodecane (on diamond) as described in Luan and Aksimentiev[154]. To study the effect of coating density, we used two simulation systems for each substrate material. For silica surfaces, each face of the substrate was coated with a layer of 25 or 62 (system 1), or 100 or 151 (system 2) aminopropylsilane molecules, corresponding to a density of 1.0, 2.5, 4.0 or 6.0 x 10^{14} molecules/cm^2, respectively. Similarly, a pair of simulation systems containing a UNCD membrane was coated with a layer of 25 or 60 (system 1), or 35 or 46 (system 2) aminodecane molecules, corresponding to a density of 1.0, 2.6, 1.5 or 2.0 x 10^{14} molecules/cm^2, respectively. The resulting functionalized surfaces were submerged in a 0.138 M NaCl solution consisting of 5,194 water molecules, 13 Na^+ and 13 Cl^- ions, producing final systems of 22,652 (silica 1), 24,620 (silica 2), 29,196 (UNCD 1), and 29,068 (UNCD 2) atoms. Prior to energy minimization, all water molecules located within 0.3 nm of the substrate or coating molecules were moved into the bulk solution. Following 2000 steps of energy minimization using the conjugate gradient method, each system was subjected to an initial equilibration for 5 ns with all the heavy atoms of the aminopropylsilane or aminodecane molecules harmonically restrained (with spring constants of 1.0 kcal/mol/$Å^2$) to their initial conformations, which allowed the water and ions to approach thermal equilibrium. Following that, the harmonic restraints on the aminopropylsilane or aminodecane molecules were released, and each system was simulated in the NPT ensemble for at least 40 ns. For all simulations, all substrate atoms (silica or UNCD carbon atoms) were harmonically restrained with spring constants of 20.0 kcal/mol/$Å^2$.

A.3 Modeling the degradation of functionalized silica

To model the degradation of the 4.0 x 10^{14} molecules/cm^2 aminopropylsilane functionalization layer on the silica substrate, we performed an eight-step molecular dynamics simulation starting from the coordinates obtained from the simulations of silica system 2. We assumed that the probability of losing a functional group is directly proportional to the total exposure of the Si-C bond to water. Hence, to choose the functionalization groups for removal, a 1-ns fragment of the simulation trajectory was used to compute the average number of water molecules located within 3 Å of each aminopropylsilane group and 0.5 nm within the silica substrate. All aminopropylsilane groups were ranked according to the average number of contacts with this water; the top 10% (rounding down) were removed. Following 2000 steps of energy minimization, the resulting system was simulated for 2.5 ns. This procedure was repeated 8 times, until the density of aminopropylsilane molecules fell to 75% of the original density, or 3.0 x 10^{14} molecules/cm^2. Figure 2.4 illustrates the results of these simulations.

A.4 Potential of mean force calculations

To study the interaction between amino acids and the immunosurfaces, we created 15 systems consisting of a 0.138 M aqueous solution of NaCl , one copy of an amino acid and one of the following three functionalized substrates: The 1.0 / 2.6 x 10^{14} molecules/cm2 aminodecane UNCD substrate; the 4.0 / 6.0 x 10^{14} molecules/cm^2 aminopropylsilane silica substrate; or the 3.0 / 6.0 x 10^{14} molecules/cm^2 aminopropylsilane substrate created through the degradation process described above. For each functionalized substrate, five systems were created corresponding to the five types of amino acids that we used to model the interactions of surfaces with the antibody protein: Lysine (charged, positive); aspartic acid (charged, negative); asparagine (polar); valine (nonpolar); and tyrosine (aromatic). The systems containing charged amino acids were made electrically neutral by adding an extra chloride or sodium counterion. Prior to PMF calculations, each system was subject to 2000 steps of energy minimization followed by a 3-ns equilibration in the NPT ensemble. The potential of mean force (PMF) of an amino acid as a function of its position relative to the substrate surface was determined from a set of umbrella sampling simulations, which were analyzed using the weighted histogram analysis method (WHAM) [100]. The umbrella sampling simulations were performed by restraining the alpha-carbon atom of an amino acid to a specified distance z from the substrate surface using the following potential energy function: $w_i(z) = \frac{1}{2}k_z(z - z_i)^2$, where z_i was the center of sampling window i and $k_z = 4$ kcal/mol/Å^2 was the spring constant. The location of the amino acids within the plane of the substrate was harmonically restrained using a spring constant of 0.8 kcal/mol/Å^2. The sampling windows

were placed every 0.06 nm for either $1.5 < z < 2.82$ nm (silica) or $1.5 < z < 3.42$ nm (UNCD), for a total of 23 or 33 windows, respectively. Following 200 steps of energy minimization, the system in each window was simulated at fixed volume for at least 6 ns, with the first 0.2 ns of each simulation excluded from the WHAM PMF calculation.

Appendix B

Modeling Protein Transport through Nanochannels

Reproduced in part from: Carr R, Comer JR, Ginsberg MD and Aksimentiev A (2011) Modeling Pressure-Driven Transport of Proteins through a Nanochannel IEEE Tran. Nanotechnol. *10(1):75–82 (Copyright © 2010 IEEE) [29].*

B.1 All-atom molecular dynamics

All molecular dynamics (MD) simulations were performed using the program NAMD [43], a 1 fs integration time step, particle mesh Ewald (PME) electrostatics [77], and periodic boundary conditions. Simulations in the NPT ensemble (constant number of particles N, pressure P and temperature T) were performed using a Langevin thermostat [113] and Nosé-Hoover Langevin piston pressure control [114] set at 295 K and 1 atm, respectively. The damping coefficient of the Langevin thermostat was 1 ps^{-1}, unless specified otherwise; the thermostat was applied only to the atoms of the nanochannel surface. A smooth (1.0–1.2 nm) cutoff was used to compute the van der Waals forces. External potentials were applied using grid-steered molecular dynamics (G-SMD) [153]. The nanochannel simulations were performed using the CHARMM [44] force field for water, ions and proteins and a custom forcefield for silica [49]. The charges of the silicon and oxygen atoms of silica were set to 0.9 e and -0.45 e, respectively, and the Lennard-Jones parameters were $r_{\mathrm{Si}}^{\mathrm{min}}$ =0.4295 nm, ϵ_{Si} =0.3 kcal/mol, $r_{\mathrm{O}}^{\mathrm{min}}$ =0.35 nm, and ϵ_{O} =0.15 kcal/mol. The silica membranes were generated using the BKS potential [75, 76] and the Inorganic Builder of VMD [155] (see below).

Appendix C

Microscopic perspective on the adsorption isotherm of a heterogeneous surface

Reproduced in part from Carr R, Comer J, Ginsberg M. D, Aksimentiev A. (2011) Microscopic perspective on the adsorption isotherm of a heterogeneous surface. J Phys Chem Lett *2:1804–1807.*

C.1 Molecular dynamics simulations.

All molecular dynamics (MD) simulations were performed using the program NAMD [43], a 1 fs integration time step, particle mesh Ewald (PME) electrostatics [77], and periodic boundary conditions. Simulations in the NPT ensemble (constant number of particles N, pressure P and temperature T) were performed using a Langevin thermostat [113] and Nosé-Hoover Langevin piston pressure control [114] set at 295 K and 1 atm, respectively. The damping coefficient of the Langevin thermostat was 1 ps^{-1} and was applied only to the atoms of the silica surfaces, unless specified otherwise. A smooth (1.0–1.2 nm) cutoff was used to compute the Lennard-Jones forces. External potentials were applied using grid-steered molecular dynamics (G-SMD) [153]. All simulations were performed using the TIP3P water model modified for the CHARMM [44] force field and a CHARMM-compatible model for silica [49], except during membrane generation. In the simulations of solute adsorption, the charges of the silicon and oxygen atoms of silica were set to 0.9 e and -0.45 e, respectively, and the Lennard-Jones parameters were $r_{\mathrm{Si}}^{\mathrm{min}}$ =0.4295 nm, ϵ_{Si} =0.3 kcal/mol, $r_{\mathrm{O}}^{\mathrm{min}}$ =0.35 nm, and ϵ_{O} =0.15 kcal/mol.

C.2 All-atom model for dimethyl methylphosphonate (DMMP).

To model DMMP, we have adapted the united-atom DMMP parameters developed by Vishnyakov and Neimark [156] for use with the CHARMM force field [44]. Tables SC.1 a–e list the all-atom parameters for DMMP based on the original united-atom model [156] with additions from the CHARMM force field [44] and quantum chemical calculations [157, 158]. The parameters for DMMP provided by Vishnyakov and Niemark were not charge neutral. To correct this, we subtracted 0.004 e from the charge of the phosphorus oxygen

and 0.002 e from the charge of each methyl carbon, where e is the charge of a proton. The addition of three hydrogens was performed according to the standard CHARMM parameter protocol. That is, hydrogens were each given a charge of +0.09 e; this was balanced by subtracting an equal amount of charge from the parent atom. A list of all the atomic charges is given in Table SC.1 a.

To compare our parameters to those of Vishnyakov and Neimark [156], we created two test systems of DMMP solvated in TIP3P [79] water at 4.6 and 1.1 mol/L concentrations. The first system recreates "mixture I" in [156], while the second system tests our model at lower concentration. MD simulations were performed on both systems in the NPT ensemble at 303 K and 1 atm for 10 ns. The parameters of Vishnyakov and Neimark [156] were developed for a 1-4 scaling factor of 0.5, but our model of silica uses a 1-4 scaling factor of 1.0. In order to determine whether our adapted DMMP parameters could be used with a 1-4 scaling factor of 1.0, we performed each simulation twice, once with each 1-4 scaling factor.

Table C.2 shows a comparison of the all-atom model with the united-atom model. Like the united-atom DMMP molecules, our all-atom DMMP molecules do not aggregate in solution. To determine the diffusion constant of DMMP in water, we have measured the mean squared displacement (MSD) of the DMMP molecules over all independent 10, 20, 50, 100, 200, 500, 1000, 2000 and 5000 ps periods during our simulations and used weighted linear regression to calculate $\frac{d}{dt}(\text{MSD})$. The Einstein relation

$$\left\langle r^2(t) \right\rangle = 6Dt$$

or, in terms of the MSD

$$D = \frac{1}{6} \lim_{t \to \infty} \frac{d}{dt}(\text{MSD}),$$

was used to calculate the diffusion constant. The measured diffusion constant of DMMP in water with our parameters is found to be 13% be greater than DMMP as described by the united-atom parameters at the same concentration. At a concentration of 1.1 mol/L, the diffusivity of DMMP increases by almost a factor of two. Hydrogen bonding between water and the DMMP oxygens was considered using the same metrics as in Vishnyakov and Neimark [156]: A distance cutoff of 3.4 Å and a minimum O-H-O angle of 120 degrees. Our model shows a higher affinity for accepting hydrogen bonds than the united-atom model [156], but is within the experimental range of 2–3 hydrogen bonds per molecule in pure water [159]. The difference between the results for diffusion and hydrogen bonding is most likely due to the difference in water models. The self-diffusion of TIP3P water used in our simulations is more than twice that of the SPC/E model used in [156], which leads to quicker diffusion for solutes in our simulations. In addition, the united-atom simulations used rigid SPC/E water, which may have reduced the hydrogen-bonding count. The use of 1-4

scaling of 0.5 or 1.0 had no measurable effect on the dynamics of DMMP. In accordance with our silica parameters, a 1-4 scaling of 1.0 was used for all further simulations. To test the DMMP parameters at the same temperature and similar concentration to our adsorption chamber simulations, we created a third system at 0.62 mol/L concentration and simulated it in the NPT ensemble for 10 ns at 295 K. The results of this simulation, presented in Table C.2, show that the diffusion constant remains the same, while the affinity for accepting hydrogen bonds increases slightly to 2.8 hydrogen bonds per molecule.

(a)

Atom	Charge (e)
P^*	1.17
O2	−0.695
OS	−0.36
$CT3_P$	−0.291
$CT3_{OS}$	−0.137
$HC3^{\nabla}$	0.09

(b)

Bond	Length (Å)	Strength (kcal/mole/Å^2)
CT3 P	1.795*	1.86†
CT3 $HC3^{\nabla}$	322.0	1.111
CT3 OS^{∇}	340.0	1.43
OS P^{∇}	269.0	1.60
O2 P^{∇}	580.0	1.48

(c)

Angle	Theta (degrees)	Strength (kcal/mole/Å^2)	U-B Length (Å)	(U-B) Strength (kcal/mole/Å^2)
OS P OS^{∇}	104.3	80.0		
HC3 CT3 OS^{∇}	109.5	60.0		
HC3 CT3 $HC3^{\nabla}$	108.40	35.500	5.40	108.40
O2 P CT3*	116.3	80.0		
CT3 P OS*	104.3	40.6		
O2 P OS*	116.5	100.1		
P OS CT3*	121.0	80.0		
P CT3 $HC3^\dagger$	110.0	50.0		

(d)

Dihedral	K_χ (kcal/mole)	n	Δ (degrees)
CT3 P OS CT3*	0.0671	1	0.00
CT3 P OS CT3*	0.6289	2	0.00
CT3 P OS CT3*	0.0755	3	0.00
CT3 P OS CT3*	−0.0582	4	0.00
CT3 P OS CT3*	0.0733	5	0.00
CT3 P OS CT3*	−0.0060	6	0.00
HC3 CT3 P OS*	0.0000	3	0.00
HC3 CT3 P O2*	0.0000	3	0.00
O2 P OS CT3*	0.1004	3	0.00
OS P OS CT3*	0.9536	2	0.00
OS P OS CT3*	0.5019	3	0.00
X CT3 OS X^{∇}	0.00	3	0.00

(e)

Atom	epsilon	Rmin/2 (Å)
$HC3^{\nabla}$	−0.024	1.3400
P^*	−0.347	1.192
O2*	−0.159	1.47
CT3*	−0.208	1.90
OS*	−0.159	1.52

Table C.1: All-atom, CHARMM-compatible parameters for MD simulations of DMMP. The tables specify (a) charge, (b) bond, (c) angle, (d) dihedral and (e) lennard-jones parameters. The parameters are based on the united-atom model [156] (indicated with an *), modified in accordance with the CHARMM force field [44]($^{\nabla}$) and *ab initio* quantum chemical calculations [157, 158] (†).

System	# Atoms	[DMMP], (mol/L)	Duration (ns)	1-4 Scaling	D, $10^{-6}\cdot cm^2/s$	# Hydrogen Bonds
UA	1419	4.6	0.5	0.5	4.5	1.7
I	13,728	4.6	9.5	0.5	5.2 ± 0.1	2.2
I	13,728	4.6	10	1.0	5.0 ± 0.2	2.3
II	10,528	1.1	10	0.5	9.3 ± 0.2	2.5
II	10,528	1.1	10	1.0	9.2 ± 0.1	2.5
III	57,296	0.62	10	1.0	9.1 ± 0.1	2.8

Table C.2: Comparison of the united-atom (UA) model of DMMP [156] with our all-atom model at three concentrations of DMMP. Simulations of systems I and II were performed using two values of 1-4 scaling: 0.5 and 1.0.

C.3 All-atom model for synthetic surfaces.

To produce the silica membrane used in this study, we created a $2.5 \times 2.5 \times 3.5$ nm^3 block of crystalline silica containing 500 silicon and 1000 oxygen atoms by replicating a unit cell of SiO_2. The resulting system was annealed through NVT (constant number of particles N, volume V and temperature T) simulations for 20 ps at 7000 K, 20 ps at 5000 K, 50 ps at 2000 K, 100 ps at 1000 K, and 50 ps at 300 K using the BKS potential [75, 76] and a $2.5 \times 2.5 \times 5.5$ nm^3 periodic cell, to produce an amorphous silica membrane with two relaxed surfaces (normal to the z-axis). As in Vollmayer et al. [76], the form of the BKS potential was modified at small distances to prevent spurious behavior at high temperature. The Coulomb portion of the BKS potential was computed using the PME method [77], while the Lennard-Jones portion was smoothly shifted to zero at an interatom distance of 0.55 nm. During the annealing procedure, an external force was applied to prevent the atoms from evaporating into the vacuum region. The temperature was controlled by Langevin dynamics with a damping constant of 5 ps^{-1}.

From the results of the annealing simulations, we created four SiO_2 surfaces, each with different surface properties. Surfaces A and B were generated by removing atoms within 0.42 nm of the top and bottom surfaces from the structure at the end of the annealing process, resulting in two different surfaces that were similar to cross sections of bulk amorphous silica. The resulting structure, having surface A as its bottom surface and surface B as its top surface is referred to as system AB. System A was created by splitting system AB in half and replicating and rigidly transforming the half containing surface A to produce a silica slab having identical surfaces (A) on the top and bottom.

The same replication and transformation procedure was used to produce system C using the bottom half of the SiO_2 block and the atomic coordinates from the first step of the annealing procedure—20 ps at 700 K. This system had similar properties to the system used in Carr et al. [29]. System D was made in the same way as system C except that atomic coordinates from the end of the annealing procedure were used. Thus, the two identical surfaces of system D can be thought of as more relaxed than the two identical surfaces of

system C due to the more gradual annealing process in the first case.

The use of the BKS force field in the annealing simulations was to produce plausible atomic structures for the SiO_2 surfaces. In the subsequent simulations of the adsorption chamber, the SiO_2 atoms were restrained to the positions generated by the annealing simulations [49, 29, 160]. The strength of the restraints and bonds were chosen to give the membrane a dielectric constant of ~ 5. The restraint force was given by $F(\vec{r}_i) = -2K(\vec{r}_i - \vec{R}_i)$, where $\vec{r}_i$ and $\vec{R}_i$ are the current and initial positions of atom i and $K = 13,900$ pN/nm. Bonds were established between all silicon and oxygen atoms separated by < 0.22 nm using with $K_{\text{bond}} = 695$ pN/nm. The interaction of the SiO_2 atoms with water and DMMP were calculated using the CHARMM compatible force field of Cruz-Chu et al. [49].

To separate the effects of surface roughness from other surface features, a fifth surface, which we will refer to as the phantom or Ph surface, was used. This surface did not consist of atoms; instead an infinitely smooth, frictionless surface was modeled by applying the following smooth potential to all atoms using G-SMD [153].

$$U(z) = \begin{cases} U_0 & \text{if } |z| \leq z_0 \\ 0 & \text{if } |z| \geq z_0 + 2l \\ \frac{1}{4}U_0 \left(2 - 3\frac{|z|-(z_0+l)}{l} + \left(\frac{|z|-(z_0+l)}{l} \right)^3 \right) & \text{otherwise} \end{cases}$$

where $U_0 = 5$ eV, $l = 0.2$ nm, and $z_0 = 1.25$ nm.

C.4 Solute adsorption simulations and analysis.

The simulations of solute adsorption were performed using atomic-scale models of small chambers that contained DMMP solution enclosed between two surfaces (see Figure 1). Systems A, AB, C and D were created using silica slabs A, AB, C, D, respectively, tiled in a four-by-four grid to create new slabs consisting of sixteen identical patches, measuring 10×10 nm^2 in total area. System Ph was created using a phantom surface slab (Ph, described above), measuring 10×10 nm^2 in area. To create the enclosed chambers, the silica or phantom slab was placed in a periodic box with the same width and breadth as the slab, but with a height greater than that of the slab, creating systems that were effectively infinitely long and wide, with a gap of 5 to 6 nm separating the surfaces (see Figure 1). The volume between the surfaces was then filled with a solution of DMMP.

Following a 2000-step minimization using a conjugate gradients method, each system was equilibrated for 1.5 ns in the NPAT ensemble (constant number of particles N, pressure P, area in the xy plane A and

Surface	Length (ns)	ΔP (bar)	N_{DMMP}	n_{DMMP} nm^{-2}	C_{bulk} M
A	100	71.0	25	0.078	0.035
A	100	71.0	50	0.16	0.060
A	100	70.0	100	0.30	0.13
A	100	69.0	150	0.43	0.20
A	100	69.0	200	0.56	0.28
A	50	0.0	200	0.56	0.28
A	100	67.0	300	0.76	0.46
A	100	41.0	1500	1.6	4.6
A_{AB}	100	67.0	200	0.67	0.38
B_{AB}	100	67.0	200	0.16	0.38
A_{AB}	100	41.0	1500	1.6	4.7
B_{AB}	100	41.0	1500	0.83	4.7
C	100	63.0	400	1.7	0.17
C	100	41.0	1500	2.3	4.1
D	50	60.0	200	1.0	0.005
D	100	60.0	400	2.0	0.014
D	100	60.0	600	2.3	0.43
D	100	41.0	1500	2.5	4.1
Ph	50	69.0	200	0.26	0.57
Ph	100	41.0	1500	1.5	4.7

Table C.3: Summary of solute adsorption simulations. Each simulation is characterized by the duration of the NVT portion of the simulation, the pressure difference across the chamber (ΔP), the total number of DMMP molecules (N_{DMMP}), the steady-state adsorption density (n_{DMMP}) and the steady-state bulk concentration C_{bulk} (see Figure 1). Each simulation of system AB, which contained both surfaces A and B, is listed twice, specifying adsorption densities for individual surfaces, labeled A_{AB} and B_{AB}.

temperature T). During the NPAT simulation, some DMMP molecules may have adsorbed to the surfaces. To remove this effect, all DMMP molecules were moved back to their initial coordinates, and constrained to those coordinates for a 0.5 ns simulation in the NVT ensemble, removing any steric clashes between DMMP and water molecules. Each system was then simulated in the NVT ensemble with a pressure gradient induced in the x-direction, resulting in a pressure-driven flow of DMMP solution through the system. To induce a pressure gradient, a constant force in the x-direction F_x was applied to all N water molecules, creating a pressure difference ΔP_x across the system of

$$\Delta P_x = N \cdot F_x / A, \tag{C.1}$$

where A is the area of the chamber in the yz plane [29]. Temperature was maintained by applying the Langevin thermostat to all silica atoms, which was sufficient to keep the temperature of the entire system within 1.2% of the target temperature [29]. To investigate whether the pressure-driven flow affected the amount of solute bound, we performed simulations of system A with and without the applied pressure difference, which showed that the pressure-driven flow had no measurable effect on adsorption. A summary of all solute adsorption simulations is given in Table C.3. For all simulations of the phantom channel, the

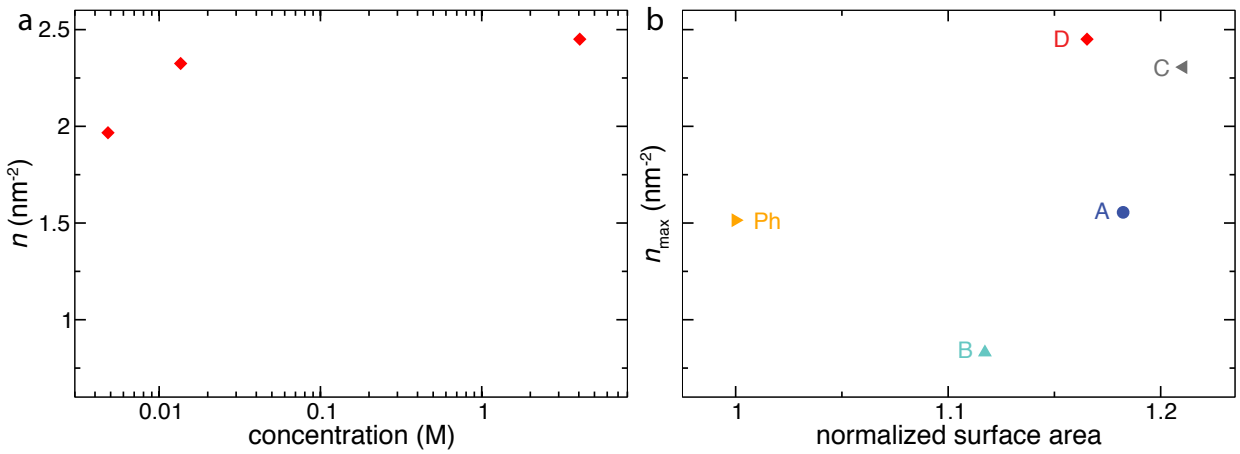

Figure C.1: Calculations of the maximum adsorption density $n_{\max}$. a) Surface density of DMMP as a function of DMMP bulk concentration for system D. b) The maximum adsorption density $n_{\max}$ as a function of the normalized surface area for each surface studied (see text).

Langevin temperature control was applied only to water oxygens with a damping coefficient of 0.1 ps^{-1}.

To calculate the solute adsorption densities at the surfaces, a DMMP molecule was considered adsorbed if its phosphorus atom, approximately the center of mass, was within 0.5 nm of the surface. The surface of each silica slab was defined as the $x-y$ plane with the z coordinate determined as the average z coordinate of the isosurface defined by the five-to-one ratio of silica and water atoms. The region extending 0.5 nm away from that surface is referred to as the adsorption layer, see Figure 1.

C.5 Calculations of the maximum adsorption density.

The maximum adsorption density $n_{\max}$ was computed for each surface and was found to depend on its atomic-scale features. To determine $n_{\max}$, we used the expression for the Langmuir isotherm in terms of the adsorption densities,

$$n = n_{\max}\frac{\alpha C_{\text{bulk}}}{1+\alpha C_{\text{bulk}}}. \tag{C.2}$$

In the limit of high concentration, the surface density n asymptotically approaches $n_{\max}$. To determine $n_{\max}$, we performed brute-force simulations of DMMP adsorption in system D for a range of DMMP concentrations. The resulting dependence of surface density on bulk concentration is shown in Figure C.1 a. As the bulk concentration increased, the adsorption density approached a constant value. Thus, we chose $n_{\max}$ for surface D to be the adsorption density at the highest bulk concentration simulated, which was 4.1 M. As surface D has the highest affinity to DMMP of all surfaces considered, to determine $n_{\max}$ for the other four surfaces (A, B, C and Ph), we simulated systems A, AB, C and Ph at the same initial DMMP concentration

as the one that yielded $n_{\max}$ for system D. The simulation of system AB was used to determine $n_{\max}$ for surface B. To verify that the presence of two surfaces (A and B) in one simulation did not affect the determination of $n_{\max}$, we compare the value of $n_{\max}$ for surface A calculated through simulation of system A with that calculated through simulation of system AB. The value of $n_{\max}$ for surface A in system AB at 4.7 M: 1.7 molecules/nm^{-1} agreed with the value in system A at 4.6 M: 1.7 molecules/nm^{-1}.

The value of $n_{\max}$ for each surface is shown in Figure C.1 b, plotted as a function of the normalized surface area. The normalized surface area was calculated as the solvent-accessible surface area (SASA) divided by the planar ($x-y$ plane) area of the slab. To calculate the SASA, we used the 'measure sasa' feature of the Visual Molecular Dynamics (VMD) [85] package, using a solvent radius of 1.4, the approximate radius of a water molecule. Figure C.1 b shows that $n_{\max}$ is not a simple geometric parameter. Approximating a DMMP molecule as a disk of radius 0.23 nm (the radius of gyration) that packs in a hexagonal lattice with a packing density of 0.9069, one would expect $n_{\max}$ to correspond to a density of $\sim$5.6 molecules nm^{-2}. However, the observed maximum adsorption densities are much lower and depend on the properties of individual surfaces. Furthermore, Figure C.1 b shows that $n_{\max}$ is not a function of the normalized surface area, meaning that variation in $n_{\max}$ is not caused by the variation in the surface area of the slabs, even after taking into account the atomic scale roughness.

C.6 Umbrella sampling simulations.

To study the interaction between a single DMMP and the membrane surfaces, we created 5 small systems consisting of a single slab of silica membrane or an equal size phantom membrane, water, and one DMMP molecule. The potential of mean force (PMF) of a DMMP molecule as a function of its position relative to the membrane surface was determined from a set of umbrella sampling simulations [99], which were analyzed using the weighted histogram analysis method (WHAM) [100] generalized to three dimensions (see below). Prior to the umbrella sampling simulations, each of the four systems underwent 2000 steps of energy minimization, 2 ps of equilibration at fixed volume during which the temperature was raised from 0 to 295 K by velocity rescaling, and 200 ps of NPT simulation.

The umbrella sampling simulations were performed by restraining the phosphorus atom of the DMMP molecule to points in (x, y, z) (where z is perpendicular to the surface) using the potential energy function $w_i(x,y,z) = \frac{1}{2}k_x(x-x_i)^2 + \frac{1}{2}k_y(y-y_i)^2 + \frac{1}{2}k_z(z-z_i)^2$, where (x_i, y_i, z_i) was the center of sampling window i and k_x, k_y and k_z were the spring constants along each axis. Because the gradient of the PMF was much larger along the z axis than in the xy plane, a stiffer spring constant of k_z =1390 pN/nm was used along

the z axis than perpendicular to it, for which $k_x = k_y$ =70 pN/nm. Furthermore, the sampling windows (x_i, y_i, z_i) were more closely spaced along the z axis. The sampling windows formed a three-dimensional grid with 4, 4, and 9 points along the x, y, and z directions, respectively. Results were first obtained using the 144 sampling windows centered at these points, but to increase the resolution of our PMF distributions, we added another 300 sampling windows. For these simulations, we used a grid of 5, 5, and 12 points with spring constants $k_x = k_y = 560$ and $k_z = 2780$ pN/nm. To ensure that the calculated PMF extended into bulk water, 19 sampling windows with the same spring constant as the previous set were added to the (x,y) center of the slab for an additional nanometer in z. Each simulation represented more than 2.2 ns. The first 0.2 ns of each simulation was excluded from the WHAM PMF calculation.

C.7 Potential of mean force calculation.

The potential of mean force (PMF) is computed by the weighted histogram analysis method (WHAM) described by Roux [100] generalized to three dimensions. Each of the three spatial dimensions is a reaction coordinate. We estimate the unbiased probability distribution by

$$\langle \rho(x,y,z) \rangle = \left(\sum_{i=1}^{N_w} n_i \ \langle \rho_i(x,y,z) \rangle \right) \left(\sum_{j=1}^{N_w} n_j \exp\left[-\frac{w_j(x,y,z) - F_j}{k_\mathrm{B}T} \right] \right)^{-1}, \tag{C.3}$$

where $\rho(x,y,z)$ is the unbiased probability distribution, N_w is the number of biased simulations, $\rho_i(x,y,z)$ is the biased probability distribution derived from the results of biased simulation i, n_i and $w_i(x,y,z)$ are the number of independent data points and the biasing potential, respectively, for biased simulation i, and $\{F_i\}$ is a set of constants.

The set of constants $\{F_i\}$ are initially unknown; thus, we make an initial guess for their values. After estimating $\langle \rho(x,y,z) \rangle$ by Equation C.3, we can obtain improved estimates these constants by solving

$$\exp\left[-\frac{F_i}{k_\mathrm{B}T} \right] = \int \mathrm{d}x \int \mathrm{d}y \int \mathrm{d}z \exp\left[-\frac{w_i(x,y,z)}{k_\mathrm{B}T} \right] \langle \rho(x,y,z) \rangle \,. \tag{C.4}$$

To obtain self-consistency, the equations are iterated, feeding the newest estimate of $\{F_i\}$ into Equation C.3 and then the newest estimate of $\langle \rho(x,y,z) \rangle$ into Equation C.4. Iteration ceases at iteration j when $\left| (F_{i+1} - F_i)^{(j)} - (F_{i+1} - F_i)^{(j-1)} \right| < 0.0001\, k_\mathrm{B}T$ for all windows $i \in \{1, 2, ..., N_w - 1\}$. The PMF is then computed by $-k_\mathrm{B}T \log(\langle \rho(x,y,z) \rangle)$.

C.8 Surface Characterization.

To characterize the atomic-scale features of the surfaces, we computed the local surface roughness and the local surface charge density of each surface. Topographical maps of the surfaces, shown in Figure C.2, were generated using hard spheres with radii of 0.2 nm as probes and considering the silicon and oxygen atoms as hard spheres with radii of 0.2147 nm and 0.175 nm, respectively. To compare the surfaces, the reference height $z = 0$ was defined to be the mean value of z (direction normal to the plane of the slab) over the topographical map of that surface. The the root-mean-square (RMS) roughness for each surface was then computed from the topographical maps. In Figure C.3, the Langmuir constant for each surface is shown as a function of its RMS roughness.

The surface charge density for each surface was computed using the 'volmap' tool in Visual Molecular Dynamics (VMD) [85]. To compute the surface charge density, the charge of each atom comprising the silica slab was distributed over a three-dimensional grid of 0.42 Å resolution by approximating each atom as a normalized Gaussian distribution with width equal to the radius of the atom and taking into account the periodicity of the system. The resulting three-dimensional grid, periodic in x and y, described the charge density in the system produced by the silica atoms. Following that, we defined a surface charge layer as the volume above the plane located 2 Å below the silica surface (defined in "Solute adsorption simulations and analysis" above). The local surface charge density, shown in the bottom row of Figure C.2, was calculated as the total charge density of the surface layer at each (x,y) coordinate. In Figure C.4, the Langmuir constant is shown as a function of the total surface charge of each silica surface. We found the plot of the Langmuir constant versus the total surface charge to sensitively depend on the definition of the surface charge layer, in contrast to the dependence of the Langmuir constant on the RMS charge density, Figure 5a, which was robust with respect to the definition of the surface charge layer.

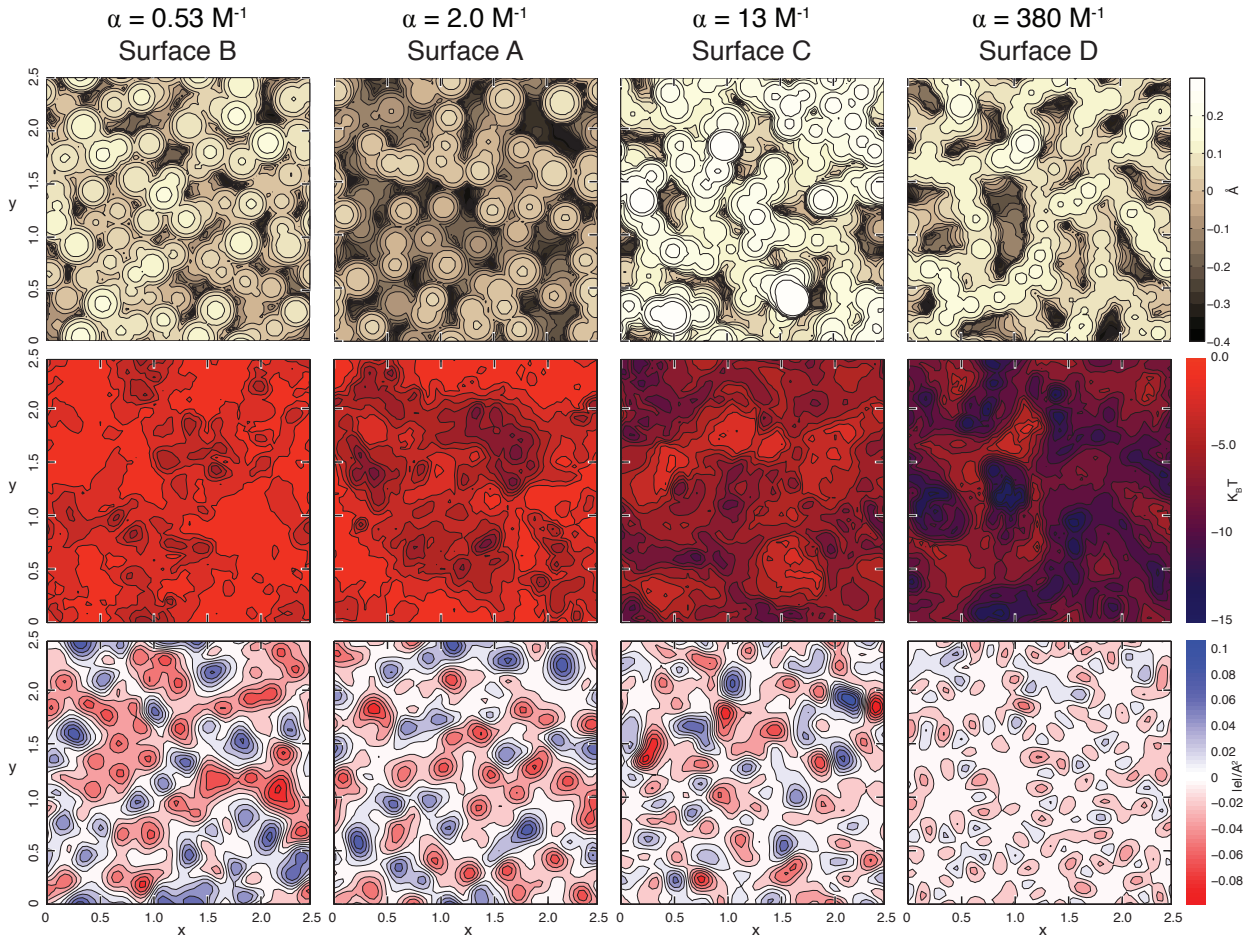

Figure C.2: Comparison of the atomic-scale features of the silica surfaces, ordered by increasing Langmuir constant. The surface features are shown on a two-dimensional grid with a resolution of 0.42 Å. (Top row) Topography of each surface, where z=0 is the mean value of z for that individual surface. (Middle row) Two-dimensional projection of the PMF minima. At each (x,y) point, the minimum value of the PMF along the line normal to the $x - y$ plane is shown. (Bottom row) The local charge density of the silica surfaces averaged over the respective MD trajectories (see text).

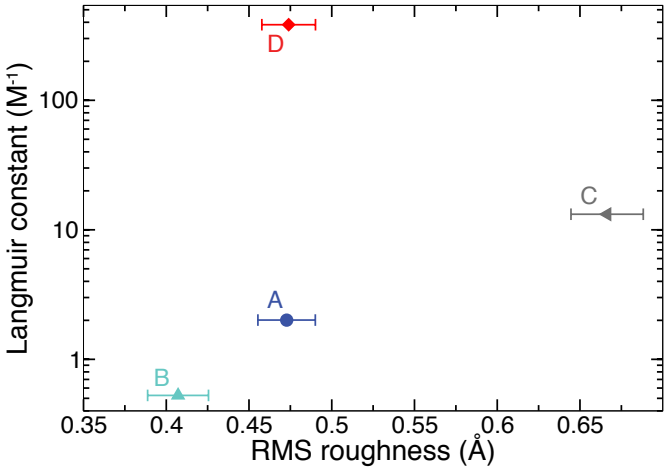

Figure C.3: The Langmuir constant as a function of the root mean square (RMS) roughness of the surface.

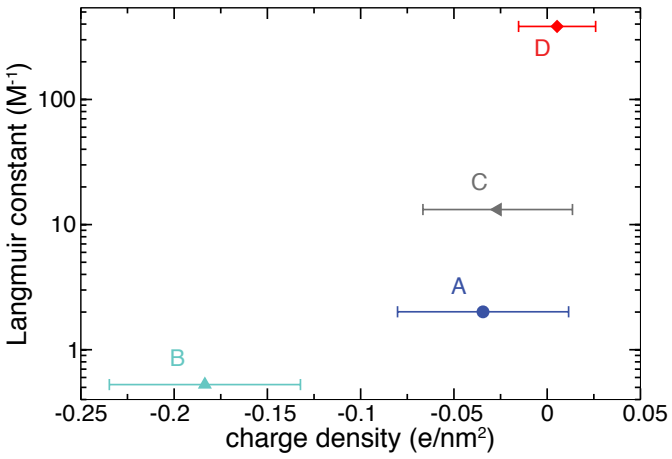

Figure C.4: The Langmuir constant as a function of the total charge density of the surface.

Appendix D

Atoms-to-microns model for small solutes transport through sticky nanochannels

*Reproduced in part from Carr R, Comer JR, Ginsberg MD and Aksimentiev A (*in preparation*) Atoms-to-microns model for small solutes transport through sticky nanochannels.*

D.1 All-atom model for synthetic surfaces.

To produce the silica membrane used in this study, we created a $2.5 \times 2.5 \times 3.5$ nm^3 block of crystalline silica containing 500 silicon and 1000 oxygen atoms by replicating a unit cell of SiO_2. The resulting system was annealed through NVT (constant number of particles N, volume V and temperature T) simulations for 20 ps at 7000 K, 20 ps at 5000 K, 50 ps at 2000 K, 100 ps at 1000 K, and 50 ps at 300 K using the BKS potential [75, 76] and a $2.5 \times 2.5 \times 5.5$ nm^3 periodic cell, to produce an amorphous silica membrane with two relaxed surfaces (normal to the z-axis). As in Vollmayer et al. [76], the form of the BKS potential was modified at small distances to prevent spurious behavior at high temperature. The Coulomb portion of the BKS potential was computed using the PME method [77], while the Lennard-Jones portion was smoothly shifted to zero at an interatom distance of 0.55 nm. During the annealing procedure, an external force was applied to prevent the atoms from evaporating into the vacuum region. The temperature was controlled by Langevin dynamics with a damping constant of 5 ps^{-1}.

From the results of the annealing simulations, we created four SiO_2 surfaces, each with different surface properties. Surfaces A and B were generated by removing atoms within 0.42 nm of the top and bottom surfaces from the structure at the end of the annealing process, resulting in two different surfaces that were similar to cross sections of bulk amorphous silica. The resulting structure, having surface A as its bottom surface and surface B as its top surface is referred to as system AB. System A was created by splitting system AB in half and replicating and rigidly transforming the half containing surface A to produce a silica slab having identical surfaces (A) on the top and bottom.

The same replication and transformation procedure was used to produce system C using the bottom half of the SiO_2 block and the atomic coordinates from the first step of the annealing procedure—20 ps at 700 K.

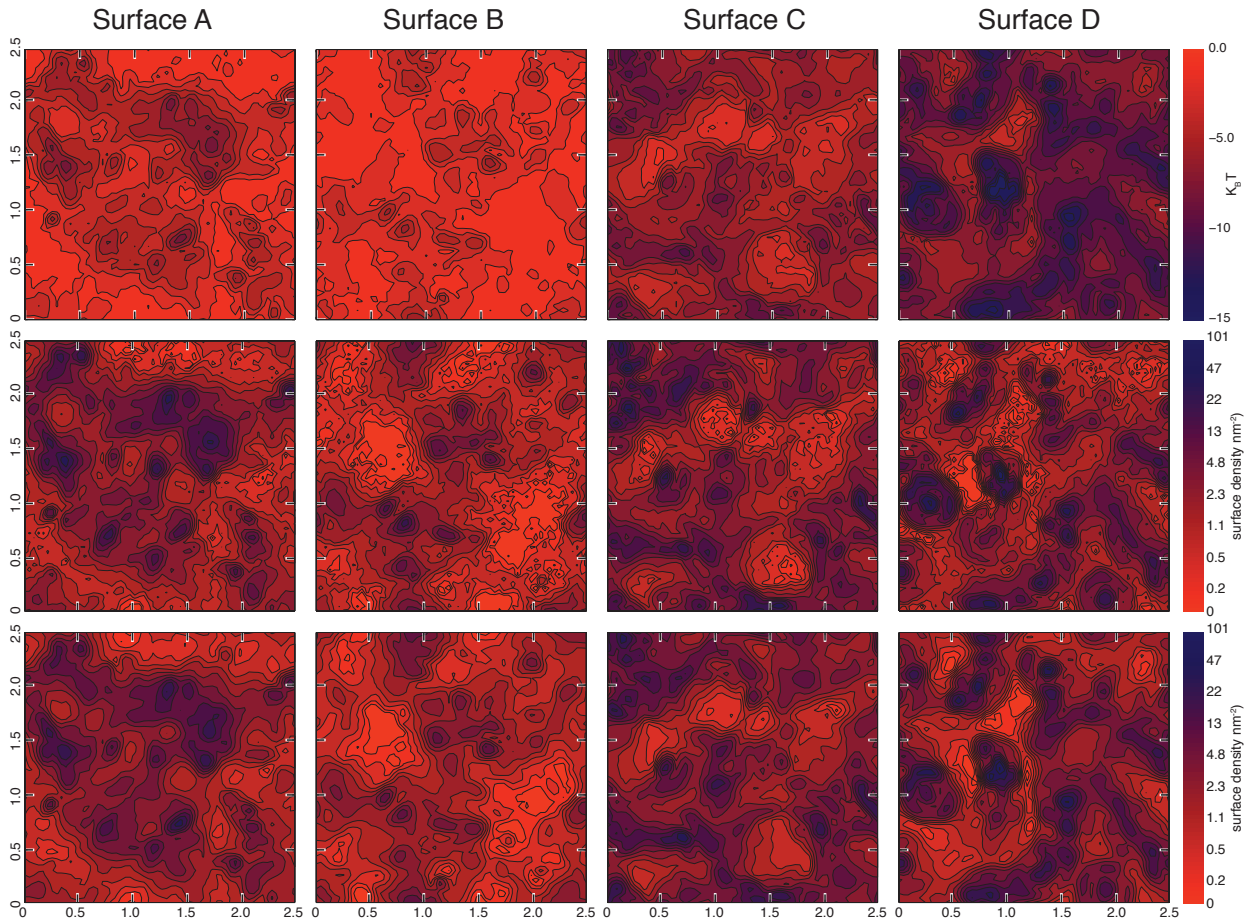

Figure D.1: Comparison of the surface adsorption density on the silica surfaces for MD and BD with the calculated DMMP–Silica surface PMFs. The surface features are shown on a two-dimensional grid with a resolution of 0.42 Å. (Top row) Two-dimensional projection of the PMF minima. At each (x,y) point, the minimum value of the PMF along the line normal to the $x-y$ plane is shown. (Middle row) Surface density of adsorbed DMMP molecules on the silica surface as a function of position on the surface for molecular dynamics simulations. (Bottom row) Surface density of adsorbed DMMP molecules on the silica surface as a function of position on the surface for brownian dynamics simulations. The results for the BD simulations represent the average of 25 unique trajectories starting from the same initial conditions as the one MD simulation.

This system had similar properties to the system used in Carr et al. [29]. System D was made in the same way as system C except that atomic coordinates from the end of the annealing procedure were used. Thus, the two identical surfaces of system D can be thought of as more relaxed than the two identical surfaces of system C due to the more gradual annealing process in the first case.

The use of the BKS force field in the annealing simulations was to produce plausible atomic structures for the SiO_2 surfaces. In the subsequent simulations of the adsorption chamber, the SiO_2 atoms were restrained to the positions generated by the annealing simulations [49, 29, 160]. The strength of the restraints and bonds were chosen to give the membrane a dielectric constant of ~ 5. The restraint force was given by $F(\vec{r}_i) = -2K(\vec{r}_i - \vec{R}_i)$, where $\vec{r}_i$ and $\vec{R}_i$ are the current and initial positions of atom i and $K = 13,900$ pN/nm. Bonds were established between all silicon and oxygen atoms separated by < 0.22 nm using with $K_{\text{bond}} = 695$ pN/nm. The interaction of the SiO_2 atoms with water and DMMP were calculated using the CHARMM compatible force field of Cruz-Chu et al. [49].

D.2 MD simulation setup

The MD simulations of transport through nanochannels were performed using atomic-scale models of silica nanochannels that contained DMMP solution enclosed between two surfaces (see Figure 5.1). Systems A, B, C and D were created using silica slabs A, AB, C, D, respectively, tiled in a four-by-four grid to create new slabs consisting of sixteen identical patches, measuring 10×10 nm^2 in total area. To create the nanochannels, the silica was placed in a periodic box with the same width and breadth as the slab, but with a height greater than that of the slab, creating systems that were effectively infinitely long and wide, with a gap of 5 to 6 nm separating the surfaces (see Figure 5.1). The volume between the surfaces was then filled with a solution of DMMP.

Following a 2000-step minimization using a conjugate gradients method, each system was equilibrated for 1.5 ns in the NPAT ensemble (constant number of particles N, pressure P, area in the xy plane A and temperature T). During the NPAT simulation, some DMMP molecules may have adsorbed to the surfaces. To remove this effect, all DMMP molecules were moved back to their initial coordinates, and constrained to those coordinates for a 0.5 ns simulation in the NVT ensemble, removing any steric clashes between DMMP and water molecules. Each system was then simulated in the NVT ensemble with a pressure gradient induced in the x-direction, resulting in a pressure-driven flow of DMMP solution through the system. To induce a pressure gradient, a constant force in the x-direction F_x was applied to all N water molecules, creating a

pressure difference ΔP_x across the system of

$$\Delta P_x = N \cdot F_x / A, \tag{D.1}$$

where A is the area of the chamber in the yz plane [29]. Temperature was maintained by applying the Langevin thermostat to all silica atoms, which was sufficient to keep the temperature of the entire system within 1.2% of the target temperature [29]. To investigate whether the pressure-driven flow affected the amount of solute bound, we performed simulations of system A with and without the applied pressure difference, which showed that the pressure-driven flow had no measurable effect on adsorption.

D.3 Analysis of the BD and MD simulations

To calculate the solute adsorption on the nanochannel surfaces, a DMMP molecule was considered adsorbed in an MD (BD) simulation if its phosphorus atom (center of mass), was within 0.5 nm of the surface. The surface of each silica slab was defined as the $x - y$ plane with the z coordinate determined as the average z coordinate of the isosurface defined by the five-to-one ratio of silica and water atoms in the MD simulation. To calculate the number bound as a function of position, shown in the middle and bottom rows of Figure D.1, the number of DMMP bound to each surface in the steady state of each simulation was averaged on a 2D histogram with a resolution of 0.42×0.42 Å^2, the same as the 2D projection of the PMF minima.

D.4 Umbrella sampling simulations.

To study the interaction between a single DMMP and the membrane surfaces, we created 5 small systems consisting of a single slab of silica membrane or an equal size phantom membrane, water, and one DMMP molecule. The potential of mean force (PMF) of a DMMP molecule as a function of its position relative to the membrane surface was determined from a set of umbrella sampling simulations [99], which were analyzed using the weighted histogram analysis method (WHAM) [100] generalized to three dimensions (see below). Prior to the umbrella sampling simulations, each of the four systems underwent 2000 steps of energy minimization, 2 ps of equilibration at fixed volume during which the temperature was raised from 0 to 295 K by velocity rescaling, and 200 ps of NPT simulation.

The umbrella sampling simulations were performed by restraining the phosphorus atom of the DMMP molecule to points in (x, y, z) (where z is perpendicular to the surface) using the potential energy function $w_i(x, y, z) = \frac{1}{2}k_x(x - x_i)^2 + \frac{1}{2}k_y(y - y_i)^2 + \frac{1}{2}k_z(z - z_i)^2$, where (x_i, y_i, z_i) was the center of sampling window

i and k_x, k_y and k_z were the spring constants along each axis. Because the gradient of the PMF was much larger along the z axis than in the xy plane, a stiffer spring constant of k_z =1390 pN/nm was used along the z axis than perpendicular to it, for which $k_x = k_y$ =70 pN/nm. Furthermore, the sampling windows (x_i, y_i, z_i) were more closely spaced along the z axis. The sampling windows formed a three-dimensional grid with 4, 4, and 9 points along the x, y, and z directions, respectively. Results were first obtained using the 144 sampling windows centered at these points, but to increase the resolution of our PMF distributions, we added another 300 sampling windows. For these simulations, we used a grid of 5, 5, and 12 points with spring constants $k_x = k_y = 560$ and $k_z = 2780$ pN/nm. To ensure that the calculated PMF extended into bulk water, 19 sampling windows with the same spring constant as the previous set were added to the (x,y) center of the slab for an additional nanometer in z. Each simulation represented more than 2.2 ns. The first 0.2 ns of each simulation was excluded from the WHAM PMF calculation.

To calculate the PMF between two DMMP molecules, we created a cubic simulation system with 2 DMMP molecules and 3,426 water molecules, measuring $4.6.6 \times 4.6$ nm^3. After a brief 1000-step energy minimization using a conjugate gradients method, the system was equilibrated for 0.2 ns in the NPT ensemble at 295 K. Umbrella sampling simulations were performed by restraining the distance between the phosphorus atoms with a potential energy function $w_i(\vec{r}_1, \vec{r}_2) = \frac{1}{2} k_r \left(|\vec{r}_1 - \vec{r}_2|\right)^2$. Results were obtained using 15 sampling windows distributed radially in shells every 0.04 nm with a force constant of $k_r = 5092$ pN/nm. Each simulation for a sampling window was represented 6 ns. The first 0.2 ns of each simulation was excluded from the WHAM PMF calculation.

D.5 Potential of mean force calculation.

The potential of mean force (PMF) is computed by the weighted histogram analysis method (WHAM) described by Roux [100] generalized to three dimensions. Each of the three spatial dimensions is a reaction coordinate. We estimate the unbiased probability distribution by

$$\langle \rho(x,y,z) \rangle = \left(\sum_{i=1}^{N_w} n_i \ \langle \rho_i(x,y,z) \rangle \right) \left(\sum_{j=1}^{N_w} n_j \exp\left[-\frac{w_j(x,y,z) - F_j}{k_\mathrm{B}T} \right] \right)^{-1}, \tag{D.2}$$

where $\rho(x,y,z)$ is the unbiased probability distribution, N_w is the number of biased simulations, $\rho_i(x,y,z)$ is the biased probability distribution derived from the results of biased simulation i, n_i and $w_i(x,y,z)$ are the number of independent data points and the biasing potential, respectively, for biased simulation i, and $\{F_i\}$ is a set of constants.

The set of constants $\{F_i\}$ are initially unknown; thus, we make an initial guess for their values. After

estimating $\langle \rho(x,y,z) \rangle$ by Equation D.2, we can obtain improved estimates these constants by solving

$$\exp\left[-\frac{F_i}{k_\mathrm{B}T}\right] = \int \mathrm{d}x \int \mathrm{d}y \int \mathrm{d}z \exp\left[-\frac{w_i(x,y,z)}{k_\mathrm{B}T}\right] \langle \rho(x,y,z) \rangle \,. \tag{D.3}$$

To obtain self-consistency, the equations are iterated, feeding the newest estimate of $\{F_i\}$ into Equation D.2 and then the newest estimate of $\langle \rho(x,y,z) \rangle$ into Equation D.3. Iteration ceases at iteration j when $\left|(F_{i+1}-F_i)^{(j)} - (F_{i+1}-F_i)^{(j-1)}\right| < 0.0001\, k_\mathrm{B}T$ for all windows $i \in \{1, 2, ..., N_w - 1\}$. The PMF is then computed by $-k_\mathrm{B}T \log(\langle \rho(x,y,z) \rangle)$.

D.6 Implicit Solvent MD Simulations

To compare our multiscale model to implicit-solvent molecular dynamics models, we created a new simulation system by removing all the water molecules from the all-atom model nanochannel system A. The effects of water were calculated using the Onufriev, Bashford, and Case (OBC) implicit solvent model [112], a generalized Born (GB) model [161], implemented in GROMACS 4 [162]. The generalized Born radius for each atom was taken to be half the distance at which the Lennard-Jones potential is zero [163] (one half the Lennard-Jones σ), and the HCT scaling factors were taken from Hawkins, Cramer and Truhlar (HCT) [164] and Tinker [165]. However, there were no available HCT scaling factors for silicon, so we created two models, one for silicon having a low HCT scaling factor of 0.72, the same as carbon, and one with a high HCT scaling factor of 9.96, the same as sulfur.

All implicit-solvent simulations were performed with GROMACS 4 [162], using a timestep of 2 fs with all bonds constrained using the P-LINCS algorithm [166], periodic boundaries, and an electrostatic and van der Waals cut-off of 2.5 nm. The implicit-solvent MD simulations only modeled the diffusion of solutes in the nanochannels, as there was no flow of solution. However, as discussed in Carr et al. [37], the amount of solute adsorbed on the nanochannel surfaces is unaffected by the flow of solution.

In our implicit-solvent MD simulations, the DMMP molecules were observed to aggregate in solution. Figure D.2 shows the radial pair distribution, "g(r)", for DMMP molecules in solution simulated with all-atom and implicit-solvent MD. From this figure, it can be seen that the implicit solvent model causes the DMMP molecules to aggregate and thus does not properly capture the dynamics of DMMP in solution. The simulation for a low HCT scaling factor for Si resulted in a steady-state adsorption density of 0.62 ± 0.03 molecules/nm^2 as compared to the all-atom MD adsorption density of 0.56 ± 0.01 molecules/nm^2. However, it is likely that the simulation had not reached a steady state, as the DMMP molecules in solution had aggregated and were likely to eventually bind to DMMP molecules adsorbed to the surface. In contrast, the

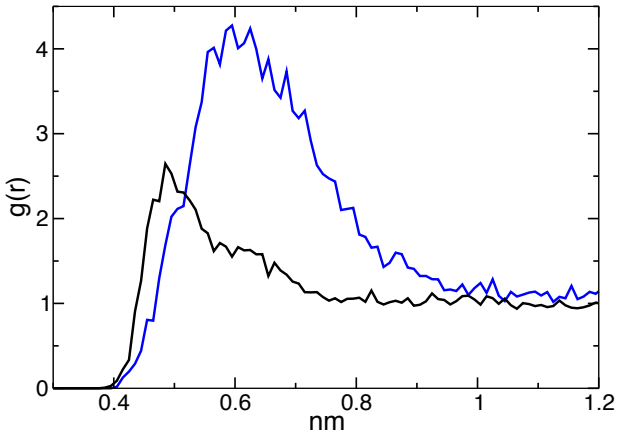

Figure D.2: The radial pair distribution of DMMP simulated with all-atom (black line) and implicit-solvent (blue line) MD

simulation high HCT scaling factor for Si resulted in no DMMP adsorption. Furthermore, little performance gain was seen by using implicit solvent: A speed of ∼28 ns/day on 240 processors was only double the performance of all-atom MD with explicit water, ∼14 ns/day on 288 processors.

D.7 Smoluchowski model

To compare our multiscale model with a simple continuum model, we used the Smoluchowski equation to predict the density of solute bound to the nanochannel surfaces. The Smoluchowski equation,

$$\partial_t C\left(z,t\right) = \partial_z \left(D\partial_z - \frac{F(z)}{\gamma} \right) C\left(z,t\right), \tag{D.4}$$

which describes the time evolution of solution concentration C under an external force F, where D is the diffusivity of the particles, γ is the coefficient of friction in the solution, and $C\left(z,t\right)$ describes the probability of finding a particle at position z at time t. The Smoluchowski model describes the dynamics of the solute as diffusive motion in an external potential and ignores solute–solute interactions. Because the Smoluchowski model does not have individual-molecule resolution, we treat the solute–surface potential W_{PS} as one-dimensional, simply a function of the distance from the surface. The one-dimensional PMF can be calculated from the 3D PMF by integrating out the unused degrees of freedom:

$$W_{\mathrm{PS}}\left(z\right) = \frac{1}{L_x L_y} \int_0^{L_x} dx \int_0^{L_y} dy \; e^{-W_{\mathrm{PS}}(x,y,z)}. \tag{D.5}$$

To solve the Smoluchowski equation, we wrote custom routines in MATLAB [167]. For the external force,

$F(z)$, we took the numerical derivative of the 1D surface–solute PMF, and interpolated the solution for the given z. We used reflective boundary conditions to conserve probability,

$$D\left(\partial_z - \frac{F(z)}{k_B T}\right) P(z,t) = 0, \text{ at } z = 0, h \text{ nm} \tag{D.6}$$

where h is the length of the channel, and an initial probability distribution,

$$C(z = 0, t = 0) = 1/h, \text{ at } 1.25 \text{ nm} < z < (h - 1.25) \text{ nm} \tag{D.7}$$

corresponding to the initial conditions of our all-atom MD simulations. The density of adsorbed DMMP molecules predicted with the Smoluchowski model are shown in Figure 5.6. Due to the lack of inter-particle interactions, the Smoluchowski equation predicts a constant fraction of solutes adsorbing to the surface in each simulation. While this is valid for low concentrations, the model over-predicts the amount of adsorbed solute at even moderate solute concentrations.

Appendix E

Synthetic ion channels embedded in biological membranes

Reproduced in part from the Supporting Information published with Carr R, Weinstock IA, Sivaprasadarao A, Müller A and Aksimentiev A (2008) Synthetic Ion Channels via Self-Assembly: a Route for Embedding Porous Polyoxometalate Nanocapsules in Lipid Bilayer Membranes Nano Lett. *8:3916–3921 (Copyright © 2008 American Chemical Society) [38].*

E.1 Coarse-grained molecular dynamics

All coarse-grained MD (CGMD) simulations were performed using the molecular dynamics program NAMD [43]. Water, ions and lipids were parameterized using the CG forcefield developed by Marrink et al. [134], and incorporated into NAMD by Shih et al. [135]. A custom forcefield was developed to describe the porous nanocapsule and DODA; the details are presented below in Appendix E. Temperature was kept constant at 310 K by Langevin thermostat using a damping coefficient of 1 ps^{-1}. To maintain pressure constant at 1 bar, the Nosé-Hoover Langevin Piston method was used with a decay period of 200 fs and a damping timescale of 50 fs [113, 114]. Each simulation was initialized through a period of minimization using a conjugate gradients method for 3000 steps followed by a 1560 step warming period to raise the temperature in 1K increments to 310K. SMD was performed using a velocity of 10^{-5} Å/timestep and a spring constant of 5 kcal/mol. The timestep of our CGMD simulations was 20 fs, which corresponds to a physical time of ∼80 fs [134], the time quoted in all figures for Chapter 6.

E.2 Modeling the system with a coarse grain

All our CGMD simulations of water, ions, octane and lipids employed the coarse-grained force field developed by Marrink et al. [134]. In the CG method, groups of atoms are replaced by beads. The beads interact like atoms in all-atom models, through bonds, angles, dihedrals and nonbonded forces. Figure E.1 shows a visual representation of our CG model of DODA. Complete details of the coarse-graining procedure are given in

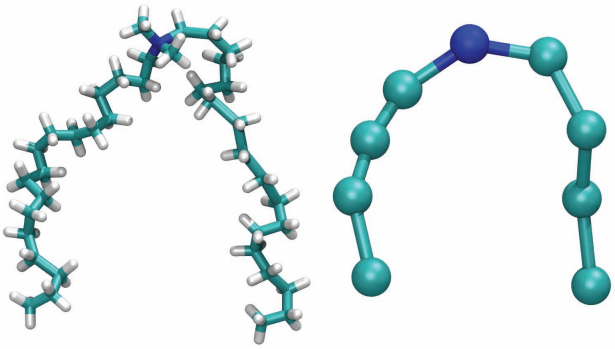

Figure E.1: All-atom (left) and CG (right) models of DODA. The blue GC bead represents the nitrogen atom of the DODA head group and its four neighboring carbons. Each cyan CG bead represents four carbons, except for the last bead on each tail representing five carbons.

the manuscript's Supporting Information [38].

The porous nanocapsule considered here is made of 12 repeats of a pentagonal unit. Thus, specifying the mapping of one pentagonal unit and its linker units to a CG representation is sufficient to describe the mapping of the entire capsule. As shown in Figure 6.1, the pentagon's center molybdenum atom and all surrounding oxygens are mapped to the center CG bead (cyan, type M). The five molybdenum atoms forming a pentagon around the center molybdenum are each mapped, with their oxygens, to the corresponding green, type B bead. Each linker molybdenum atom and its oxygens are mapped to the corresponding white, type L bead. Finally, the sulfate linker groups are mapped onto the yellow, type S beads. A complete description of the coarse-graining procedure for the porous nanocapsule is given in the manuscript's Supporting Information [38].

E.3 Validation of the coarse-grain model

To test our CG model of the porous nanocapsule and DODA, self-assembly of DODA with the capsule in a simple nonpolar solvent (octane) was simulated. Figure E.2 presents the results of a typical simulation. Starting from an initially random distribution, Figure E.2 a, DODA molecules adhere to the surface of the capsule with their positively charged head groups, Figure E.2 b–d, eventually forming a steady-state hydrophobic spheroid, Figure E.2 e. Such simulations were performed at three DODA concentrations (0.35, 0.54 and 0.8 mmol/L), three times for each concentration. A stable assembly similar to that shown in Fig.Figure E.2 e was observed at the end of each simulation.

The structure of the steady-state assembly is characterized in Figure E.3. As previously shown by Kurth and co-workers [133] for the porous CH_3COO-linker nanocapsule, DODA tends to aggregate near the capsule; its concentration decreases with the radial distance from the capsule's surface. In a steady state, DODA molecules form a spherical shell around the capsule, with their positively charged headgroup facing the negatively charged capsule and their hydrophobic tails facing the octane solvent, Figure E.3 a. The structure

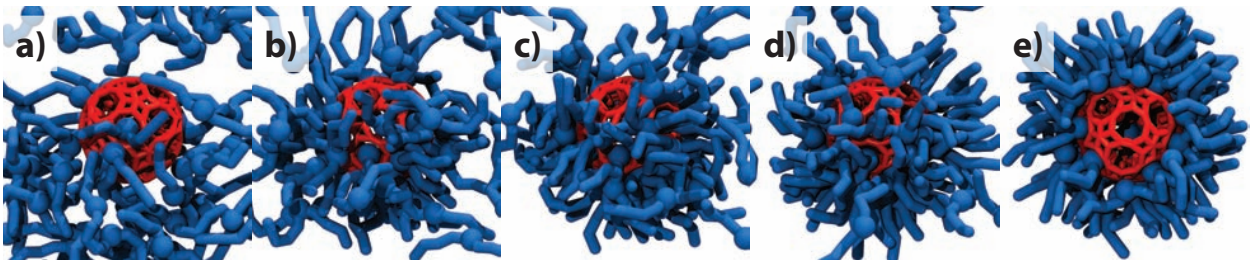

Figure E.2: Self assembly of the porous nanocapsule (red) with DODA detergent (blue) in a nonpolar solvent (not shown). The snapshots illustrate the progress of a CGMD simulation in a cut-away view. The snapshots correspond to 0 (a), 1.6 (b), 3.2 (c), 4.2 (d), and 164.0 (e) ns of the simulation. An animation illustrating the self-assembly is available in the manuscript's Supporting Information [38].

of the steady-state assembly could be reproduced in nine independent simulations performed at three different DODA concentrations, Figure E.3 b. The kinetics of the assembly is quantitatively characterized in Figure E.3 c.

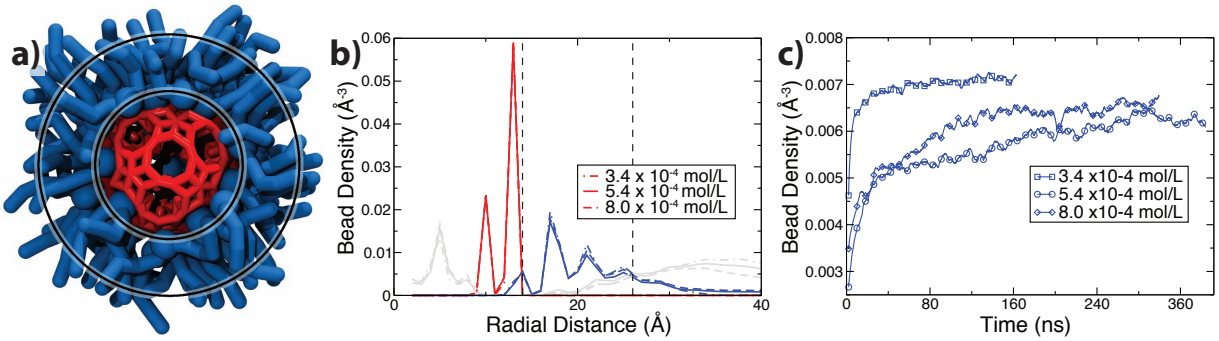

Figure E.3: Structure and kinetics of the DODA/capsule assembly in hydrophobic solvent. a) Steady-state structure of the DODA-capsule assembly. The capsule (red) is surrounded by a shell of DODA (blue). The inner and outer rings indicate the transition from the porous nanocapsule to DODA, and from DODA to solvent, respectively. b) Density of CG beads versus radial distance from the center of the capsid. Blue, red and grey indicate the density of the porous nanocapsule, DODA and octane, respectively. The transition between the domains is defined as the distance at which the corresponding bead densities become equal and is shown as dashed lines. c) Density of DODA versus time in three CGMD simulations. The density of DODA was computed in the region defined by the inner and outer rings, see panels a and b. The aggregation at 3.4×10^{-4} mol/L occurs much faster than in the other simulations because this simulation was performed having long-range electrostatics enabled via Particle Mesh Ewalds method [77].

Appendix F

Publications

- **Carr R**, Comer J, Ginsberg M. D, Aksimentiev A. Atoms-to-microns model for small solutes transport through sticky nanochannels. In preparation.
- **Carr R**, Comer J, Ginsberg M. D, Aksimentiev A. (2011) Microscopic perspective on the adsorption isotherm of a heterogeneous surface. *J Phys Chem Lett* 2:1804–1807.
- **Carr R**, Comer J, Aksimentiev A. (2011) in *Simulations in Nanobiotechnology.* (CRC Press, LLC).
- **Carr R**, Comer J, Ginsberg M. D, Aksimentiev A. (2011) Modeling pressure-driven transport of proteins through a nanochannel. *IEEE Tran Nanotechnol* 10:75–82.
- Radadia A. D, Stavis C. J, **Carr R**, Zeng H, King W. P, Carlisle J. A, Aksimentiev A, Hamers R. J, Bashir R. (2011) Control of nanoscale environment to improve stability of immobilized proteins on diamond surfaces. *Adv Funct Mater* 21:1040–1050.
- Stavis C, Clare T. L, Butler J. E, Radadia A. D, **Carr R**, Zeng H, King W. P, Carlisle, J. A, Aksimentiev A, Bashir R, Hamers R. J. (2011) Surface chemistry special feature: Surface functionalization of thin-film diamond for highly stable and selective biological interfaces.. *Proc Natl Acad Sci USA* 108:983–988.
- Wells D. B, Bhattacharya S, **Carr R**, Maffeo C, Ho A, Comer J, Aksimentiev A. (2011) in *Nanopore-based technology: single molecule characterization and DNA sequencing.* (Humana Press).
- Luan B, **Carr R**, Caffrey M, Aksimentiev A. (2010) The effect of calcium of the conformation of cobalamin transporter BtuB.. *Proteins Struct Func Bioinf.* 78:21153-21162.
- **Carr R**, Weinstock I. A, Sivaprasadarao A, Müller A, Aksimentiev A. (2008) Synthetic ion channels via self-assembly: A route for embedding porous polyoxometalate nanocapsules in lipid bilayer membranes. *Nano Lett* 8:3916–3921.

References

[1] Stavis C, et al. (2011) Surface chemistry special feature: Surface functionalization of thin-film diamond for highly stable and selective biological interfaces.. *Proc Natl Acad Sci USA* 108:983–988.

[2] Radadia A. D, et al. (2011) Control of nanoscale environment to improve stability of immobilized proteins on diamond surfaces. *Adv Funct Mater* 21:1040–1050.

[3] Ho C, et al. (2005) Electrolytic transport through a synthetic nanometer-diameter pore. *Proc Natl Acad Sci USA* 102:10445–14450.

[4] Haneveld J, Tas N, Brunets N, Jansen H, Elwenspoek M (2008) Capillary filling of sub-10 nm nanochannels. *J Appl Phys* 104:014309.

[5] Mueller A, et al. (2003) Trapping cations in specific positions in tuneable artificial cell channels: New nanochemistry perspectives. *Angew Chem Int Ed* 42:5039–5044.

[6] Craighead H (2006) Future lab-on-a-chip technologies for interrogating individual molecules. *Nature* 442:387.

[7] Lindström S, Andersson-Svahn H (2010) Overview of single-cell analyses: Microdevices and applications. *Lab Chip* 10:3363–3372.

[8] Mohammed M, Desmulliez M (2010) Lab-on-a-chip based immunosensor principles and technologies for the detection of cardiac biomarkers: A review. *Lab Chip* 11:569–595.

[9] de la Rica R, Matsui H (2010) Applications of peptide and protein-based materials in bionanotechnology. *Chem Soc Rev* 39:3499–3509.

[10] Intel Corp. (2011, May 2) Intel 22nm 3-D tri-gate transistor technology. Intel Press Release, http://newsroom.intel.com/docs/DOC-2032.

[11] Rothemund P (2006) Folding DNA to create nanoscale shapes and patterns. *Nature* 440:297–302.

[12] Stein I, Steinhauer C, Tinnefeld P (2011) Single-molecule four-color FRET visualizes energy-transfer paths on DNA origami. *J Am Chem Soc* 133:4193–4195.

[13] Schena M, et al. (1998) Microarrays: Biotechnology's discovery platform for functional genomics. *Trends Biotech* 16:301–306.

[14] Graves D (1999) Powerful tools for genetic analysis come of age. *Trends Biotech* 17:127–134.

[15] Buck M, Lieb J (2004) ChIP-chip: considerations for the design, analysis, and application of genome-wide chromatin immunoprecipitation experiments. *Genomics* 83:349–360.

[16] Hansen C, Classen S, Berger J, Quake S (2006) A microfluidic device for kinetic optimization of protein crystallization and in situ structure determination. *J Am Chem Soc* 128:3142–3143.

[17] Lavén M, et al. (2005) Imaging of peptide adsorption to microfluidic channels in a plastic compact disc using a positron emitting radionuclide. *Lab Chip* 5:756–763.

[18] Tegenfeldt J. O, et al. (2004) Micro- and nanofluidics for DNA analysis. *Anal Bioanal Chem* 378:1678–1692.

[19] Dekker C (2007) Solid-state nanopores. *Nature Nanotech* 2:209 – 215.

[20] Dimitrov V, et al. (2010) Nanopores in solid-state membranes engineered for single molecule detection. *Nanotechnology* 21:065502.

[21] Siwy Z, Fuliński A (2002) Origin of $1/f^{\alpha}$ noise in membrane channel currents. *Phys Rev Lett* 89:158101.

[22] Mirsaidov U, Comer J, Dimitrov V, Aksimentiev A, Timp G (2010) Slowing the translocation of double-stranded DNA using a nanopore smaller than the double helix. *Nanotechnology* 21:395501.

[23] Siwy Z, Heins E, Harrell C, Kohli P, Martin C (2004) Conical-nanotube ion-current rectifiers: The role of surface charge. *J Am Chem Soc* 126:10850–10851.

[24] Markoff J. (2009, October 5) I.B.M. joins pursuit of $1,000 personal genome. New York Times, http://www.nytimes.com/2009/10/06/science/06dna.html.

[25] Aksimentiev A (2010) Deciphering ionic current signatures of DNA transport through a nanopore. *Nanoscale* 2:468–483.

[26] Soelberg S, Stevens R, Limaye A, Furlong C (2009) Surface plasmon resonance detection using antibody-linked magnetic nanoparticles for analyte capture, purification, concentration, and signal amplification. *Anal Chem* 81:2357–2363.

[27] Derrington I, et al. (2010) Nanopore DNA sequencing with MspA. *Proc Natl Acad Sci USA* 107:16060.

[28] Hall A, et al. (2010) Hybrid pore formation by directed insertion of α-haemolysin into solid-state nanopores. *Nature Nanotech* 5:874–877.

[29] Carr R, Comer J, Ginsberg M. D, Aksimentiev A (2011) Modeling pressure-driven transport of proteins through a nanochannel. *IEEE Tran Nanotechnol* 10:75–82.

[30] Squires T. M, Quake S. R (2005) Microfluidics: Fluid physics at the nanoliter scale. *Rev Mod Phys* 77:977.

[31] Schoch R, Han J, Renaud P (2008) Transport phenomena in nanofluidics. *Rev Mod Phys* 80:839.

[32] Sparreboom W, Berg A, Eijkel J (2010) Transport in nanofluidic systems: A review of theory and applications. *New Journal of Physics* 12:015004.

[33] Boy D. A, Gibou F, Pennathur S (2008) Simulation tools for lab on a chip research: Advantages, challenges, and thoughts for the future. *Lab Chip* 8:1424–1431.

[34] van der Heyden F, Bonthuis D, Stein D, Meyer C, Dekker C (2006) Electrokinetic Energy Conversion Efficiency in Nanofluidic Channels. *Nano Lett* 6:2232–2237.

[35] Maffeo C, et al. (2010) DNA–DNA interactions in tight supercoils are described by a small effective charge density. *Phys Rev Lett* 105:158101.

[36] Sendner C, Horinek D, Bocquet L, Netz R. R (2009) Interfacial water at hydrophobic and hydrophilic surfaces: Slip, viscosity, and diffusion. *Langmuir* 25:10768–10781.

[37] Carr R, Comer J, Ginsberg M. D, Aksimentiev A (2011) Microscopic perspective on the adsorption isotherm of a heterogeneous surface. *J Phys Chem Lett* 2:1804–1807.

[38] Carr R, Weinstock I. A, Sivaprasadarao A, Müller A, Aksimentiev A (2008) Synthetic ion channels via self-assembly: A route for embedding porous polyoxometalate nanocapsules in lipid bilayer membranes. *Nano Lett* 8:3916–3921.

[39] Luan B, Carr R, Caffrey M, Aksimentiev A (2009) The effect of calcium of the conformation of cobalamin transporter BtuB. *Proteins Struct Func Bioinf.* In press.

[40] Carr R, Comer J, Ginsberg M, Hock V, Aksimentiev A. (2011) Atoms-to-microns model for small solute transport through sticky nanochannels. In Preparation.

[41] Carr R, Comer J, Aksimentiev A. (2011) in *Simulations in Nanobiotechnology.* (CRC Press, LLC).

[42] Wells D. B, et al. (2011) in *Nanopore-based technology: single molecule characterization and DNA sequencing.* (Humana Press).

[43] Phillips J. C, et al. (2005) Scalable molecular dynamics with NAMD. *J Comp Chem* 26:1781–1802.

[44] MacKerell A. D, Jr., et al. (1998) All-atom empirical potential for molecular modeling and dynamics studies of proteins. *J Phys Chem B* 102:3586–3616.

[45] Gumbart J, Wang Y, Aksimentiev A, Tajkhorshid E, Schulten K (2005) Molecular dynamics simulations of proteins in lipid bilayers. *Curr Op Struct Biol* 15:423–431.

[46] Chipot C, Schulten K. (2008) in *Biophysical Analysis of Membrane Proteins.* (Wiley-VCH Verlag GmbH & Co. KGaA), pp. 187–211.

[47] Hsin J, Strümpfer J, Lee E, Schulten K (2010) Molecular origin of the hierarchical elasticity of titin: Simulation, experiment, and theory.. *Annual review of biophysics* 40:187–203.

[48] Aksimentiev A, Heng J. B, Timp G, Schulten K (2004) Microscopic kinetics of DNA translocation through synthetic nanopores. *Biophys J* 87:2086–2097.

[49] Cruz-Chu E. R, Aksimentiev A, Schulten K (2006) Water-silica force field for simulating nanodevices. *J Phys Chem B* 110:21497–21508.

[50] Hassanali A. A, Singer S. J (2007) Model for the water–amorphous silica interface: The undissociated surface. *J Phys Chem B* 111:11181–11193.

[51] Comer J, Dimitrov V, Zhao Q, Timp G, Aksimentiev A (2009) Microscopic mechanics of hairpin DNA translocation through synthetic nanopores. *Biophys J* 96:593–608.

[52] Park J, Aluru N (2009) Temperature-dependent wettability on a titanium dioxide surface. *Mol Sim* 35:31–37.

[53] Schneider J, Ciacchi L. C (2011) A classical potential to model the adsorption of biological molecules on oxidized titanium surfaces. *J Chem Theory Comput* 7:473–484.

[54] Serr A, Horinek D, Netz R (2008) Polypeptide friction and adhesion on hydrophobic and hydrophilic surfaces: A molecular dynamics case study. *J Am Chem Soc* 130:12408–12413.

[55] Ziemys A, Ferrari M, Cavasotto C (2009) Molecular modeling of glucose diffusivity in silica nanochannels. *J Nanosci Nanotechnol* 9:6349–6359.

[56] Carr R, Comer J, Ginsberg M. D, Aksimentiev A (2010) Modeling pressure-driven transport of proteins through a nanochannel. *IEEE Tran Nanotechnol.*

[57] Doyle M, Archer J, Kaspar C, Weiss R (2006) FRI briefings human illness caused by E. coli O157:H7 from food and non-food sources. *FRI Briefings.*

[58] MacKenzie D. (2011, May 31) Death toll rising in cucumber bacteria outbreak. NewScientist, http://www.newscientist.com/article/dn20526-death-toll-rising-in-cucumber-bacteria-outbreak.html.

[59] Bittman M. (2011, June 7) E. coli: Dont blame the sprouts! New York Times, http://opinionator.blogs.nytimes.com/2011/06/07/e-coli-dont-blame-the-sprouts/.

[60] Dekeyser C, et al. (2008) Oligo (ethylene glycol) monolayers by silanization of silicon wafers: Real nature and stability. *J Coll Interf Sci* 324:118–126.

[61] Lasseter T, Clare B, Abbott N, Hamers R (2004) Covalently modified silicon and diamond surfaces: Resistance to nonspecific protein adsorption and optimization for biosensing. *J Am Chem Soc* 126:10220–10221.

[62] Austin R, Tegenfeldt J, Cao H, Chou S, Cox E (2002) Scanning the controls: genomics and nanotechnology. *IEEE Tran Nanotechnol* 1:12–18.

[63] Stavis S, Corgié S, Cipriany B, Craighead H, Walker L (2007) Single molecule analysis of bacterial polymerase chain reaction products in submicrometer fluidic channels. *Biomicrofluidics* 1:034105.

[64] Fologea D, Ledden B, McNabb D. S, Li J (2007) Electrical characterization of protein molecules by a solid-state nanopore. *Appl Phys Lett* 91:053901–3.

[65] Wang X, Chen Y, Gibney K. A, Erramilli S, Mohanty P (2008) Silicon-based nanochannel glucose sensor. *Appl Phys Lett* 92:013903.

[66] Martin F, et al. (2005) Tailoring width of microfabricated nanochannels to solute size can be used to control diffusion kinetics. *J Control Release* 102:123–33.

[67] Vlassiouk I, Siwy Z. S (2007) Nanofluidic diode. *Nano Lett* 7:552–556.

[68] Gracheva M. E, Vidal J, Leburton J.-P (2007) p-n semiconductor membrane for electrically tunable ion current rectification and filtering. *Nano Lett* 7:1717–1722.

[69] Xia Q, Morton K, Austin R, Chou S (2008) Sub-10 nm self-enclosed self-limited nanofluidic channel arrays. *Nano Lett* 8:3830–3833.

[70] Drazer G, Khusid B, Koplik J, Acrivos A (2005) Wetting and particle adsorption in nanoflows. *Phys Fluids* 17:017102–1–18.

[71] Sigalov G, Comer J, Timp G, Aksimentiev A (2008) Detection of DNA sequence using an alternating electric field in a nanopore capacitor. *Nano Lett* 8:56–63.

[72] Pricl S, et al. (2006) Multiscale modeling of protein transport in silicon membrane nanochannels. Part 1. Derivation of molecular parameters from computer simulations. *Biomed Microdevices* 8:277–290.

[73] Ghiringhelli L, Hess B, van der Vegt N, Delle Site L (2008) Competing adsorption between hydrated peptides and water onto metal surfaces: From electronic to conformational properties. *J Am Chem Soc* 130:13460–13464.

[74] Shen J, Wu T, Wang Q, Pan H (2008) Molecular simulation of protein adsorption and desorption on hydroxyapatite surfaces. *Biomaterials* 29:513–532.

[75] van Beest B. W. H, Kramer G. J, van Santen R. A (1990) Force fields for silicas and aluminophosphates based on *ab initio* calculations. *Phys Rev Lett* 64:1955–1958.

[76] Vollmayr K, Kob W, Binder K (1996) Cooling-rate effects in amorphous silica: A computer-simulation study. *Phys Rev B* 54:15808–15827.

[77] Batcho P. F, Case D. A, Schlick T (2001) Optimized particle-mesh Ewald/multiple-time step integration for molecular dynamics simulations. *J Chem Phys* 115:4003–4018.

[78] Housset D, Habersetzer-Rochat C, Astier J, Fontecilla-Camps J (1994) Crystal structure of toxin II from the scorpion Androctonus australis Hector refined at 1.3 a resolution.. *J Mol Biol* 238:88.

[79] Jorgensen W. L, Chandrasekhar J, Madura J. D, Impey R. W, Klein M. L (1983) Comparison of simple potential functions for simulating liquid water. *J Chem Phys* 79:926–935.

[80] Lorenz C. D, Crozier P. S, Anderson J. A, Travesset A (2008) Molecular dynamics of ionic transport and electrokinetic effects in realistic silica channels. *J Phys Chem C* 112:10222–10232.

[81] Heng J. B, et al. (2006) The electromechanics of DNA in a synthetic nanopore. *Biophys J* 90:1098–1106.

[82] Zhu F, Tajkhorshid E, Schulten K (2002) Pressure-induced water transport in membrane channels studied by molecular dynamics.. *Biophys J* 83:154–160.

[83] Aksimentiev A, Schulten K (2005) Imaging alpha-hemolysin with molecular dynamics: Ionic conductance, osmotic permeability and the electrostatic potential map. *Biophys J* 88:3745–3761.

[84] Yeh I, Hummer G (2004) System-size dependence of diffusion coefficients and viscosities from molecular dynamics simulations with periodic boundary conditions. *J Phys Chem B* 108:15873–15879.

[85] Humphrey W, Dalke A, Schulten K (1996) VMD – Visual Molecular Dynamics. *J Mol Graphics* 14:33–38.

[86] Brown S (1997) Metal recognition by repeating polypeptides. *Nature Biotech* 15:269–272.

[87] Whaley S. R, English D. S, Hu E. L, Barbara P. F, Belcher A. M (2000) Selection of peptides with semiconductor binding specificity for directed nanocrystal assembly. *Nature* 405:665–668.

[88] Naik R, Stringer S, Agarwal G, Jones S, Stone M (2002) Biomimetic synthesis and patterning of silver nanoparticles. *Nature Mater* 1:169–172.

[89] Baneyx F, Schwartz D (2007) Selection and analysis of solid-binding peptides. *Curr Op Biotech* 18:312–317.

[90] Rocco M. A, et al. (2009) Site-specific labeling of surface proteins on living cells using genetically encoded peptides that bind fluorescent nanoparticle probes. *Bioconjugate Chem* 20:1482–1489.

[91] M. M. A. S, Dutta (2005) Integrated biological-semiconductor devices. *Proc IEEE* 93:1772–1783.

[92] Wang B, Kral P (2007) Optimal atomistic modifications of material surfaces: Design of selective nesting sites for biomolecules. *Small* 3:580–584.

[93] Gracheva M, Leburton J.-P (2008) Simulation of electrically tunable semiconductor nanopores for ion current/single bio-molecule manipulation. *J Comput Electronics* 7:6–9.

[94] Castellari M, Versari A, Fabiani A, Parpinello G, Galassi S (2001) Removal of ochratoxin a in red wines by means of adsorption treatments with commercial fining agents. *J Agric Food Chem* 49:3917–3921.

[95] Mikhalovsky S (2003) Emerging technologies in extracorporeal treatment: Focus on adsorption. *Perfusion* 18:47–54.

[96] Regnier F, Gooding K (1980) High-performance liquid chromatography of proteins. *Anal Biochem* 103:1–25.

[97] Thierry B, Merhi Y, Bilodeau L, Trepanier C, Tabrizian M (2002) Nitinol versus stainless steel stents: Acute thrombogenicity study in an ex vivo porcine model. *Biomaterials* 23:2997–3005.

[98] Niedzwiecki D. J, Grazul J, Movileanu L (2010) Single-molecule observation of protein adsorption onto an inorganic surface. *J Am Chem Soc* 132:10816–10822.

[99] Torrie G, Valleau J (1977) Nonphysical sampling distributions in Monte Carlo free-energy estimation: Umbrella sampling. *Journal of Computational Physics* 23:187–199.

[100] Roux B (1995) The calculation of the potential of mean force using computer simulations. *Computer Physics Communications* 91:275–282.

[101] Poissier A, Ganeshan S, Fernandez-Serra M. V (2011) The role of hydrogen bonding in water-metal interactions. *Phys Chem Chem Phys* 13:3375–3384.

[102] Dianat A, et al. (2009) Dissociative adsorption of methane on surface oxide structures of Pd-Pt alloys. *J Phys Chem C* 113:21097–21105.

[103] Ermak D, McCammon J (1978) Brownian dynamics with hydrodynamic interactions. *J Chem Phys* 69:1352.

[104] Fayad G, Hadjiconstantinou N (2010) Realistic brownian dynamics simulations of biological molecule separation in nanofluidic devices. *Microfluid Nanofluid* 8:521–529.

[105] Im W, Seefeld S, Roux B (2000) A grand canonical Monte Carlo–Brownian Dynamics algorithm for simulating ion channels. *Biophys J* 79:788–801.

[106] Potter M, Luty B, Zhou H, McCammons J (1996) Time-dependent rate coefficients from Brownian Dynamics simulations. *J Phys Chem* 100:5149–5154.

[107] Woolf T, Roux B (1994) Molecular dynamics simulation of the gramicidin channel in a phospholipid bilayer. *Proc Natl Acad Sci USA* 91:11631.

[108] Hummer G (2005) Position-dependent diffusion coefficients and free energies from Bayesian analysis of equilibrium and replica molecular dynamics simulations. *New J Phys* 7:34.

[109] Landau L. D, Lifshitz E. M. (1999) *Fluid Mechanics*, Course of theoretical physics. (Pergamon Press, Oxford, New York) Vol. 6, 2 edition.

[110] Zhang J (2010) Lattice boltzmann method for microfluidics: models and applications. *Microfluid Nanofluid* pp. 1–28.

[111] van Kampen N. G. (1992) *Stochastic Processes in Physics and Chemistry.* (North-Holland, Amsterdam, New York).

[112] Onufriev A, Bashford D, Case D (2004) Exploring protein native states and large-scale conformational changes with a modified generalized born model. *Proteins Struct Func Bioinf* 55:383–394.

[113] Brünger A. T. (1992) *X-PLOR, Version 3.1: A System for X-ray Crystallography and NMR* (The Howard Hughes Medical Institute and Department of Molecular Biophysics and Biochemistry, Yale University).

[114] Martyna G. J, Tobias D. J, Klein M. L (1994) Constant pressure molecular dynamics algorithms. *J Chem Phys* 101:4177–4189.

[115] Hille B. (2001) *Ionic channels of excitable membranes.* (Sinauer Associates, Sunderland, MA), 3rd edition.

[116] Gouaux E, MacKinnon R (2005) Principles of selective ion transport in channels and pumps. *Nature* 310:1461–1465.

[117] Doyle D. A, et al. (1998) The structure of the potassium channel: Molecular basis of K^+ conduction and selectivity. *Science* 280:69–77.

[118] Chang G, Spencer R. H, Lee A. T, Barclay M. T, Rees D. C (1998) Structure of the MscL homolog from *Mycobacterium tuberculosis*: A gated mechanosensitive ion channel. *Science* 282:2220–2226.

[119] Hilf R, Dutzler R (2008) X-ray structure of a prokaryotic pentameric ligand-gated ion channel. *Nature* 452:375.

[120] Long S. B, Campbell E. B, MacKinnon R (2005) Crystal structure of a mammalian voltage-dependent *Shaker* family K^+ channel. *Science* 309:897–903.

[121] Jasti J, Furukawa H, Gonzales E, Gouaux E (2007) Structure of acid-sensing ion channel 1 at 1.9 Å resolution and low pH. *Nature* 449:316–323.

[122] Fyles T (2007) Synthetic ion channels in bilayer membranes. *Chem Soc Rev* 36:335–347.

[123] Koert U, Al-Momani L, Pfeifer J. R (2004) Synthetic Ion Channels. *Synthesis* 2004:1129–1146.

[124] Matile S, Som A, Sordé N (2004) Recent synthetic ion channels and pores. *Tetrahedron* 60:6405–6435.

[125] Gokel G, Mukhopadhyay A (2001) Synthetic models of cation-conducting channels. *Chem Soc Rev* 30:274–286.

[126] Müller A, Roy S (2005) Multifunctional metal oxide based nanoobjects: Spherical porous capsules/artificial cells and wheel-shaped species with unprecedented materials properties. *J Mater Chem* 15:4673–4677.

[127] Müller A, Roy S (2005) Linking Giant Molybdenum Oxide Based Nano-Objects Based on Well-Defined Surfaces in Different Phases. *Eur J Inorg Chem* pp. 3561–3570.

[128] Müller A, Roy S. (2004) *The Chemistry of Nanomaterials: Synthesis, Properties and Applications* eds. Rao C, Müller A, Cheetham A. (Wiley-VCH).

[129] Müller A, et al. (2003) Drawing small cations into highly charged porous nanocontainers reveals "water" assembly and related interaction problems. *Angew Chem Int Ed* 42:2085–2090.

[130] Merca A, et al. (2007) Mimicking biological cation-transport based on sphere-surface supramolecular chemistry: Simultaneous interaction of porous capsules with molecular plugs and passing cations.. *Chem Eur J* 13:7650–7658.

[131] Rehder D, Haupt E. T. K, Bögge H, Müller A (2006) Countercation transport modeled by porous spherical molybdenum oxide based nanocapsules.. *Chem Asian J* 1-2:76–81.

[132] Müller A, et al. (2006) "Gating" the Pores of a Metal Oxide Based Capsule: After Initial Cation Uptake Subsequent Cations Are Found Hydrated and Supramolecularly Fixed Above the Pores. *Angew Chem Int Ed Engl* 45:460.

[133] Volkmer D, et al. (2000) Toward Nanodevices: Synthesis and Characterization of the Nanoporous Surfactant-Encapsulated Keplerate $(DODA)_{40}(NH_4)_2[(H_2O)Mo_{132}O_{372}(CH_3COO)_{30}(H_2O)_{72}]$. *J Am Chem Soc* 122:1995–1998.

[134] Marrink S. J, de Vries A. H, Mark A. E (2004) Coarse grained model for semiquantitative lipid simulations. *J Phys Chem B* 108:750–760.

[135] Shih A. Y, Arkhipov A, Freddolino P. L, Schulten K (2006) Coarse grained protein-lipid model with application to lipoprotein particles. *J Phys Chem B* 110:3674–3684.

[136] Marrink S. J, Risselada H. J, Yefimov S, Tieleman D. P, de Vries A. H (2007) The martini forcefield: Coarse grained model for biomolecular simulations. *J Phys Chem B* 111:7812–7824.

[137] Lopez C. F, Nielsen S. O, Moore P. B, Klein M. L (2004) Understanding nature's design for a nanosyringe. *Proc Natl Acad Sci USA* 101:4431–4434.

[138] Wallace J, Sansom M (2007) Carbon nanotube/detergent interactions via coarse-grained molecular dynamics. *Chem Phys of Lipids* 149:89–89.

[139] Wong-Ekkabut J, et al. (2008) Computer simulation study of fullerene translocation through lipid membranes. *Nature Nanotech* 3:363.

[140] Knecht V, Marrink S (2007) Molecular Dynamics Simulations of Lipid Vesicle Fusion in Atomic Detail. *Biophys J* 92:4254.

[141] Marrink S. J, Mark A. E (2003) Molecular dynamics simulation of the formation, structure, and dynamics of small phospholipid vesicles. *J Am Chem Soc* 125:15233–42.

[142] Stevens M. J, Hoh J. H, Woolf T. B (2003) Insights into the molecular mechanism of membrane fusion from simulations: Evidence for the association of splayer tails. *Phys Rev Lett* 91:188102.

[143] Kasson P. M, et al. (2006) Ensemble molecular dynamics yields submillisecond kinetics and intermediates of membrane fusion. *Proc Natl Acad Sci USA* 103:11916–11921.

[144] Isralewitz B, Izrailev S, Schulten K (1997) Binding pathway of retinal to bacterio-opsin: A prediction by molecular dynamics simulations. *Biophys J* 73:2972–2979.

[145] Müller A, et al. (2004) Artificial cells: Temperature-dependent, reversible Li^+-ion uptake/release equilibrium at metal oxide nanocontainer pores. *Angew Chem Int Ed* 43:4466–4470.

[146] Haupt E, Wontorra C, Rehder D, Müller A (2005) Porous inorganic capsules in action: Modelling transmembrane cation-transport parameter-dependence based on water as vehicle. *Chemical Communications* 2005:3912–3914.

[147] Haupt E. T. K, Wontarra C, Rehder D, Merca A, Müller A (2008) Confinement and step-wise reopening of channels in an artificial cell/inorganic capsule: A ^{7}Li NMR study. *Chem Eur J* 14:8808–8811.

[148] Rehder D, Haupt E. T. K, Müller A (2008) Cellular cation transport studied by $^{6/7}$Li and ^{23}Na NMR in a porous Mo_{132} keplerate type nano-capsule as model system. *Magn Res Chem* 46:S24–S29.

[149] Miyamoto S, Kollman P. A (1992) SETTLE: An analytical version of the SHAKE and RATTLE algorithm for rigid water molecules. *J Comp Chem* 13:952–962.

[150] Andersen H (1983) Rattle: A "velocity" version of the Shake algorithm for Molecular Dynamics calculations. *J Comp Phys* 52:24–34.

[151] Joung I. S, Cheatham T. E, III (2008) Determination of alkali and halide monovalent ion parameters for use in explicitly solvated biomolecular simulations. *J Phys Chem B* 112:9020–9041.

[152] Deb B, He W, Song K (2008) An analytical potential energy function to model protonated peptide soft-landing experiments. The $CH_3NH_3^+/CH_4$ interactions. *Physical Chemistry Chemical Physics* 10:4565–4572.

[153] Wells D. B, Abramkina V, Aksimentiev A (2007) Exploring transmembrane transport through α-hemolysin with grid-steered molecular dynamics. *J Chem Phys* 127:125101.

[154] Luan B, Aksimentiev A (2010) Electric and electrophoretic inversion of the DNA charge in multivalent electrolytes. *Soft Matter* 6:243–246.

[155] Aksimentiev A, Brunner R, Cruz-Chu E. R, Comer J, Schulten K (2009) Modeling transport through synthetic nanopores. *IEEE Nanotechnology Magazine* 3:20–28.

[156] Vishnyakov A, Neimark A (2004) Molecular Model of Dimethylmethylphosphonate and Its Interactions with Water. *J Phys Chem A* 108:1435–1439.

[157] Barvik, Jr. I, Stepanek J, Bok J (2002) Explicit solvent molecular dynamics simulation of duplex formed by the modified oligonucleotide with alternating phosphate/phosphonate internucleoside linkages and its natural counterpart.. *J Biomol Struct Dyn* 19:863–75.

[158] Štrajbl M, et al. (1997) Vibrational spectra and quantum mechanical force fields of modified oligonucleotide linkages: 1. methyl methoxymethanphosphonate. *Journal of Molecular Structure* 415:161 – 177.

[159] Eaton G, Harris L, Patel K, Symons M (1992) Infrared and nuclear magnetic resonance spectroscopic studies on the solvation of trimethylphosphate and dimethylmethylphosphonate. *Journal of the Chemical Society Faraday transactions* 88:3527–3531.

[160] Comer J, Wells D. B, Aksimentiev A. (2011) in *Protocols in DNA nanotechnology.* (Humana Press).

[161] Baker N. A, Bashford D, Case D. A. (2006) in *New Algorithms for Macromolecular Simulation*, Lecture Notes in Computational Science and Engineering, eds. Leimkuhler B, et al. (Springer Berlin Heidelberg) Vol. 49, pp. 263–295.

[162] Hess B, Kutzner C, Van Der Spoel D, Lindahl E (2008) Gromacs 4: Algorithms for highly efficient, load-balanced, and scalable molecular simulation. *J Chem Theory Comput* 4:435–447.

[163] Bjelkmar P, Larsson P, Cuendet M, Hess B, Lindahl E (2010) Implementation of the CHARMM force field in GROMACS: Analysis of protein stability effects from correction maps, virtual interaction sites, and water models. *J Chem Theory Comput* 6:459–466.

[164] Hawkins G, Cramer C, Truhlar D (1996) Parametrized models of aqueous free energies of solvation based on pairwise descreening of solute atomic charges from a dielectric medium. *J Phys Chem* 100:19824–19839.

[165] Ponder J. (2009) Tinker: Software tools for molecular design.

[166] Hess B (2008) P-lincs: A parallel linear constraint solver for molecular simulation. *J Chem Theory Comput* 4:116–122.

[167] The MathWorks, Inc. (2008) Matlab v.7.